Nanofluidic insight into energy harvesting and desalination

Catherine Sempere

Université Claude Bernard Lyon 1

Ecole doctorale Physique et astrophysique de Lyon

Nanofluidic insight into energy harvesting and desalination

Catherine Sempere

Thèse présentée pour l'obtention du diplôme de doctorat,

soutenue publiquement le 14 octobre 2015

Jury:

M.	Benoît COASNE	LIPhy, Grenoble	Rapporteur
M.	Frédéric RESTAGNO	LPS, Orsay	Rapporteur
M.	Thierry BIBEN	ILM, Lyon	Examinateur
M.	Didier NOËL	EDF Lab les Renardières	Examinateur
M.	Lydéric BOCQUET	LPS-ENS, Paris	Directeur de thèse
M.	Alessandro SIRIA	LPS-ENS, Paris	Directeur de thèse

Institut Lumière Matière
UMR5306 CNRS
Université Claude Bernard Lyon 1
Domaine Scientifique de La Doua
Bâtiment Kastler, 10 rue Ada Byron
69622 Villeurbanne CEDEX, France

Abstract

The first part of this thesis is an introduction to the different energy conversion and desalination methods that will be invoked in this work.
In a second part, we show that the ionic conductance of a nanopore array is sub-additive with the number of pores. Individal contributions of each pore to the global conductance tend to a null value, if the network is big enough. We note that this phenomenon only involves length ratios, and that working at a nanometric scale does not have any influence.
Then, in a third part, we measure the permeability of a pore array at a macroscopic scale. There too, the effect of the array does not depend on the scale of the system. Permeability evolves inversely to conductance: permeability is enhanced by the presence of neighboring pores, but in a smaller proportion than the ionic conductance falls under the same cause.
The fourth part uses the results of the two preceding ones, to determine a scaling law for the electric power produced by streaming current and diffusio-osmosis, two methods of osmotic energy conversion. We show that entrance effects have a negative impact on such conversion, more efforts are needed to understand them better and circumvent them.
The fifth and last part of this thesis is a numerical work on a new desalination device. It relies on osmosis through a gas phase which is trapped within a hydrophobic nanotube. Its main interest is to use nanotubes bigger than the pores of currently used materials, thus less prone to fouling. We use molecular dynamics methods to study the permeability and selectivity of this device.

Key words : nanofluidics, entrance effects, pore arrays, ionic and fluidic transport, cross-coupling transport phenomena, osmotic energy, energy conversion, desalination

Résumé

Une approche nanofluidique de la conversion d'énergie et du dessalement

La première partie de cette thèse constitue une introduction aux différentes méthodes de conversion d'énergie et de dessalement qui seront évoquées dans cet ouvrage.
Dans une deuxième partie, nous montrons que la conductance ionique d'un réseau de nanopores est sous-additive avec le nombre de pores. La contribution individuelle de chaque pore à la conductance globale tend vers une valeur nulle, pour un réseau suffisamment grand. On note que seuls des rapports de longueurs interviennent, et que le choix d'une échelle nanométrique n'a pas d'influence dans l'effet observé.
Ensuite, dans une troisième partie, nous mesurons la perméabilité d'un réseau de pores à une échelle macroscopique. Là aussi, l'influence du réseau ne dépend pas de l'échelle du système. La perméabilité évolue en sens inverse de la conductance : elle est augmentée par la présence de pores voisins, mais dans une faible proportion.
La quatrième partie se sert des résultats des deux parties précédentes, dans le but de déterminer une loi d'échelle pour la puissance électrique produite par courant d'écoulement et diffusio-osmose, deux méthodes de conversion d'énergie osmotique. On montre que les effets d'entrée ont un effet délétère sur cette conversion ; ils nécessitent des études plus approfondies.
La dernière partie est un travail numérique sur un nouveau procédé de dessalement par osmose via une phase gaz, piégée dans des nanotubes hydrophobes. Son intérêt principal est l'utilisation de nanotubes plus

gros que les pores des matériaux actuellement utilisés, donc moins susceptibles de s'encrasser. Par dynamique moléculaire, nous étudions la perméabilité et la sélectivité du dispositif.

Mots-clés : nanofluidique, effets d'entrée, réseaux de pores, transport ionique et fluidique, phénomènes de transport couplés, énergie osmotique, conversion d'énergie, dessalement

Résumé substantiel

La nanofluidique est, chronologiquement, la petite sœur de la microfluidique, mais aujourd'hui elle représente un domaine en pleine expension avec des persepctives industrielles et économiques peut-être même plus vastes. En effet, des applications d'une grande importance sociétale font intervenir des objets nanofluidiques, à commencer par les techniques de séparation dans les liquides. Le dessalement et la purification de l'eau se font généralement à travers des membranes de pores sub-nanométriques, s'inspirant de processus biologiques d'efficacité encore non égalée. La nanofluidique porte également de grands espoirs dans la production d'énergie d'origine osmotique. Grâce à des membranes poreuses, là aussi de dimension typique subnanométrique, de l'énergie chimique stockées dans les gradient salins est convertie en énergie électrique. L'entreprise norvégienne Statkraft a fait fonctionner une usine pilote sur ce principe de 2009 à 2013.

Un des comportements les plus intéressants découverts par les recherches en nanofluidique est celui du glissement quasi parfait de l'eau dans des nanotubes de carbone (CNT). Cette structure, constituée d'un feuillet de graphène enroulé, est devenue un objet d'étude commun depuis les résultats de Sumio Iijima en 1991. Depuis, d'autres types de nanotubes ont suscité de l'intérêt, comme les nanotubes de nitrure de bore (BNNT), dont on a récemment mis en évidence la charge surfacique exceptionnelle (jusqu'à $1\mathrm{C/m}^2$, ce qui représente 1 électron pour 2 atomes du nanotube). Ces propriétés font que les CNT portent des espoirs plutôt en filtration et dessalement, où ils permettraient d'augmenter le flux d'eau tout en gardant une bonne sélectivité vis-à-vis des ions et des impuretés. Quant aux BNNT, ils sont envisagés plutôt comme convertisseurs d'énergie *via* la diffusio-osmose, qui tire partie de leur forte charge de surface.

Toutefois, les bonnes propriétés du transport au sein des nanotubes ne doit pas faire oublier les effets d'entrée, c'est-à-dire ce qu'il se passe aux accès des nanotubes. Même si la friction est négligeable dans un CNT, et même si la charge de surface est très grande dans un BNNT, le transport fluidique et ionique sera toujours limité par le fait que les molécules d'eau et les ions doivent converger depuis le bulk jusqu'à la nanostructure. Depuis les travaux fondateurs de Sampson en hydrodynamique, et de Hille et Hall en physiologie, la valeur de la résistance d'accès est bien connue lorsqu'on considère un nanopore ou un nanotube unique, de section circulaire. En revanche, les effets de géométrie et les effets collectifs entre pores ont été peu étudiés. Cette thèse propose de pallier ce manque, et, dans les deux premières parties, nous présentons des travaux expérimentaux dont le but est de mieux comprendre la dépendance de la résistance d'entrée, ionique ou fluidique, avec le nombre de pores présents et la géométrie du réseau.

La première partie de cette thèse constitue une introduction aux différentes méthodes de conversion d'énergie et de dessalement qui seront évoquées dans cet ouvrage.

Dans une deuxième partie, nous montrons que la conductance ionique d'un réseau de nanopores est sous-additive avec le nombre de pores. En effet, la présence de pores voisins entraîne une augmentation de la résistance ionique d'entrée à travers un pore. Ce travail expérimental permet de vérifier des lois d'échelles prédisant une contribution individuelle de chaque pore à la conductance globale tendant vers une valeur nulle, pour un réseau suffisamment grand. Un point intéressant ici est que seul des rapports de longueurs interviennent. Le rapport entre l'épaisseur du pore et son rayon détermine la sensibilité aux effets d'entrée, et le rapport entre le rayon et la distance interpore donne la mesure des intéractions interpores. Finalement, le fait d'être à une échelle nanométrique n'a pas d'influence dans l'effet observé (car on se

place dans un régime où la charge de surface n'a pas d'influence sur la conductance).

Dans une troisième partie, nous mesurons la perméabilité d'un réseau de pores à une échelle macroscopique. Là aussi, l'influence du réseau ne dépend pas de l'échelle du système, mais seulement du rapport entre rayon et distance interpore. La perméabilité évolue en sens inverse de la conductance : elle est augmentée par la présence de pores voisins, mais dans des proportions plus faibles que la conductance ionique ne diminue par la même cause. Surtout, la contribution individuelle des pores à la perméabilité totale sature rapidement lorsqu'on augmente le nombre de pores.

La quatrième partie se concentre sur des phénomènes de transport dits couplés ou croisés, typiquement nanofluidique, où le type de transport diffère du type l'excitation. Par exemple, dans la diffusio-osmose, on observe un écoulement et un courant ionique, en réponse à un gradient salin. En se servant des résultats des deux parties précédentes, nous déterminons une loi d'échelle pour la puissance électrique produite par courant d'écoulement et diffusio-osmose, deux méthodes de conversion d'énergie osmotique. On montre que les effets d'entrée ont un effet délétère sur cette conversion ; ils nécessitent des études plus approfondies.

La cinquième partie est un travail numérique sur un nouveau procédé de dessalement par osmose via une phase gaz. Son intérêt principal est l'utilisation de nanotubes "plus gros" que les pores des matériaux actuellement utilisés, donc moins susceptibles de s'encrasser. Dans cette méthode, les nanotubes sont hydrophobes et comportent une bulle de vapeur qui joue le rôle de membrane sélective, imperméable aux ions. Le rayon maximal du nanotube n'est alors limité que par la stabilité de l'interface liquide-vapeur. L'emploi de la dynamique moléculaire nous permet de tester la dépendance de la perméabilité du dispositif

en fonction des paramètres géométriques. Nous mettons également en évidence le fait que le nanotube doit avoir une longueur minimale, égale à son rayon, afin que la bulle perdure. Ceci représente une borne supérieure à la valeur du gradient de concentration dans un nanotube, ce qui en fait une limite de la présente méthode. Nous présentons enfin le calcul de la barrière d'énergie libre qui s'oppose à un ion traversant la bulle de vapeur, entouré d'une couche de molécules d'eau.

Remerciements

Je remercie chalereusement Lydéric Bocquet et Alessandro Siria de m'avoir acceptée en thèse auprès d'eux, et de m'avoir consacré du temps. Lydéric, ta façon de faire de la science est éblouissante, et je ne doute pas une seule seconde que tes réalisations prochaines ne continuent d'apporter des avancées significatives à l'état de la connaissance en matière molle. Alessandro, le jeune chercheur prometteur que tu étais a encore pris du galon ! Ton opiniatreté au travail, tout comme l'importance que tu accordes au sport, sont très inspirantes.

Je remercie également du fond du coeur mes encadrants officieux lyonnais : Anne-Laure Biance, avant son départ pour le Japon, et Christophe Ybert qui a pris le relai. J'ai beaucoup apprécié travailler avec vous, en particulier du fait de vos approches si complémentaires. Anne-Laure, ta soif de science et la multiplicité des projets que tu entreprends font plaisir à voir. Puisses-tu continuer à mettre autant de coeur à l'ouvrage, et à transmettre la persévérance – comme tu l'as fait pour moi face à mes manips d'hydro ! Christophe, ta rigueur nous a permis un bon substantiel dans la compréhension des effets d'entrée, nul doute que tes qualités scientifiques seront à l'origine de bien d'autres résultats. Merci aussi pour ton écoute et tes paroles bienveillantes !

Simon Gravelle, doctorant de la même promo que moi, fut aussi un encadrant officieux. Cher Simon, bravo pour tout le travail que tu as accompli, mais surtout MERCI, pour ton aide, ton enseignement de LAMMPS, ta simplicité, et l'exemple de travail que tu donnes – entre autres.

Merci Laurent Joly, ton aide importante était pour moi complètement inespérée ! C'est quand même chouette, ça, que juste parce qu'on trouve un sujet sympa, on vienne en discuter avec l'étudiant–e qui travaille dessus ! C'est un idéal que je croyais dépassé, englouti sous la paperasse

des chercheurs.
Merci à Christophe Dujardin, directeur de l'école doctorale PhAST : t'avoir comme interlocuteur dans un moment de doute a été une grande chance. Si un RH avait fait le recrutement, il n'aurait pas pu trouver meilleur directeur d'ED.
Merci à Philippe Poncharal pour les heures passées au MEB ensemble, à essayer de m'enseigner le doigté nécessaire à la nanomanipulation, à Pasal Vincent pour m'avoir appris à faire les plus jolies pointes du monde. Merci à Alessandro Gadaleta, Elisa Tamborini, Remy Brossard ("l'équipe"), et aussi à Oriane Bonhomme, Catherine Barentin et Thierry Biben pour les intéressantes discussions scientifiques que nous avons eues.
Pour le volet aide à la conception/réalisation, merci à Rémy Fulcrand et Nick Blanchard pour toute la microscopie, à Rémy pour l'imprimante 3D et Gilles Simon pour tout le reste. Merci à Ruben Mascart et Fabio Rampoldi de l'informatique. Merci à Christelle Macheboeuf pour son efficacité et son sourire.
Je voudrais aussi remercier Corinne Augier et Catherine Barentin qui m'ont fait confiance dans l'enseignement. C'était particulièrement agréable de travailler avec vous, on se sentait une vraie équipe ! Merci à tous les collègues enseignants, en particulier à Julien Lam pour l'aventure de la copie perdue, à Osvanny Ramos pour m'avoir appris le principe de base de la photo lors des TP de L1 ! Merci à mes élèves pour tous les échanges que nous avons eu.
Un très grand merci à Didier Noël, chercheur senior à EDF, de m'avoir fait confiance pour une mission de doctorant-conseil sur les nanotubes de carbone. Egalement, merci beaucoup à Emanuela Buccafurri qui a assuré le suivi du projet, pour ses conseils et ses retours, qui m'ont été et me resteront fort utiles. Au passage, merci à Léa Bello, de m'avoir appris que 2 ans d'ACE suffisaient à valider l'Agreg !
L'Unviersité ne serait pas grand chose si le monde extérieur ne savait pas

ce qu'on y fait. Merci à Eric Le Roux pour ce superbe projet artistico-scientifique These's Art. Merci à ma super photographe Stéphanie Allaix, c'était tellement cool ce shooting dans ma cuisine !

En trois ans de thèse on travaille beaucoup, mais on papotte encore plus avec ses co-bureaux. Alors, merci à vous pour tout ce bavardage, par ordre chronologique dans le bureau 11-011 : Xixi, Kelly, et Choongeyop, je vous ai pardonné votre accueil un peu froid ! Richard, ta prédiction est résolument fausse, ma thèse est finie, je ne suis pas mariée et je n'ai pas d'enfants, aucun sortilège n'est attaché à mon bureau ! Pascal, te découvrir féministe fut une joie inouïe ! Florence, notre désillusionnée nationale, qui est quand même presque toujours de bonne humeur et souriante. Rodney, le musicien brésilien qui ne s'est jamais plaint, Alexis, ou L'homme-qui-voyage-et-déménage, pour sa douce folie qu'il a bien essayé de nous cacher un long moment ! Coraline, pour son énergie débordante, ses clopes, la fête, et sa ténacité malgré l'omniprésence des tamis dans sa vie ! Tess, la petite dernière, qui apporte un sentiment de calme et de douce constance dans toute cette agitation. Sans oublier les nouveaux venus par le miracle de la cloison : Joseph, le biophysicien-gourmet-musicien-X-basketteur-clown, et encore, mon analyse omet sûrement d'autres caractéristiques. De la balle à la ker-ridor bawl, en passant par le fameux mail "Nutella", tes surprises ont joyeusement pimenté nos quotidiens. Menka, ma soeur macédonienne, que je ne cesserai d'admirer pour l'intelligence avec laquelle elle pratique la tolérance. Sébastien le petit jeune, qui, malgré un voyage à Cuba n'a toujours rien trouvé de plus beau que ses montagnes ! Je te souhaite d'y retourner et d'en profiter. Teresa, que je regrette de n'avoir pas mieux connue, qui semble très prometteuse !

Parmi toutes ces personnes, certaines méritent un merci spécial pour leur aide précieuse avec Matlab, sans lesquelles ma thèse n'aurait pas été ce qu'elle est : merci+++ aux pros que sont Pascal, Alexis, et Menka ! Merci à tout le reste de l'équipe Liquides et Interfaces pour l'atmosphère

très agréable qui y règne et les nombreux gateaux partagés en salle café ! Merci en particulier aux doctorants et post-doctorants Baudouin, Henri, Isaac, Nico W., Pauline, Antoine, Ludivine, Nicolas, Ramon, Aude et John qui sont déjà partis ; Loren, Alexandra, Félix, Ronan, Quentin, Andrea, Marie-Emelyne qui restent. Merci aussi aux stagiaires, que, fidèle à la coutume, j'ai honteusement oublié jusqu'à présent.
Merci aussi aux amis du labo, situés dans des couloirs un peu plus éloignés : Julien Lam, Antoine Aubret, Nora Abdellaoui, Daniel Förster (l'homme le plus gentil de la Terre).
Voici venue l'heure de remercier haut et fort mes colocs Victoria, Daniel et Pierre. J'ai eu TELLEMENT de chance de vous avoir eu !!! Merci à tous mes amis de l'ENS de Lyon, ceux du campus de la Doua Martin, Jibé, Sylvain, Léa, Tatjana, Etienne, et ceux restés à l'ENS comme ce cher JujuBee ! Mais aussi Louison (le photopore indien brillera au Chili !), Charlotte et Amandine, toujours présentes lors de mes excursions parisiennes. Merci à Maxime-Guillaume et Chiho, à Lydie, et l'adorable famille brésilienne Rodrigo, Marina et Luiza. Enfin merci à Pauline : pour la discrétion, pour l'accueil en temps de chaudière cassée, pour tous les bons moments, et à Fosca : nous avons traversé tellement de choses ! Et aujourd'hui nous sommes toujours contentes de nous voir, c'est une grande joie pour moi.
Merci à Tita, Poupine, Moumine et mes parents, pour leur soutien qui n'a jamais failli durant ces 3 ans.
Merci à mon compagnon pour être lui ♥ !

Contents

À ma mère

Chapter 1

Nanofluidics, energy harvesting and desalination

Nanofluidics was born from a great ambition: to undertake the technical and intellectual challenges of handling flows at an always smaller scale. Its realm begins where microfluidics ends, below 1 micron. Apart from the inherent interest this challenge holds, the aim to mimick biological behaviors, and try to reach their efficiency, is one of the main engines of the nanofluidic-community creativity. For example, researchers have long had their eyes on the high selectivity of ion channels and pumps on cell membranes. From urea filtration within the Henle loop in kidneys, to energy generation from saline gradients between both sides of cell membranes, the human body is an incredibly rich source of inspiration. Moreover, the numerous applications arising from nanofluidics reinforce the global impact of this discipline. The fields of genomics, filtration, desalination and energy harvesting are the most likely to be deeply affected by this relatively new science [1], of which the theoretical

foundations date back to the 1960s but the numerical and experimental tools were only ready at the turn of the century.

The phenomena studied in this thesis lay deeply in the field of nanofluidics and are closely linked to applications. Firstly, we focused on a typical nanoscopic phenomenon known as entrance effects, consisting in a (hydrodynamic or ionic) resistance at nanochannel entrances [2–4]. In membranes containing several nanochannels, collective behaviors at pore mouths strongly influence entrance effects. We will discuss how these behaviors are crucial to address, in particular in the field of energy harvesting. They demonstrate that although nanoscale transport properties are very promising, the coupling between a nanochannel and the outside world can undermine the global efficiency of a macroscopic device built from nanofluidic basic units. Special care is therefore needed for the prototypes expected in a very near future, as scaling-up toward a marketable device requires more than a simple parallelization of nanochannels.
The other facet of this thesis deals with a new nanofluidic device, designed to provide osmotic transport through two different phases, liquid and gas [5–7]. It bears some similarities with existing desalination processes, but shows unprecedented advantages which we studied numerically.

To contextualize our work, we propose now to introduce a few existing energy conversion and desalination processes using nanoporous membranes. Whether it be for energy harvesting or desalination, all the methods presented here rely on ion separation from water (except for streaming currents). The aim is either, just to clean the water, or to convert the chemical energy stored in salinity gradients – the Gibbs free energy of mixing – into electrical energy. Thus, we choose not to categorize the processes according to their finality, but to the physics at stake.

In a first time, we will present the electrokinetic phenomena known as electro-osmosis and streaming currents. We then turn to the very important class of osmosis-related phenomena, among which diffusio-osmosis is of particular interest for future applications in energy harvesting. Distillation processes, much employed for desalination, will follow, and last we will evoke electrostatic-interaction-based techniques.
Our purpose here is not to be exhaustive, but to give the reader an overview of the processes relating to this thesis. This will offer the opportunity to shed light upon some of the new behaviors unveiled by nanofluidics.

1.1 Electrokinetic phenomena

As one goes down toward the nanoscale, the classical laws describing fluid behavior remain valid, at least until 1 nm [8, 9]. Yet, the relative importance of surface over bulk increases, leading to new phenomena. At this scale, the physics of the flow cannot be decoupled from the electrostatics arising from the electric charge at the fluid/solid interface. These effects combine to lead to new behaviors, known as interfacial phenomena. Cross-coupling electrokinetic phenomena, such as electro-osmosis, streaming currents and diffusio-osmosis, are the prime example of it. They originate in a net surface charge in the diffuse layer close to a surface, which we describe now. Electro-osmosis and streaming currents, which convert mechanical power into electrical power, will be presented next. Diffusio-osmosis will be part of the subsequent section related to osmosis.

1.1.1 Building up of the electrical double layer

Because of dissociation and adsorption occurring at the interface between a solid surface and an electrolytic solution, the fluid exhibits a non-zero local electric charge on a few nanometers from the wall [10]. Starting from the wall, we first encounter non-hydrated specifically adsorbed co-ions (and a few similar counterions), followed by hydrated counterions which are also bounded to the surface. Together, they define the Stern layer (see Fig. 1.1). After this comes the slip plane, from which starts the diffuse layer with mobile co-ions and counterions. The surface electric charge is not totally screened by the Stern layer, which causes the diffuse layer to carry more counterions than co-ions, and thus, to carry a net ionic current when in motion.
The local electric charge in the vicinity of a surface translates in an electrostatic potential ψ, which, if the surface potential is sufficiently small, obeys the linearized Poisson-Boltzmann equation

$$\frac{\mathrm{d}^2\psi}{\mathrm{d}x^2} = \frac{1}{\lambda_\mathrm{D}^2}\psi, \tag{1.1}$$

where x is a direction perpendicular to the wall, and $\lambda_\mathrm{D} = \left(\frac{\epsilon k_\mathrm{B} T}{\mathrm{e}^2 \sum_i \rho_i z_i^2}\right)^{1/2}$ with ϵ the permittivity, ρ_i the ionic concentration, z_i the valence of the specie i, e the elementary charge, k_B the Boltzmann constant and T the temperature. The electrostatic potential and the local electric charge thus decay exponentially over a distance given by the Debye length λ_D, see Fig. 1.1. λ_D is the characteristic size of the electrical debye layer (EDL), defined as the union of the Stern layer and the diffuse layer. The Debye lenght is typically of the order of a few nanometers, for moderate electrolyte concentration. For nanometric channels of radius a, filled with an ionic solution under a certain concentration, $a < \lambda_\mathrm{D}$ and one speaks about EDL overlap. Exotic effects appear in this regime, such

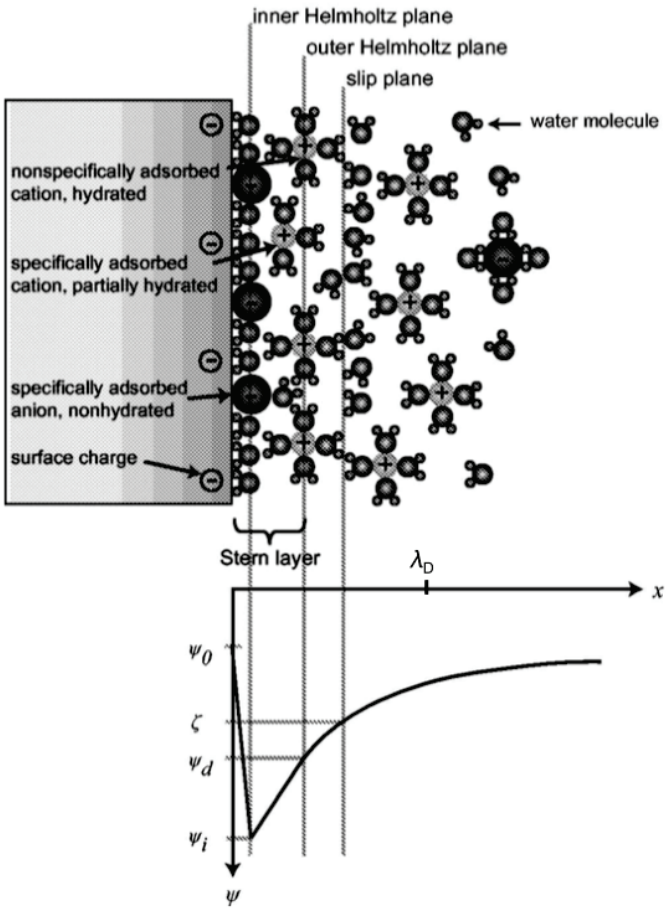

FIGURE 1.1: Layer diagram at the solid-electrolyte interface, with the corresponding electrostatic potential evolution $\psi(x)$. Here the surface potential ψ_0 is assumed to be negative, which corresponds to a negative surface charge. Reproduced from [10].

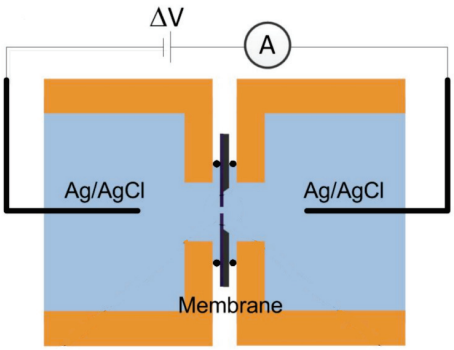

FIGURE 1.2: Schematic of an electrochemical cell, with a nanochannel drilled in a membrane, linking two reservoirs. Reproduced from [12].

as permselectivity [8], which will not be addressed in this thesis.
In case of higher surface potentials, non-linearities in the Poisson-Boltzmann equation have to be taken into account [11], which will not be considered here.

1.1.2 Electro-osmosis

Let us now consider a nanochannel linking two macroscopic reservoirs, as in Fig. 1.2. A voltage drop is imposed between the reservoirs, via two electrodes, which results in an ionic current inside the nanochannels. Cations are transported toward one electrode, anions toward the other one. This ionic current will be the subject of the chapter 2, in which the impact of interactions between nanochannels will be considered.
Within the diffuse layer, the excess of counterions results in a net ion momentum. By viscosity, this momentum is communicated to the water molecules surrounding them, then to the whole fluid. A net solvant flow can therefore be recorded (see for example [13] or [14]).

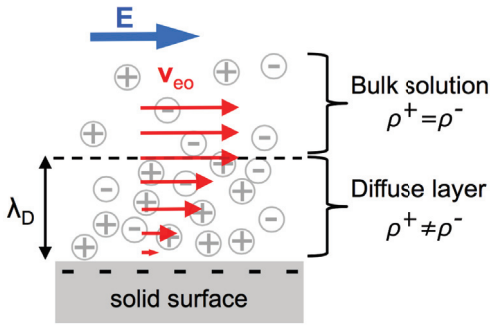

FIGURE 1.3: Principle of electro-osmotic flow generation: under an applied potential drop, prevailing cations (in case of a negatively charged interface) in the diffuse layer lead the fluid by viscosity, resulting in a net liquid flow. ρ^+ and ρ^- denote the cation and anion concentration respectively. Adapted from [13].

This phenomenon, depicted in Fig. 1.3, is known as electro-osmosis. Apart from nanofluidic laboratories, it is used as a wall-dehumidification technique.

1.1.3 Streaming current

Conversely, under an applied pressure drop between the two reservoirs, a flow sets in. The ratio between the flow and the pressure drop is the hydrodynamic permeability, which we will study in chapter 3 for a cluster of pores. We will see that as ionic conductance, permeability is affected by interactions at nanochannel entrances.
The liquid flow leads the electrically diffuse layers with it, which results in a measurable ionic current in the channel, provided the electrical circuit is a closed loop. This ionic current is a cross phenomena known as streaming current, see Fig. 1.4. As electro-osmosis, this effect does

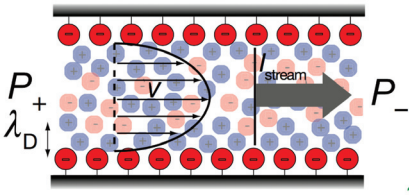

FIGURE 1.4: Principle of streaming-current generation: under an applied pressure drop, liquid flows in the nanochannel. The moving diffuse layer involves a net ionic current. Reproduced from [15].

not need EDL overlap to be perceptible. In the case where $a \gg \lambda_D$, the streaming current reads [14]

$$I_{ST} = -\frac{\pi a^2}{\ell}\frac{\epsilon\zeta}{\eta}\Delta P, \tag{1.2}$$

with a and ℓ the channel radius and length, ϵ the fluid permittivity, ζ the value of the electrostatic potential at the slip plane and η the fluid viscosity.

This method is envisioned to produce electrical power from a mechanical source [16], with possible enhancement coming from the addition of polymer in water [17]. However, pressure-driven streaming currents reach lower values than diffusio-osmotic currents [15]. To the best of our knowledge, energy conversion by streaming currents has not been tested on a large scale.

In chapter 4, we provide scalings for the streaming current output power and efficiency. We show that interactions at pore entrance have a huge impact on the scaling when nanochannels are massively parallelized.

We now come to osmosis related phenomena, which display water transport under a concentration gradient.

1.2 Osmosis related phenomena

Osmosis is the spontaneous flow of water (or solvent) molecules through a semi-permeable membrane into a region of higher solute concentration. Its discovery is the fact the cleric Abbé Nollet back in 1748, who observed water passing through an animal bladder and diluting alcohol, but never the contrary [18]. Osmosis is crucial in living systems, as most biological membranes are semipermeable. Osmosis is the first mean by which water is transported in and out of the cells.
Semi-permeable membranes exclude ions thanks to very short-range interactions, such as steric effects. Water molecules being smaller than hydrated ions, water alone can pass through the nanometric or sub-nanometric pores of the membrane.
In this thesis, we will deal with unconventional osmosis phenomena, which, strictly speaking, involve no semi-permeable membranes. Rather, the semi-permeable role will be undertaken by the diffuse layer (in diffusio-osmosis) of by a vapor bubble (in phase-change osmosis). Now, we first present the basic concepts under osmosis before turning to its applications in desalination and energy conversion.

1.2.1 Osmotic pressure

The osmotic pressure $\Delta\Pi$ is the mechanical pressure drop required to prevent the spontaneous water flow through a semi-permeable membrane separating two reservoirs of different solute concentrations. For ideal dilute solutions, the mechanical pressure to be applied on the more concentrated side, to prevent spontaneous water flow, can be calculated as [19]

$$\Delta\Pi \approx -\Delta\rho\, k_{\mathrm{B}} T \tag{1.3}$$

where $\Delta\rho = \Delta\rho^+ + \Delta\rho^-$ is the concentration difference taking all solvated species into account (in m^{-3}) between the two sides of the membrane. $\Delta\rho^+$ and $\Delta\rho^-$ respectively refer to the cation and anion centration difference.

In a more general way, the osmotic pressure corresponds to a solvent chemical potential difference. Solvent chemical potential is higher on the less concentrated side (the feed solution) than in the more concentrated side (the draw solution), hence if no mechanical pressure counterbalances this chemical potential drop, solvent flows from the feed to the draw solution as in Fig. 1.5 (top situation). In this case, water dilutes the draw solution until concentrations on both sides of the membrane are in balance (or, if an hydraulic pressure builds up, until it balances the osmotic pressure).

To understand how mechanical and chemical energies can be converted into each other through osmotic processes, we consider the situation depicted in Fig. 1.5. Suppose the high- and low-concentration liquids are in 2 boxes closed by 2 pistons, and separated by a semi-permeable membrane. The pistons can move if the pressures on their inner and outer sides do not equilibrate. As water is an incompressible liquid, it is intuitive that while the osmotic dilution takes place, both pistons are displaced by the solvent flow. The chemical energy stored in the concentration gradient is therefore converted into mechanical energy, which produces work to move the pistons. In this sense, semi-permeable membranes can be seen as a transducer.

Note that if an excess pressure $\Delta P < \Delta\Pi$ is applied on the concentrated side, its dilution sill occurs until a concentration drop $\Delta\rho' = \Delta P/k_B T$.

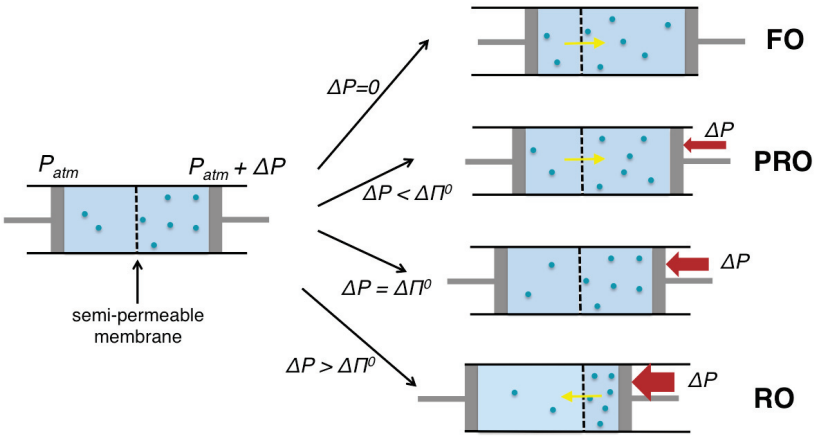

FIGURE 1.5: Principle of osmosis methods to purify water or generate mechanical power. $\Delta\Pi^0$ is the osmotic pressure computed in the initial state. The forward osmosis (FO), pressure-related osmosis (PRO) and reverse osmosis (RO) are illustrated. They only depend on the pressure drop ΔP applied between the reservoirs. If $\Delta P = \Delta\Pi^0$ (third situation), no net flow is observed. Note that in FO, PRO and RO, equilibrium is reached when $\Delta P = \Delta\Pi^f$ the osmotic pressure in the final state.

1.2.2 Forward osmosis

Osmotic pressure has a direct application, known as forward-osmosis, used in water treatment and desalination [20, 21]. For now it is referred to as an emerging technology [22], whose main advantage is a low energy input, as no (or low) hydraulic pressure is applied on the draw solution. There are two ways to use this technique. Either brackish or sea water is diluted by fresh water, thereby decreasing its impurity level and mineral content. The second possibility is is that fresh water be extracted from sea water using a draw solution of lower water chemical potential. In the second case, ammonia-carbon dioxide solutions were used with some

success [23]. Of course, the electrolyte in the draw solution must be easily separable from water in a subsequent treatment.
As all the membrane-based methods, forward osmosis is hindered by a phenomenon known as *concentration polarization*. Because of the difference in ion mobility in the membrane phase and in the solution, in the steady state the ion concentration close to the membrane differs from that in the bulk [24]. This is referred to as external concentration polarization. It can be reduced by increasing flow velocity (parallel to the membrane) and turbulence at the membrane [20]. In forward-osmosis, asymmetric membranes are used, which comprise an active layer and a porous supporting layer. Again, the ion mobility between the bulk and the supporting layer differs, which results in a concentration gradient inside the supporting layer. Consequently, the concentration gradient across the active layer, is reduced compared to the concentration difference between the two bulk solutions. The water flow through the membrane is thus reduced. This phenomenon, known as internal concentration polarization (ICP) cannot be handled through physical means like mixing [20]. It has to be solved in membrane design. One of the main challenge faced by forward osmosis is thus the production of high-performance membranes.

1.2.3 Pressure-retarded osmosis

A second application of osmosis is pressure-retarded osmosis, used to generate energy from a salinity gradient [25, 26]. The principle is the same than in forward osmosis, but sea-water is pressurized at 65 to 85% of $\Delta\Pi$ which "retards" the water permeation from the low-concentration to the high-concentration side. Yet this water flow expands the draw solution volume, from which a turbine extracts work to generate electrical energy. A simplistic schematization of this process

is given in Fig. 1.5 (second case). This method was considered very seriously by the Norwegian company Statkraft. A pilot power-plant conducted real-scale tests during 3 years, but they were halted in 2013 as competitiveness with existing renewable energies was not judged attainable in a foreseeable future. In fact, pressure-retarded osmosis faces similar challenges as forward osmosis: ICP and fouling. The design of low-cost, robust, highly selective yet enabling a high water flow, and reducing-ICP membranes is still a bottleneck. Moreover, it has be shown that this technique does not allow high power density together with high efficiency [27]. As pre-treatment of sea-water and river-water consumes a major part of the produced power, closed-loop pressure-retarded osmosis has been proposed [28]. Yet, clever ideas are still needed to make pressure-retarded osmosis an industrially relevant method.

1.2.4 Reverse osmosis

We now come to reverse osmosis, a famous application where mechanical pressure compresses the high-concentration solution above the osmotic pressure. This process is nowadays the leader one in desalination, as it has the lowest energy cost [29, 30]. It accounts for 41% of the total desalinated water volume.

Reverse osmosis consists in extracting water from sea-water or a brine to feed the fresh water side, see Fig. 1.5 (bottom situation). Additionally, it was proposed that the very concentrated residual from reverse osmosis be used as the draw solution in pressure-retarded osmosis, leading to promising power densities [28].

Once more, the development of more suitable membranes, preventing scale and fouling, is the main challenge. Moreover, as in all the already

mentioned membrane-based methods for desalination or energy harvesting, the use of sub-nanometric pores is required to prevent ions from crossing the semi-permeable membrane. This selectivity imperative has a direct cost, as fabricating such membranes on a large scale is complex and expensive, and a hydrodynamic cost as it considerably hiders water permeation [7]. Indeed, in a Poiseuille flow, permeability scales like the radius to the fourth and is thus very sensitive to the pore size. Carbon nanotubes are considered as very serious candidates to replace the current polymeric or inorganic membranes, as they exhibit greatly enhanced flow [29, 31]. Zeolites and porous graphene are other possible alternatives [32].
The phase-change based osmosis method studied in Chapter 5 ressembles reverse osmosis, but it enables the use of bigger pores, of typical radius $a \sim 10 - 100$ nm. As transport through a vapor phase is less efficient than in a liquid phase, water permeability may not be enhanced compared to reverse osmosis, but such membranes could be financially more attractive. Moreover, bigger pores are less prone to fouling than sub-nanometric ones.

1.2.5 Diffusio-osmosis

We end this paragraph by diffusio-osmosis, an unconventional osmosis method as it does not rely on a semi-permeable membrane.
In bulk solution in presence of a concentration gradient, solutes diffuse according to Fick's law, but of course there is not net flux of solvent toward the more concentrated part. This is because the solvent pressure always adapts, in order to keep the total pressure constant everywhere in the bulk [33]. In other words, the solvent pressure compensates the osmotic pressure.

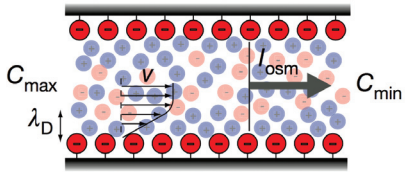

FIGURE 1.6: Principle of diffusio-osmotic current generation: under an applied salt concentration drop between the reservoirs, a salt concentration gradient builds up. Inside the nanochannel, the concentration gradient within the diffuse layer differs from that far from the interface. In the diffuse layer, an unbalanced osmotic pressure sets in and drives a liquid flow from the less concentrated to the more concentrated side. The moving diffuse layer involves a net ionic diffusio-osmotic current. Reproduced from [15].

Inside a nanochannel linking two reservoirs with different salt concentrations, this picture only holds far from the solid-liquid interface. In the diffuse layer close to the interface, ion concentration differs from the bulk because of the electrostatic potential ψ that builds transversally, over a distance given by the Debye length (see Fig. 1.1). It can be shown that a non-compensated osmosis pressure $k_B T[\rho^+(x,z) + \rho^-(x,z) - \rho^0(z)]$ builds in the diffuse layer, denoting $\rho^0(z)$ the bulk concentration and ρ^+ and ρ^- the local cation and anion concentrations. The pressure variation along the nanochannel axis z generates a viscous flow according to Stokes equation, called the diffusio-osmotic flow, see fig 1.6. For more details about the calculations, see [13, 15].
Like in streaming current, the moving charged diffuse layer leads a net ionic current, given by [15]

$$I_{DO} \approx \frac{2\pi a \Sigma}{\ell} \frac{k_B T}{\eta \lambda_B} \Delta \log \rho^0 \tag{1.4}$$

with Σ the excess surface charge remaining after the Stern layer has established and λ_B the Bjerrum length, a typical nanometric lengthscale

[8]. For a monovalent salt it is defined as

$$\lambda_{\mathrm{B}} = \frac{e^2}{4\pi\epsilon k_{\mathrm{B}} T} \tag{1.5}$$

and at ambient temperature, $\lambda_{\mathrm{B}} = 0.7$ nm.
As semi-permeable membranes in traditional osmosis processes, the diffuse layer at a solid-liquid interface can play the role of a transducer. It converts mechanical or chemical energy into electrical energy, depending on the considered mechanism: streaming or diffusio-osmotic current.
Diffusio-osmotic currents share common features with streaming currents, as they both belong to cross-coupling phenomena, which originate in electrokinetic effects at a solid-liquid interface. However, several aspects point in favor of diffusio-osmotic currents. First, it is possible to achieve a high osmotic pressure drop within the diffuse layer, whereas nanochannel fragility does not sustain as high a mechanical pressure drop. In consequence, diffusio-osmotic currents reach higher values than their streaming counterparts. Moreover, diffusio-osmotic currents take more advantage of a high excess surface charge Σ than streaming currents [15]. In this sense, boron-nitride nanotubes were recently identified as a good candidate for energy harvesting [15, 34].

Contrary to pressure-retarded osmosis and reverse osmosis, diffusio-omotic currents have not been tested on a real scale yet. In this thesis, we furnish first-order elements for the scaling up of diffusio-osmotic currents in chapter 4. Thanks to the results of chapter 2 on ionic conductance, which will be shown to be transferable to salt diffusive flux, and also of the results of chapter 3 on hydrodynamic permeability, we will calculate the cross coefficient linking the concentration difference to the diffusio-osmotic current. Its scaling with the number of nanochannels is not self-evident, in view of interaction-modified entrance effects.

1.3 Distillation methods

Phase-change based processes have been extensively used for desalination, even though they now tend to be outdone by reverse osmosis. All current methods rely on evaporation. Already, around 400 BC, Hippocrates taught his students that vapor produced from seawater when condensed is no longer salty. In fact, because of the high dehydration energy required to strip its solvation shell to an ion, salt stays in the liquid phase while pure water evaporates. However, distillation methods have a high energetic cost because of the large water specific heat.
The phase-change osmosis device presented in chapter 5 bears some similarities with membrane distillation, which will be presented in the following. We first mention the two main distillation methods used in desalination, multi-stage flash and multi-effect distillations, even though they do not present nanoporous materials.

1.3.1 Multi-stage flash distillation and multi-effect distillation

Still the most in use, multi-stage flash distillation (MSF) accounts for 44% of the worldwide installed desalination capacity [29]. Sea-water transits in several chambers of decreasing pressure, where it undergoes flash evaporation (*i.e.* evaporation because of a pressure reduction), see Fig. 1.7.

In multi-effect distillation (MED), water evaporates on the surfaces of hot vapor supply pipes at several stages. The steam is collected into the tubes of the next stage, heating and evaporating more water, see Fig. 1.8. Economically speaking, MED is competitive with MSF [29].

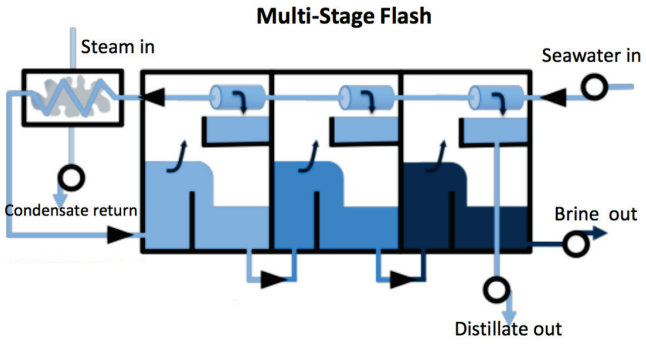

FIGURE 1.7: Schematic diagram of the MSF technology. From left to right, the three chambers have a decreasing pressure and temperature. Seawater is first heated through the three chambers (from right to left) and the brime heater (to the left), before flowing back in the chambers where it undergoes flashing. At each of the 6 steps, a distillate is extracted. The blue color intensity represents the water salinity, from light (distillate) to intense (brine). Reproduced from [29].

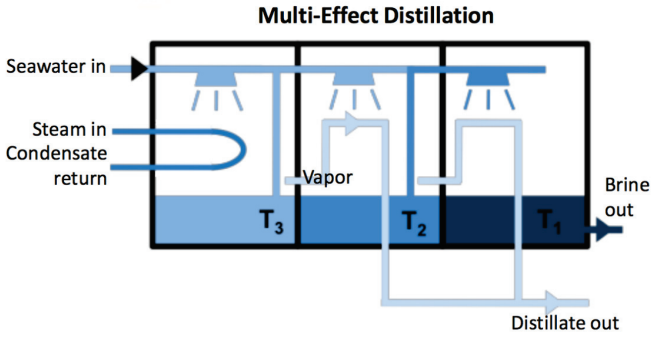

FIGURE 1.8: Schematic diagram of the MED technology. Water undergoes three stages. Sprayed from above, part of it evaporates on the steam tube and is re-used in the next chambers to generate more vaporization. The blue color intensity represents the water salinity, from light (distillate) to intense (brine). Reproduced from [29].

MSF and MED plants have a large capacity. These techniques benefit from a high purity permeate and an energy cost nearly independent of water salt concentration.

1.3.2 Membrane distillation

For smaller scale applications, other techniques are used. One of them is membrane distillation, where elevated (50-90°C) temperature salted water and low temperature fresh water are introduced on either sides of a hydrophobic porous membrane [29, 35]. Water evaporates from the concentrated side and condensates into the fresh water side. This method suffers from lower permeate flux compared to other separation techniques such as reverse osmosis, and concentration and temperature polarization effects which reduce the flow. It has not been implemented on a wide scale and need further development.

The desalination method we will present in chapter 5 stems from osmosis processes and membrane distillation. As in membrane distillation, water evaporates at the brine side and condensates at the fresh water side. However the process is not thermally driven, but mechanically driven as in reverse osmosis, or osmotically driven as in forward osmosis.

1.4 Electrostatic separation

Charge-based separation methods are well-suited for treating low-salinity water, in which case they require lower energy input than reverse osmosis or distillation. They are currently used for small-scale production of drinking and pure water [29]. These methods are given for information purposes only, and will not be exploited in the remaining of this thesis.

1.4.1 Electrodialysis

In electrodialysis, ions are transported by an applied electric field, which drives ions according to their charge. Moreover, cation and anion selective membranes allow or prevent ion flow. These membranes are made of polymers exhibiting charged groups, to which a counterion is attached. Under an applied electric field, the counterion has a high mobility and can be replaced by any ion of the same charge, allowing the passage of only anions or cations through the membrane. [36]. This phenomenon is known as ion exchange. The alternate arrangement of ion selective membranes results in alternate brine and partially demineralized water, see Fig. 1.9.

1.4.2 Capacitive deionization

Other electrostatic-interaction based desalination techniques include capacitive deionization. It involves a different mechanism, as ions are not transported toward an electrode like in electrodialysis, but adsorb on a imposed-potential surface [37, 38]. The purified solution is then flushed.
Capacitive deionization is an active research domain, much efforts being devoted to the achievement of the right material to build the electrodes from.

1.4.3 Reverse electrodialysis

Reverse electrodialysis setup is very similar to electrodialysis one, but the purpose is right inverted. To generate an ionic current, draw solutions

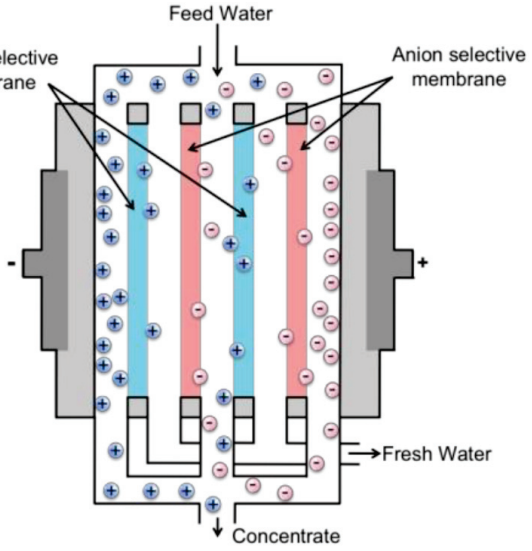

FIGURE 1.9: Schematic diagram of electrodialysis desalination system, with cation (blue) and anion (red) selective membranes. Reproduced from [29].

(salted water) and feed solutions (fresh water) are introduced in alternate cells, separated by cation and anion specific membranes. Under the chemical potential difference, ion exchange between the electrolyte and the membranes takes place. It results in a salt enrichment on the feed side and salt impoverishment on the draw side, and in an ionic current. At both ends of the stack, electrodes convert the ion flux into an electrical current, provided to an external circuit [27, 28].
Unlike pressure-retarded osmosis, chemical energy is directly converted into electrical energy. Several companies are testing this method and a power plant relying on reverse electrodialysis is to be built in the Netherlands.

1.5 Summary

To summarize, we recall here the salinity-gradient based energy-conversion methods we have superficially covered in the previous paragraphs:
• Pressure-retarded osmosis, which was tested on a wide scale but abandoned two years ago
• Reverse electrodialysis, about to be tested on a wide-scale
• Diffusio-osmosis, in development
• Streaming currents (electricity from hydraulic pressure), under consideration.

As for desalination, we reviewed
• Reverse osmosis, the most advanced and most widely used technique
• Multi-stage flash distillation, older than reverse osmosis and still in use especially for highly saline brines to be desalinated
• Multi-effect distillation, competitive with MSF
• Electrodialysis, a niche technology used in small device
• Forward osmosis, membrane distillation, and capacitive deionization, still in a development stage.

The remaining of this thesis consists in 4 chapters, the last one being totally independent from the 3 others.
In chapter 2, we focus on the ionic conductance of an array of interacting nanopores. We experimentally show that conductance scales sub-linearly with the number of pores, because of long-range electrostatic interactions between pore entrances. This result is supported by a scaling analysis and numerical finite-element calculationss.
Then, in chapter 3, interacting pores are studied for their global hydrodynamic permeability. Unlike ionic conductance, hydrodynamic

permeability keeps a linear behavior while interactions only add corrections to entrance effects. The experimental results presented in this chapter are in very good agreement with an existing model.
These two chapters contain preliminary results which will be used in chapter 4 to predict the behavior of streaming current and diffusio-osmotic currents in large-scale membranes. Output electrical power and efficiency show *a priori* unfavorable scalings, not taking into consideration any experimental sophistication. These results highlight the non trivial aspect of scaling up "good properties" encountered at the nanoscale.
Chapter 5 is devoted to molecular dynamics simulations originating in a recent proposition of a new desalination device by Karnik and his co-workers. The separation method is similar to reverse osmosis, but the semi-permeable membrane is replaced by a gas bubble trapped in a hydrophobic nanochannel. The dynamics of the process is studied, along with its dependency against geometrical parameters, showing good agreement with a Knudsen-diffusion based model. Then, by computing the free energy barrier encountered by an ion approaching and penetrating the gas phase, we show that ion impermeability is ensured for channel length above a minimal value, of the order of the channel radius.

Chapter 2

Ionic conductance of solid-state nanopore networks

Contents

2.1 Ionic currents in nanopores

Solid-state nanopore membranes are well-known for their powerful applications in multiple domains, in particular in biology, as low-cost biosensors [39], but also in engineering as devices for filtering or for the generation of energy [15, 29, 40]. A biosensor is made of a nanopore connected to two fluid reservoirs, between which a potential or pressure drop is imposed. The particles in solution are driven through the nanopore, where their passage temporarily blocks the flow of ionic current. It is thus possible to detect biological components, such as proteins, by measuring the ionic current crossing the nanopore [41–45]. This is expected to achieve fast and low-cost sequencing of DNA [39]. Furthermore, in the context of desalination or energy conversion, multipore membranes also raise great hopes to increase the efficiency of the process [46, 47]. The passage through the ultrathin nanopores is a key to their unique properties: it provides high sensitivity to molecular passage, as well as enabling the building up of huge potential and chemical gradients across the thin membranes which facilitates the

passage [48]. In this context, pierced graphene constitutes the ultimate membrane, yielding great expectations for applications [32, 49–51].

In this thesis, we use the terms "nanopore" and "nanochannel" assigning them different meanings. Nanochannel is considered as a generic term, whereas nanopore refers to a nanochannel with a small aspect ratio (*i.e.* a channel length comparable to or smaller than the nanochannel lateral dimensions). This terminology is convenient here, but differs from the common use of "nanopore" in any situation.

Success in using nanopores lies in a proper understanding of transport properties of molecules, but also of ionic current signals through the nanopores, which is commonly used as a probe of macromolecule transport [52]. In the first two chapters of the present thesis, we have a special interest in electrokinetic transport in nanochannels, with the prospect of energy harvesting at a macroscopic level. This requires a deep understanding of ionic current signals at nanochannel (or nanopore) entrances where interactions take place. To scale up good properties at the nanometer scale, towards marketable membranes, the effects of electrostatic interactions between pores on the global conductance must be understood and mastered.

In this chapter, we report a non-extensive, sub-linear scaling of the conductance of N pores, due to long-range mutual interaction across an array of nanopores. We present theoretical, numerical and experimental results aiming at measuring and predicting this behavior. The results presented here were published in [53].

In this first section, we review state of the art concerning ionic transport in nanopores. We define the access resistance, which is of major importance in nanopores (by contrast to long nanochannels) and which will turn to be modified by the presence of neighboring pores. Then, we precise how surface conduction intervenes at low salt concentration.

2.1.1 Inner and access resistances

The ionic resistance of a nanopore containing an ionic solution has two distinct origines. The first one is the resistance of the solution inside the channel. In mks units, the inner resistance of a cylindrical pore reads

$$R_{\text{channel}} = \frac{1}{\kappa_{\text{b}}} \frac{\ell}{\pi a^2}, \tag{2.1}$$

with κ_{b} the bulk conductivity of the solution, ℓ the pore length and a its radius. This expression stems directly from the mesoscopic Ohm's law $\vec{j} = \kappa_{\text{b}} \overrightarrow{E}$ with $\vec{j}$ the ionic current and $\overrightarrow{E}$ the electric field, considering the solution inside the pore as a uniform conductor. Under this assumption, Ohm's law becomes $\dfrac{I}{\pi a^2} = \kappa_{\text{b}} \dfrac{\Delta V}{\ell}$ from which Eq.(2.1) is recovered. Here ΔV is the potential drop in passive sign convention. When several pores are present in a membrane, each pore presents an inner resistance expressed as in Eq.(2.1). On the other hand, the second contribution to the pore resistance is modified by electrostatic interactions between pore.

The second and main contribution to the nanopore resistance comes from entrance effects, *i.e.* the convergence of field lines toward and outward the pore. As reservoirs on both sides of the pore are usually much bigger than the pore itself, one can consider that field lines converge from an hemispheric electrode at infinity toward a disk of radius a located at the pore entrance (and respectively field lines diverge from a disk of radius a toward infinity). This situation is depicted on Fig. 2.1-a. Following Vodyanoy and Bezrukov [54], the so-called access resistance is counted twice to account to both pore entrance and exit, and added to the channel inner resistance like resistances in series, see Fig. 2.1-a. We now turn to the computation of the access resistance for a single isolated pore.

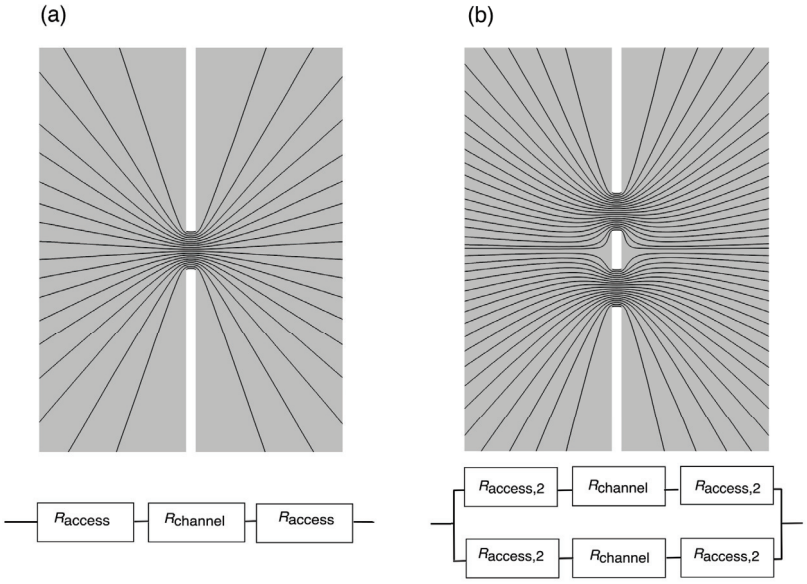

FIGURE 2.1: Electric field lines converging toward a single pore (a) or 2 pores (b) and the modeling in terms of electric resistance. Access resistances and channel resistance add up in series, but access resistance depends on the presence of other pores. Indeed, electrostatic interactions modify a pore access resistance by deforming converging and diverging field lines. Top images are courtesy of S. Gravelle.

Hille in 1968 [2], followed by Hall [3], first calculated the access resistance through a small circular pore in a membrane, by using an analogy between ion transport and an electrostatic capacitance problem. The key remark made by Hille and Hall is that the obeyed equations are identical in both cases: for ion transport, current conservation $\overrightarrow{\nabla} \cdot \vec{j} = 0$ and the mesoscopic Ohm's law result in a Laplace equation for the electrostatic potential:

$$\overrightarrow{\nabla}^2 V = -\frac{1}{\kappa_b} \overrightarrow{\nabla} \cdot \vec{j} = 0. \tag{2.2}$$

In a capacitance problem, the absence of electric charges between the electrodes also yields $\vec{\nabla}^2 V = 0$. Boundary conditions are in both case a given potential on the disk and at infinity. Consequently, the access electrical resistance for a single pore entrance is related to the capacitance C between a conducting disk of vanishing thickness, standing for the nanopore entrance, and a half-spherical electrode at infinity. This is expressed as

$$R_{\text{access}} = \epsilon\rho/C \tag{2.3}$$

with $\rho = \kappa_{\text{b}}^{-1}$ the resistivity of the medium. For a charged conducting disk of radius a in a half space, we have $C = 4\epsilon a$ [55], leading to

$$R_{\text{access}} = \frac{1}{4\kappa_{\text{b}} a} \tag{2.4}$$

(for one side of the pore). Adding this access resistance for the two sides of the pore to the bulk resistance of a cylindrical conductor, one can write the total conductance of an isolated pore as

$$G_1^0 = (R_{\text{channel}} + 2R_{\text{access}})^{-1} = \kappa_{\text{b}} \left[\frac{\ell}{\pi a^2} + \frac{1}{2a} \right]^{-1} \tag{2.5}$$

where the subscript stands for the number of pores, and the superscript ^{0} denotes that the pore is isolated. For pores of aspect ratio $\ell/a = 1/2$ such as the ones we use in this work, entrance effects are of the same order of magnitude as channel resistance, yet dominant as $R_{\text{channel}}/2R_{\text{access}} = 1/\pi$. The shorter and wider the pores, the more access resistance prevails over channel resistance.

Formula (2.5) works for moderate to highly concentrated solutions of KCl; at low concentrations, surface conduction effects become dominant over the bulk conduction, leading to an anomalous saturation of the conductance [12]. This effect will be briefly exposed in the next section.

More sophisticated approaches also take into account the concentration gradients in pore entrances [56], and require solving explicitly the Poisson-Nernst-Planck equations. However they do not predict appreciable deviations from Hall's formula, at least in neutral or weakly charged membranes [57]. We will see in the next section that this is actually the case in our work. Finally, geometrical effects could also be accounted for, in particular by taking into account the hourglass-like shape of some solid-state nanopores, as shown by Kowalczyk and coworkers [58]. Yet, as we will describe later in section 2.4.1, we ensured that the 200-nm radius pores we used had an accurate cylindrical shape.

2.1.2 Surface conduction effects in nanopores

At low salt concentration, solid-state nanopores show an unexpectedly large ionic conduction. This effect originates in the presence of a non-neutral diffuse layer close to the membrane surface, which couples to three-dimensional entrance effects at pore mouths. Note that the large ionic conduction at low salt concentration is a well known effect in *nanochannels* [8, 10, 59], but paradoxically its interpretation for *nanopores* is much more delicate as nanopores cannot be reduced to a one-dimensional view contrary to nanochannels. Here, we present the main results obtained by C. Lee and coworkers in [12].

Due to adsorption and dissociation of chemical species on the surface, the membrane surface is electrically charged and surrounded by partially-hydrated and hydrated counterions which are bound to the surface [60]. This defines the Stern layer, and following Schoch *et al.* [10] we call effective surface charge Σ that which remains after the Stern layer has established. Beyond the Stern layer, in the solution, an excess of mobile counterions builds up in the so-called diffuse layer, to maintain

electroneutrality. The surface conductivity κ_s relationship with effective surface charge can be estimated as

$$\kappa_s \approx e\mu|\Sigma|, \tag{2.6}$$

with e the elementary charge and μ the ions mobility expressed in $m^2.C^{-1}.V^{-1}.s^{-1}$ (we consider here K^+ and Cl^- which are supposed to have the same mobility), see [12] for details. This approximation does not take into account any electro-osmotic contribution, the importance of which is under debate for nanopores [61, 62]. On the other hand, the bulk conductivity of a KCl solution is given by $\kappa_b = 2e^2\mu\rho_s$ with ρ_s the ionic density in m^{-3}.

The electrical conductance of the diffuse layer is negligible compared to the bulk conductance for high salt concentration c_s, typically $c_s > 10^{-2}$ mol/L in our work. To describe accurately the prevalence of bulk or surface conduction over the other, one has to refer to the Dukhin length l_{Du},

$$l_{Du} = \frac{\kappa_s}{\kappa_b} \approx \frac{|\Sigma|/e}{2\rho_s}. \tag{2.7}$$

At low concentration, l_{Du} overtakes the pore radius a and surface conduction is predominant. To feed this type of conduction, ions from outside the pore are driven toward the entrances which results in anomalous entrance effects. Indeed, surface conduction modifies electric field lines and current stream lines deep outside the nanopore, over an extension given by the Dukhin length, see Fig. 2.2-c. As a consequence, entrance effects are modified by the predominance of surface over bulk conduction inside the nanopore. Experimentally speaking, this translates in a plateau in pore conductance at low salt concentration, in place of a linear decrease proportional to κ_b, see Fig. 2.2-a.

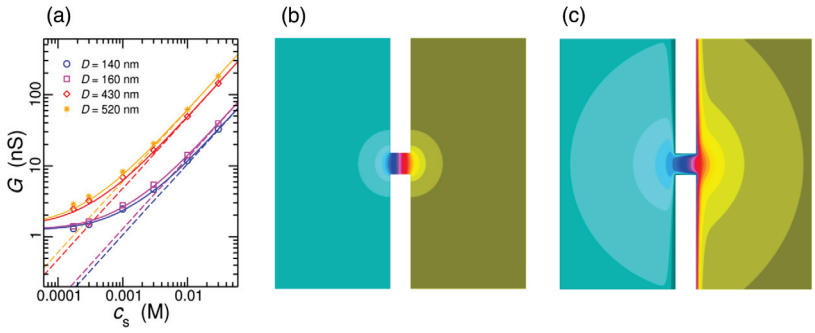

FIGURE 2.2: (a) Conductance of solid-state nanopores of diameter D and surface charge $\Sigma = 20$ mC/m^2, from finite-element simulations. Dashed and solid lines are predictions using Eq.(2.5) and Eq.(2.10) respectively. (b) Contour lines of the electric potential across a typical pore ($L = D = 100$ nm) without surface charge and (c) with surface charge (Dukhin length $l_{\mathrm{Du}} \sim 3D$). Images from [12].

The theoretical model proposed by Lee *et al.* [12] (from which we only recall the results) to account for this plateau adds a surface component not only to the inner pore conductance, but also to the access term:

$$R_{\mathrm{channel}} = \left(\kappa_{\mathrm{b}} \frac{\pi a^2}{\ell} + \kappa_{\mathrm{s}} \frac{2\pi a}{\ell} \right)^{-1} \tag{2.8}$$

$$R_{\mathrm{access}} = \left(4\kappa_{\mathrm{b}} a + 2\kappa_{\mathrm{s}} \right)^{-1} . \tag{2.9}$$

After some straightforward manipulations, this results in

$$G_1^0 = \kappa_{\mathrm{b}} \left[\frac{\ell}{\pi a^2} \frac{1}{1 + 2\frac{l_{\mathrm{Du}}}{a}} + \frac{1}{2a + l_{\mathrm{Du}}} \right]^{-1} . \tag{2.10}$$

The second term in Eq.(2.10) means that from the outside, the pore has an effective size $a_{\mathrm{eff}} = a + l_{\mathrm{Du}}/2$. For low salt concentration, $l_{\mathrm{Du}} > a$ and the effective size can be much bigger than the pore radius. This is clearly seen in Fig. 2.2-c. Moreover, in the infinitely low concentration

limit, the saturation of the conductance is given by

$$G_1^0(l_{\mathrm{Du}} \to \infty) = \kappa_{\mathrm{s}} \left(\frac{2\ell}{\pi a} + 1 \right)^{-1} \tag{2.11}$$

which only depends on the aspect ratio ℓ/a, and not explicitly on the pore diameter. Counterintuitively, small pores and large ones can conduct as efficiently at low salt concentration.

In this work, we stick to the high-concentration regime where the Dukhin length is small compared to the pore size. Surface conduction effects can be neglected, which simplifies the study of electrostatic interactions that we undertake.

2.1.3 Electrostatic interactions between nanopores

In the following of this chapter, we raise the question of ionic transport through an array of multiple nanopores. While naïve expectations would suggest that the total ion conductance G_N should scale as the number N of pores, we report experimental results for arrays with $N = 1 \dots 50$ pores showing that the conductance per pore G_N/N strongly decreases with the number of pores N, with $G_N/N \to 0$ as $N \to \infty$.

This anomalous sublinear scaling of the conductance originates in electrostatic interactions at pore entrances which affect entrance effects. The modified access resistance translates visually in the modification of the curvature of streamlines at pore entrances, when a neighboring pore is present, see Fig. 2.1-b page 29. The purpose of this chapter is to predict and measure such modified access resistance, and to discuss its consequences.

The sublinear scaling of the conductance is supported by a scaling analysis of ion transport, presented in the next section. Then, this

analysis is successfully compared to numerical and experimental results in the third and fourth sections. Consequences of this counter-intuitive result are discussed for ionic - but also diffusive and thermal - transport across membranes in the final discussion 2.5.

2.2 From 1 to 2, to many pores: a scaling analysis

We build our approach in the spirit of Hall's work [3] and generalize Eq.(2.5) to the case of multiple pores. Following the reasoning exposed in 2.1.1, the overall access resistance $R_{N,\mathrm{access}}$ of one side of the pore array can be obtained directly from the corresponding capacitance of N conducting (and electrostatically connected) disks, as

$$R_{\mathrm{access,N}} = \frac{1}{\kappa_{\mathrm{b}}} \times \frac{\epsilon}{C_{\mathrm{Npores}}}. \tag{2.12}$$

In the following sections, we derive the expression of C_{Npores}.

2.2.1 Two pores

Before exploring the general N-pore case, we first consider the 2-pore geometry. In this case the calculations proceed easily by a simple electrostatic analogy. The calculation of the 2-disk capacitance separated by a distance L can be estimated recursively. We fix the potential V_0 on the disks and compute their charge. For $L \to \infty$, the charge held by each pore entrance tends to that of isolated pores, *i.e.* $q = 4\epsilon a V_0$. For finite L, their charge will depend on the interspacing L in order to maintain two neighboring conducting disks at the same potential, due to mutual electrostatic interaction. Corrections will add to the

charge q, which we write $\delta q^{(i)}$ for the i-th order correction. We make the standard simplifying assumption that the effect of a given disk can be approximated by the effect of a point charge located at its center. This assumption is expected to hold when $L \gg a$ (as may be indeed verified numerically).
In this case, the image charge $\delta q^{(1)}$ held by a disk at V facing a point charge q is simply $\delta q^{(1)} = -q\frac{a}{L}$ [55]. Symmetrically, both disks now hold $q + \delta q^{(1)}$. As $\delta q^{(1)}$ was the correction accounting for a charge q, we now need a correction $\delta q^{(2)}$ to account for an extra charge $\delta q^{(1)}$, and so on. Next orders can be calculated along the same method and within the above approximation, this leads to $\delta q^{(n)} = q \times (-a/L)^n$, so that the total charge on a single disk is accordingly estimated by summing up all contributions as $Q = \sum_n \delta q^{(n)} = q/(1 + a/L)$. The global access ionic resistance of the two pores is deduced accordingly

$$R_{2,\text{access}} \simeq \frac{1}{4\kappa_\text{b}\, a}\left(1 + \frac{a}{L}\right) \tag{2.13}$$

and the two pores conductance is

$$G_2 = 2\kappa_\text{b}\left[\frac{\ell}{\pi a^2} + \frac{1}{2a_\text{eff}}\right]^{-1} \tag{2.14}$$

where $a_\text{eff} \simeq a/(1 + a/L)$ has the meaning of an effective electric size of the pores, modified under their mutual influence.

2.2.2 N pores: general framework

Let's generalize this result to N pores. In that case, the charge correction factor may be different for each pore, but we consider only (averaged) global properties in the present estimates. As above the conductance

may be written as

$$G_N = N\kappa_{\rm b}\left[\frac{\ell}{\pi a^2} + \frac{1}{2a_{\rm eff}}\right]^{-1} \tag{2.15}$$

where the effective electric size of the pore now takes the general expression

$$a_{\rm eff} \equiv a \times \frac{C_{\rm N\ pores}}{NC_{\rm single\ pore}}. \tag{2.16}$$

Following the capacitance analogy, the effective electric size $a_{\rm eff}$ is defined in terms of the capacitance $C_{\rm N\ pores}$ of the N pore system.
We are not aware of a general analytical estimate for $C_{\rm N\ pores}$ and we therefore proceed along the same lines as for the two pore case above, with an estimate of the charge carried by each conducting disk (the pore entrances) in order to keep their potential fixed.
Using the recursive reasoning, the charge perturbations on each pore $\{\delta q_1, \ldots, \delta q_N\}$ are linearly linked to the bare charge of the pores $\{q_1, \ldots, q_N\}$

$$\delta\vec{q} = \left(-\frac{a}{L}\right) \times \boldsymbol{A} \cdot \vec{q}. \tag{2.17}$$

The matrix is a function of the geometry of the pore network. For example for N pores in a line separated by a distance L, the matrix has the structure

$$A_{ij} = \begin{cases} 0 & i = j, \\ |i-j|^{-1} & i \neq j = 1 \ldots N. \end{cases} \tag{2.18}$$

The transformation matrix is always centrosymmetric in any geometry, because $A_{ij} = A_{ji}$, and in a linear geometry is also a Toeplitz matrix, which can be diagonalized numerically using fast recursive algorithms.
Now the capacitance $C_{\rm N\ pores}$ follows. To first order in a/L, each pore entrance carries a total charge $Q_i \simeq q_i + \delta q_i = q_i + (-a/L)A_{ij}q_j$. At the zeroth order, the charges q_i are fixed by the potential V_0, as

$q_i = q_0 = 4\epsilon a V_0 \, \forall i$, and the total charge in a N-pores array is

$$\begin{aligned} Q_{\text{N pores}} &\simeq \sum_i q_i - \frac{a}{L} \times \sum_i \sum_j A_{ij} q_j \\ &= 4\, N \epsilon a V_0 \left(1 - \frac{a}{L} \times \frac{1}{N} \sum_{i,j} A_{ij} \right). \end{aligned} \tag{2.19}$$

Thus we get

$$C_{\text{N pores}} \simeq N C_{\text{single pore}} \times \left(1 - \frac{\gamma_N a}{L} \right) \tag{2.20}$$

with $\gamma_N \equiv N^{-1} \sum_i \sum_j A_{ij}$ a global factor accounting for the geometry of the network.
We finally obtain for the effective electric size of the pores: $a_{\text{eff}} \simeq a \left(1 - \gamma_N \frac{a}{L}\right)$. The previous expression for a_{eff} can be viewed as the first order expansion of the (physically more relevant) formula

$$a_{\text{eff}} \simeq \frac{a}{1 + \gamma_N \frac{a}{L}}. \tag{2.21}$$

While this form involves a number of approximations, we anticipate from the numerical results below that this is found to agree very well with the numerical solution. Together with Eq.(2.15), this expression gives the conductance of the N-pores network.

2.2.3 Scaling relationships

While exact values for the geometric factor γ_N can be explicitly calculated for specific geometries, it is possible to obtain scaling relationships in the limit of a large pore array, $N \to \infty$. We consider specifically two geometries: a line of pores and 2D compact arrays, for example made of square or hexagonal lattice of N pores.

The case of lines is certainly the simplest one. The corresponding transformation matrix $\boldsymbol{A}$ is given in Eq.(2.18) and $\gamma_N = \frac{1}{N}\sum_i \sum_{j\neq i} |i-j|^{-1}$. For large N a continuum approximation can be made and

$$\gamma_N = \frac{1}{N}\sum_i \sum_{j\neq i} \frac{1}{|i-j|} \simeq \frac{1}{N}\int\int_{|x-y|>1}^{N} dx\, dy\, \frac{1}{|x-y|} \tag{2.22}$$

yielding

$$\gamma_N \approx \log N \tag{2.23}$$

for the 1D line of pores.

In the case of a 2D compact lattice of N pores, the transformation matrix $\boldsymbol{A}$ takes the generic form

$$A_{ij} = \begin{cases} 0 & i = j, \\ |r_i - r_j|^{-1} & i \neq j = 1 \ldots N. \end{cases} \tag{2.24}$$

with r_i the (dimensionless) positions of the pores in units of L, and

$$\gamma_N = \frac{1}{N}\sum_i \sum_{j\neq i} \frac{1}{|r_i - r_j|} \tag{2.25}$$

To estimate the sum in Eq.(2.25), we proceed using an analogy to a further electrostatic problem. The sum corresponds indeed to the electrostatic energy $\mathcal{E}_N$ of a conductor made of the N pores with unit charge. In the large N limit, a continuum approximation can be made, so that $\mathcal{E}_N = \frac{\mathcal{Q}_N^2}{2\mathcal{C}_N}$, with $\mathcal{Q}_N = N$ the total charge, and $\mathcal{C}_N$ the capacitance of the global object (here the N pores). Using standard results [55], C_N scales linearly with the lateral size $\mathcal{R}_N$ of the compact N pores system, so that $C_N \sim \mathcal{R}_N \sim \sqrt{N}$.

Gathering results, one gets finally

$$\gamma_N \sim N^{1/2} \tag{2.26}$$

for 2D arrays of pores. The scaling is therefore stronger in 2D as compared to the logarithmic scaling for the 1D line. This is due to the higher coordination number in 2D.

2.2.4 N-pore conductance

Altogether one therefore predicts for the conductance the following expression

$$G_N \simeq N\kappa_\mathrm{b}\left[\frac{l}{\pi a^2}+\frac{1}{2a}\left(1+\gamma_N\frac{a}{L}\right)\right]^{-1} \tag{2.27}$$

with $\gamma_N \sim \log N$ for lines of pores, while $\gamma_N \sim N^{1/2}$ for 2D arrays of pores. A counter-intuitive outcome of this prediction is that – *whatever the bulk contribution to the conductance*, as described by the first term in the brackets in the right hand side of the previous equation –, the contribution of entrance effects dominates for sufficiently large N and

$$\frac{G_N}{N} \propto \frac{1}{\gamma_N} \xrightarrow[N\to\infty]{} 0 \tag{2.28}$$

Entrance effects lead to a sublinear scaling of the conductance as a function of the number of pores and the conductance per unit pore vanishes for an infinite number of pores.

We shall come back on the astonishing consequences of this prediction in section 2.5.

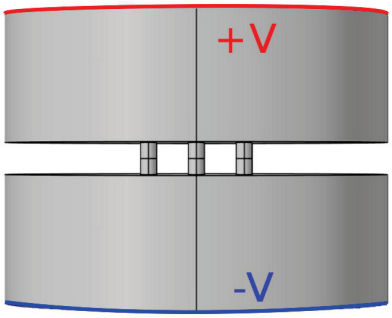

FIGURE 2.3: Axisymetric geometry of 3 pores in a membrane used for the resolution of the Laplace equation. Courtesy of S. Gravelle.

2.3 Numerical validation of the scaling relationships

Before turning to the experimental investigation of this unexpected effect, we first validate our predictions on the basis of a numerical resolution of the transport equations using a finite-element method (COMSOL software). This allows merely to apprehend the approximations behind the above calculation.

We built up an axisymetric system formed by two reservoirs separated by a thin non-conducting membrane with one or N pores drilled through the membrane. We ensured that the size of reservoirs was much larger than the pore radius and the global pore network to avoid finite-size effects, see Fig. 2.3. We imposed an electrical potential difference ΔV between the two sides of the membrane. Then we solved the Laplace equation for the potential V, $\vec{\nabla}^2 V = 0$, using a finite-element calculation.

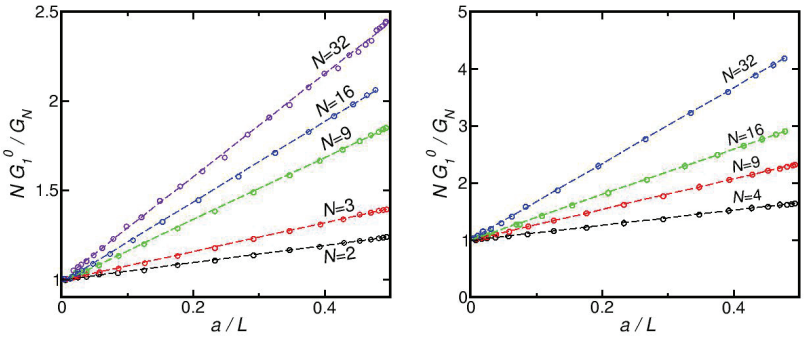

FIGURE 2.4: Numerical results: inverse conductance for N pores, G_N, normalized by $N \times G_1$, with G_1 the conductance of a single pore, versus the inverse distance L between the pores for various numbers N of pores: (*Left*) N pores in a line; (*Right*) N pores in a square array. The linear dependence does confirm the prediction in Eq.(2.27). The slope of the linear dependence allows to extract the geometric factor γ_N.

The boundary condition at the interface between the membrane and the solution is that of a vanishing flux, leading to $\vec{n} \cdot \overrightarrow{\nabla} V = 0$ on the surfaces. Finally we measured the total ionic current I through the pores, defined according to the mesoscopic Ohm's law as

$$I = \kappa_{\rm b} \int_S (-\overrightarrow{\nabla} V) \cdot \overrightarrow{dS} \tag{2.29}$$

being $\kappa_{\rm b}$ the bulk conductivity and S a cross-section of the system.

Within this numerical setup, we explored both the linear and 2D networks (square and hexagonal lattice) for a number of pores varying from $N = 2$ up to $N = 151$ (for the hexagonal arrangement). In Fig.2.4, we show the conductance across the nanopore network, calculated numerically for a varying distance L between pores. For the various geometries, we found that the inverse conductance scales linearly with the inverse length L^{-1}, in full agreement with our main prediction in Eq.(2.27).

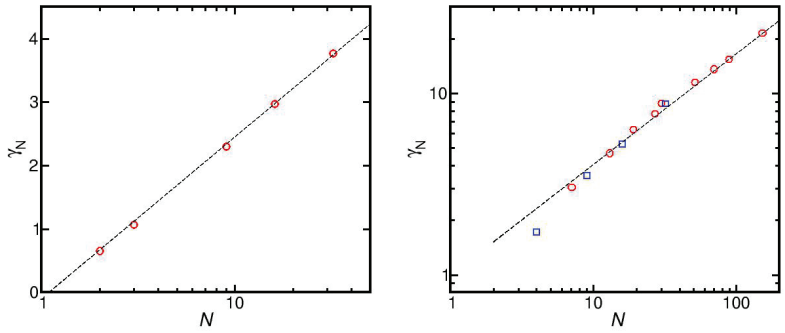

FIGURE 2.5: Numerical results: Plot of the geometrical factor γ_N versus the number of pores N. (*Left*) N pores in a line: the linear fit shows that $\gamma_N \sim \log N$ in this geometry. (*Right*) N pores in a square array (square symbols) and in an hexagonal array (circle symbols). The dashed line is a powerlaw fit with a 0.6 exponent.

Indeed, from Eq.(2.5) and Eq.(2.27), one expects

$$\frac{NG_1^0}{G_N} = \frac{\dfrac{\ell}{\pi a^2} + \dfrac{1}{2a}\left(1 + \gamma_N \dfrac{a}{L}\right)}{\dfrac{\ell}{\pi a^2} + \dfrac{1}{2a}} = 1 + \frac{a}{L}\frac{\gamma_N}{1 + \dfrac{2\ell}{\pi a}}. \tag{2.30}$$

The linear dependencies of the inverse conductance with a/L thereby confirms our predictions. From the reservoir, the effective electrostatic diameter of the pore, given in Eq.(2.21), is the size that matters.

From the slope of the lines in the previous plot, one can accordingly extract the geometric factor γ_N. This is plotted in Fig. 2.5 for the line of pores, as well as for the square and hexagonal network of pores.

Altogether these numerical calculations fully confirm the predictions of the scaling analysis. The geometric factor is found to scale logarithmically in N for the linear network, $\gamma_N \sim \log N$, while it scales algebraically with the number of pores in the 2D system, $\gamma_N \sim N^\alpha$, with a measured exponent $\alpha \simeq 0.6$ very close to the predicted one (0.5).

We attribute the slight difference in exponent in edge effects which should disappear in the very high N regime (which we could not reach numerically).

We now turn to the experimental counterpart with the aim to explore the electric conductance across an array of nanopores.

2.4 Experimental results on linear and square arrays of pores

Experimental measurements were conducted on nanopores. We first describe the fabrication process of the nanopores, and the preparation protocol. Then, we relate how the operations are done before presenting the results for linear and square arrangements of pores.

2.4.1 Fabrication process and setting up of the measurement device

We fabricated multipore membranes from commercial 7.5 mm x 7.5 mm x 380 μm silicon chips, covered with a 50-nm silicon-nitride (Si_3N_4) layer (*Silson*). A 50 μm square is etched at the center of the chip, to leave access to the 50-nm thick Si_3N_4 layer.

The nanometric silicon nitride membrane was drilled by gallium Focused Ion Beam (FIB) milling. The resulting nanopores were cylindrical, of radius $a \approx 100$ nm. Various FIB scan protocols were tested by R. Fulcrand in order to obtain straight cylinders [63]. Cross-section images, obtained with a scanning electron microscope (SEM), are displayed on Fig. 2.6. These five cylinders were milled using the four available scan

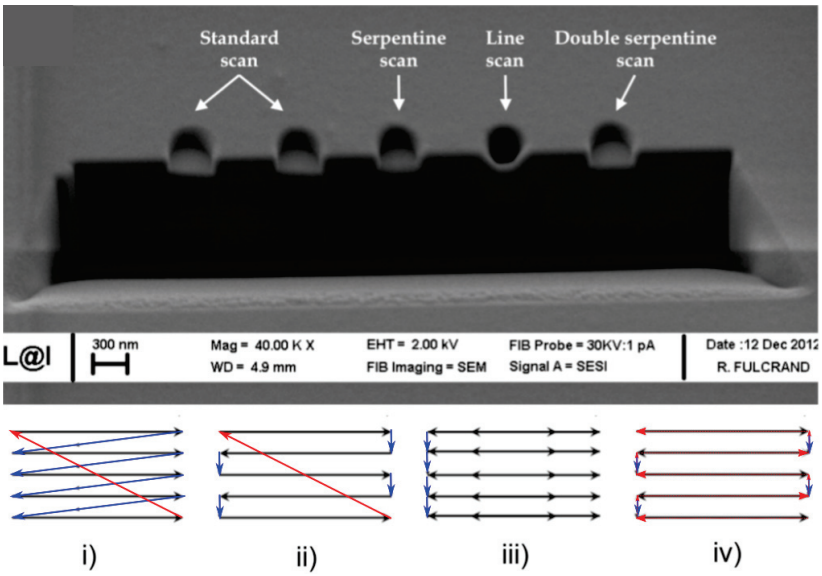

FIGURE 2.6: Effect of various FIB scan protocols on pore milling in SiN thick membrane (1 μm) at 1 pA by using the same ion dose (1 nC/μm^2). Below, different protocols are illustrated: (i) standard raster scan, (ii) serpentine scan, (iii) line scan and (iv) double serpentine scan. The beam follows the black and blue lines first, then the red lines on its way back. Courtesy of R. Fulcrand.

methods of the ion beam on the FIB/SEM used for this work. The figure demonstrates how the scan method can alter the shape of the cylinder, even if the same dwell time, probe current and ion dose were used. The standard scan results in a non-planar floor as the beam always scans in the same direction (left to right in Fig.(4)-a). The serpentine scan gives a level floor but results in an increased redeposition on the sidewalls, resulting in a more conical shape. This effect is further enhanced for the line scan method whereas the double serpentine scan gives the best results for this particular material system leading to no significant "hourglass" shaping of the pores.

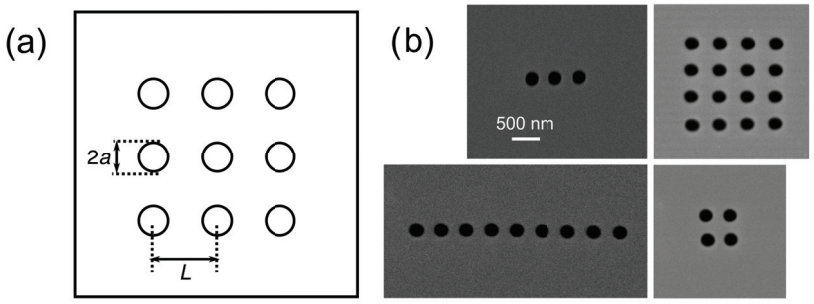

FIGURE 2.7: (a) Sketch of the system. (b) SEM images of FIB-milled multipores: pore lines and square arrays.

Using this technique, we fabricated membranes with 1 to 90 drilled nanopores on a line or in square array, with various distances L between the pores. The actual distances and diameters were measured post-fabrication by SEM imaging, with errors of a few nanometers . Figure 2.7-b shows the SEM image of a sample with various nanopore arrays.

Each chip was then inserted in a custom-made electrochemical cell in polyether ether ketone (PEEK). This polymer is renowned for its robustness, either under mechanical stress or chemical attacks from both organic and aqueous environments. The risk of pollution and clogging of the nanopores was thus reduced.

The cell consists in two reservoirs between which the chip is sandwiched, the sealing being insured by O-rings. The set up is represented in Fig. 2.8. The plugs which close the reservoirs have little holes where a 0.8 mm silver wire is inserted. These wires become Ag/AgCl electrodes after plunging them in bleach (NaClO solution) for 30 minutes. Such activation was performed about once a week.

Before any chip insertion, both reservoirs as well as the O-rings were ultrasonically cleaned with deionized water (18.2 MΩ.cm, *Millipore*)

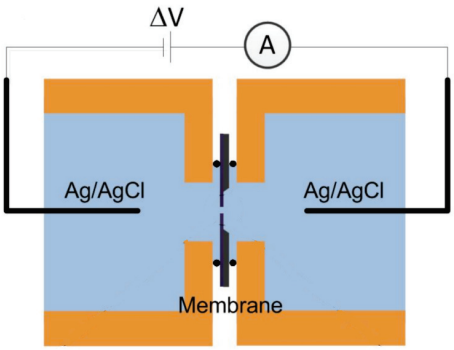

FIGURE 2.8: Schematic of the electrochemical cell, from [12]. The parts in PEEK are represented in orange. The tension generator is a data acquisition system (DAQ) in output mode. The ammeter symbol stands for the I/V converter, of which the voltage is recorded through the DAQ.

and soap (MicroSon, *Fisher Scientific*) for 15 minutes at 60°C. Several rinses were then completed. The purpose of the procedure is to remove any trace of salt or dust in the cell. The O-rings and the chip had to be carefully manipulated with Teflon nip, to avoid any scratch which could entail a leakage.

After the insertion of the chip in the cell, both reservoirs were filled with a previously degassed KCl solution of concentration c_s ranging from 10^{-4} mol/L to 1 mol/L, made by diluting solid KCl (*Acros Organics*, 99% purity) into deionized water. The conductivity of the solution was checked before each experiment with a conductimeter (HI 2550, *Hanna Instruments*). Salt concentration was computed from the measured conductivity considering an average temperature of 22°C in the room [64].

At this point, the measurement device is ready to fulfill its role. We now expose the electric measurement procedure.

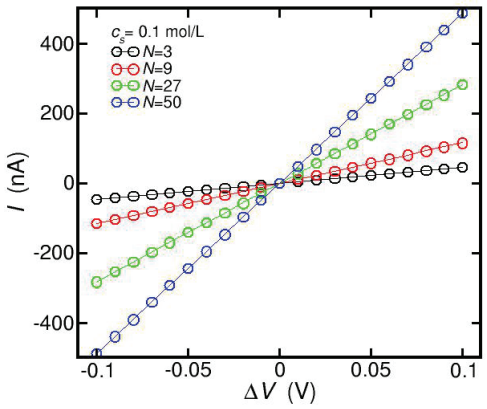

FIGURE 2.9: Typical current-voltage curves in N nanopores, obtained in KCl solutions at $c_S = 0.1$ mol/L.

2.4.2 Electric measurements

Figure 2.8 contains a schematic of the electrical circuit. Voltage is imposed on the electrodes via a National Instruments data acquisition system board. Note that the silver chloride electrodes used here allow fast electrode kinetics: the chemical reactions taking place at the electrodes

$$\mathrm{AgCl_{(s)} + e^- \rightleftharpoons Ag_{(s)} + Cl^-}$$

have a 100% efficiency up to at least several mA of current in our device. As one of the electrodes is connected in series to a custom-made I/V converter, the current was also recorded thanks to the acquisition card, see Fig. 2.8. The conductance of the nanopores is then extracted from I-V characteristic curves such as the ones displayed on Fig. 2.9. The whole procedure is monitored through a *LabVIEW* program. The resolution with this setup is $\pm$ 1 pA.

The first KCl solution used was a 1 mol/L, then we carefully emptied, rinsed, and refilled the cell reservoirs with solutions progressively less concentrated. From the lower salt concentration, we followed a regular increase of concentration until 1 mol/L. Figure 2.10-a is a plot of the measured conductance as a function of the salt concentration for a single nanopore. Below $c_S \sim 10^{-2}$ mol/L, a slight deviation from the linear behavior can be noted, in agreement with previously reported observations (see section 2.1.2).
This saturation is the signature of surface conduction, which takes precedence over bulk conduction for the Dukhin length overpassing the pore size. From Fig. 2.10-a, we can estimate the surface conductivity of a nanopore as $\kappa_S = 0.4$ nS, corresponding to a surface charge $\Sigma = 6$ mC/m^2. These values are in agreement with previous measurements in [12] on similar nanopores. For a salt concentration $c_S = 10^{-3}$ mol/L, the Dukhin length is worth $l_{Du} = \kappa_s/\kappa_b \sim 40$ nm which compares to the nanopore radius $a = 100$ nm. This indicates that the typically nanometric behavior of surface conduction predominance is at stake indeed.

In the study of electrostatic interactions between pores that we want to fulfill, we chose to stay in the classic regime of bulk conduction dominating over surface conduction. In this purpose, we used solutions from 1 to 10^{-2} mol/L. In this range of concentration, the simple formula (2.5) is sufficient to account for the measured conductance of a single pore. We now turn the experimental results on lines of 3 nanopores, with various spacings.

2.4.3 3 pores in a line: scope of the interaction

In this section, we explore the case of three pores in a line, which we compare to the measurements obtained for a single-pore membrane.

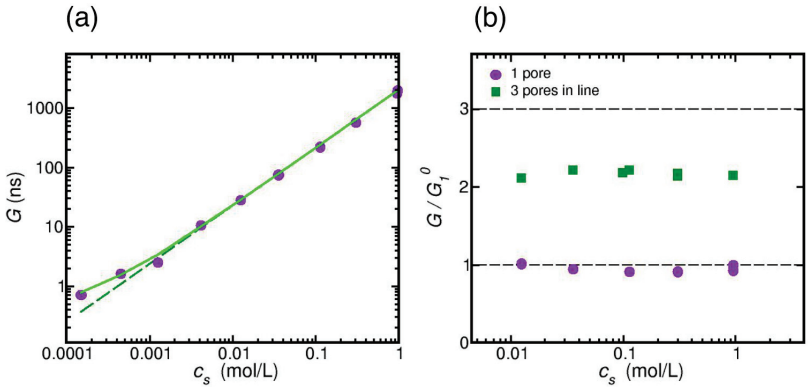

FIGURE 2.10: (a) Experimental conductance of a single nanopore, as a function of salt concentration (purple circles). The dotted line is Eq.(2.5) prediction, from which experimental measurements depart at low concentration. The green curve is the prediction of Eq.(2.10) using $\kappa_s = 0.4$ nS. (b) normalized conductance of 1 pore (purple circles) and 3 pores in line (green squares), spaced with $L = 4a$. The naively expected values of 1 and 3 are evidenced with dotted lines.

The 3-pore conductance was normalized by the single pore value, G_3/G_1^0, using Eq.(2.5) and the measured conductivity of the solution. On Fig. 2.10-b, the normalized conductance of 3 pores spaced with $L = 4a$ is clearly lower than the naively expected value of 3. This gives an indicator of the strength and scope of long-range interaction between pores. Note that there is no dependence of the normalized conductance with salt concentration in this regime, as expected.

To confirm this trend and rationalize the role of pore spacing, we report in Fig. 2.11 the conductance of five different 3-pore systems G_3, as a function of the distance L between the pores. This time, the conductance was normalized by three times its single pore value, $G_3/3G_1^0$. As the normalized conductance approaches unity when $L \gg a$,

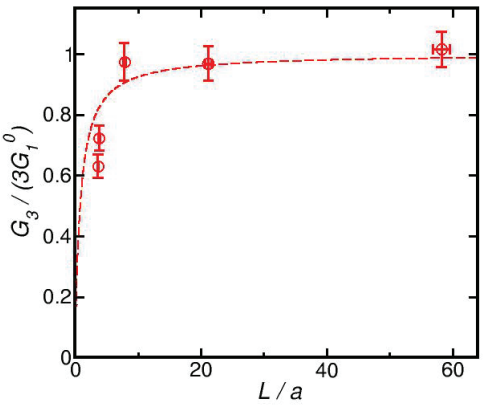

FIGURE 2.11: Experimental values of the normalized conductance $G_3/3G_1^0$ of 3-nanopore linear arrays, with G_3 measured conductance of the sample and G_1^0 the predicted conductance of a single nanopore, as a function of the normalized distance L/a. The pore radius is $a = 100$ nm. Error bars are obtained from measurements over 5 salt concentrations in the range $10^{-2} - 1$ mol/L (standard deviation of G_3/κ_b) and an uncertainty of 10 nm on the distances L and radii a. The dashed line is the prediction using Eq.(2.27) (with $\gamma_3 = 1.07$ as obtained from the numerical calculation).

a strong decrease of the multipore conductance, with respect to the sum of the contributions of individual pores, is observed at small interpore distance $L \approx a$, so that $G_3 < 3 \times G_1^0$.

Furthermore the theoretical prediction in Eq.(2.27) is found the reproduce fairly well the experimental results (with $\gamma_3 = 1.07$ as obtained from the numerical calculation). We now turn to experiments on membranes where the interpore spacing is fixed: $L/a = 4$.

2.4.4 Multipore networks: linear and square geometries

While the above experiment confirms the strong mutual influence of the nanopores, we now come to our main focus: the dependency of the conductance with the number of pores N. To this end we have measured the conductance in linear and square arrays of nanopores, with a number of pores varying between $N = 1$ to $N \approx 50$ for a given interpore distance L ($L \approx 4\ a$). The results are displayed on Fig. 2.12. The conductance of the multipore system G_N, normalized by N times the expected contribution of an individual pore, is plotted versus the number of pores N. The panels (a)–(b) of this figure clearly demonstrate that the normalized conductance *decreases* by a large factor with the number of pores N.

As suggested by our prediction in Eq.(2.27), these data are presented in the panels (a′)–(b′) as NG_1/G_N versus N to highlight the scaling behavior of the entrance effects. The results for the line of nanopores, panel (a′), do exhibit a $\log N$ scaling, in full agreement with our predictions above. The 2D square array exhibits a slow algebraic increase of the entrance effects, as highlighted by the comparison to a $N^{1/2}$ scaling in panel (b′), again in agreement with our predictions. Altogether the experiments fully confirm the sublinear scaling of the conductance due to entrance effects. They highlight the mutual interaction of electric transport between the pores, as shown in the deformation of the electric streamlines, see Fig. 2.1-b.

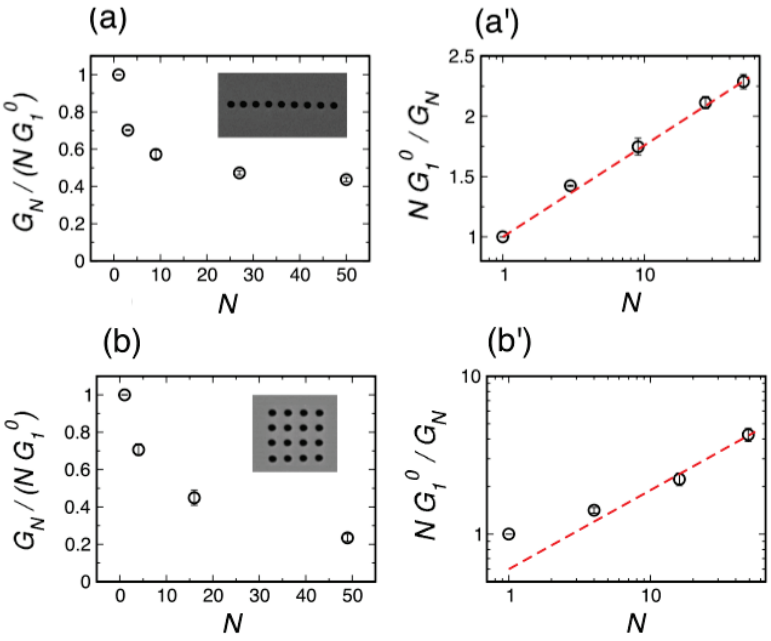

FIGURE 2.12: Experimental results: conductance across N nanopores f(a) and in a square array (b), as a function of the number of nanopores N. The conductance is normalized by N times the value expected for a single isolated nanopore. The distance between nanopores is fixed $L \approx 4\ a$ (with $a \approx 100$ nm the pore radius). In panels (a′) and (b′), the inverse conductance is plotted versus the number of pores in order to highlight the scaling with N. The dashed line highlights the predicted $\log N$ behavior for the linear geometry (panel a′), while it shows a $N^{1/2}$ scaling for the square geometry (panel b′). This plot gathers measurements for salt concentration c_s between $10^{-2} - 10^{0}$M, as the normalized conductance is independent of concentration in this regime.

2.5 Discussion

In conclusion, we experimentally demonstrated and theoretically justified that the conductance through arrays of nanopores exhibits an anomalous subadditive dependence of the conductance on the number of pores. The total ion conductance normalized by the sum of individual contributions *strongly decreases* with the number of pores N. A theoretical framework shows that this counter-intuitive behavior originates in the mutual interactions between the nanopores. The long range nature of the transport leads to a bending of the field lines at pore entrances, thereby modifying the apparent cross-section of each pore.

We furthermore proposed a scaling approach showing that the global entrance effects diverge as N goes to infinity. This leads to a sublinear dependence of the total conductance versus the number of pores, scaling as $G_N \sim N/\log(N)$ for an array of N pores in a line, and $G_N \sim N^{1/2}$ for a 2D array of pores. An astonishing consequence is that the normalized conductance G_N/N *vanishes* for an infinite number of pores, $G_N/N \to 0$ as $N \to \infty$. We checked this result by finite-element simulation, finding a good agreement with experimental results.

We quote that our results are valid in the regime where surface conduction can be neglected compared to bulk conduction inside the pore. This implicitly assumes moderate to high salt concentration. It corresponds to a regime where the so-called Dukhin length l_{Du}, defined as the ratio between surface and bulk conductivity, is smaller than the interpore distance. It would be highly desirable to extend our predictions to include the effects of surface conduction.

The consequences of the sublinearity of the conductance with the number of pores are highly non-trivial. Its effects will be particularly dominant

for ultrathin membranes, such as graphene pierced by many pores. While one would naively expect that, for the molecularly thin graphene layer, a huge electric potential gradient should build up across the membrane. However, two phenomena reduce the effective potential gradient inside the molecular pore. First, even for a single pore, entrance effects imply a strong potential drop outside the pore. Indeed, the shorter the pore, the more entrance effects dominate over Poiseuille dissipation. Second, as we just showed, electrostatic interactions increase access resistance, which means that the potential drop outside the pore is even higher. Therefore, an imposed potential drop between two electrodes does *not* report itself between a pore's extremities, and the gradient inside a graphene pore is not as high as we wish. To circumvent access-related potential drop, one could imagine to graft electrodes on both sides of a graphene layer itself, but this remains an unexplored situation.

We saw that the anomalous scaling of the conductance originates from entrance effects. It is thus easily understandable that it will have consequences in transport through pores with small aspect ratio ℓ/a, where entrance effects are the main source of dissipation. Yet, this anomalous scaling can affect even longer channels, provided the number of channels is significant. Indeed, as it can be seen from our main prediction in Eq.(2.27), entrance effects always prevail over bulk conductance through the membrane for sufficiently large N. Typically this occurs – using Eq.(2.27) – when $\gamma_N \gtrsim L \cdot \ell/a^2$, with ℓ and a the length and radius of the pores, and L their interdistance. This condition occurs above a threshold number of pores, $N^\star$. For a 1D line of nanopores, $N^\star \approx \exp[L \cdot \ell/a^2]$, while $N^\star \approx \left(L \cdot \ell/a^2\right)^2$ for a 2D array. Above $N^\star$, entrance effects start to play a dominant role and the anomalous scaling for the conductance is in effect, decreasing the conductance with the number of channels N. For membranes made of channels with large aspect ratio $\ell/a \gg 1$, $N^\star$ is accordingly very large and the effect is

weak. However, for macroscopic membranes, even if the aspect ratio is large, we can foresee that this phenomenon will take place, considering the very large number of channels and the very short distance between them.

Furthermore it is also interesting to note that the theoretical framework proposed here can be generalized to other transport phenomena involving a Laplacian type of equation. This is due to the conservation equation which leads to long-range interaction between the pores. While this should deserve further systematic investigations, the present results are expected to generalize to diffusive or heat transport (provided the membrane is assumed to be thermally insulating). In the context of reverse osmosis and desalination process, an anomalous scaling with the number of channels could have a major impact on the efficiency.
As far as hydrodynamic transport is concerned, the Stokes equation also exhibits a similar Laplacian form (for the velocity potential). An analogy can be made between the pressure drop and the potential drop (the driving forces) as well as between the fluid velocity and the current (the fluxes). The concept of hydrodynamic resistance is thus familiar in students textbook. Nevertheless, Ohm's law (so as Fick's and Fourier's laws) provides a relationship of proportionality between the driving force and the flux which has no equivalent in hydrodynamic transport. Therefore the approach we developed in this chapter cannot be applied directly to hydrodynamic interactions, although they do exist and have appreciable (but weaker) effects. This will be the purpose of the second chapter of this thesis.

The case of cross-transport phenomena is also of interest and may well be affected by a similar anomalous scaling. For example, electro-osmosis, which is a solvent flow driven by the charged diffuse layer motion under an electric field, originates in the potential gradient inside the channel. If this potential gradient is reduced because of the anomalous scaling

of entrance effects, electro-osmosis is likely to be affected. Due to Onsager symmetry, the same holds for the streaming current, which is the electric current induced by hydrodynamic flow under a pressure drop. This will be tackled in the discussion of the next chapter. Note that electro-osmosis and streaming currents are generally neglected in nanopores (as in our case), but come into play for longer channels. Yet we saw that for N channels with $N > N^\star$, the anomalous scaling of entrance effects has indeed an influence, and can thus possibly lead to modifications for cross-transport phenomena.

In the context of energy harvesting, streaming currents were considered as an interesting new route to produce electric current I_{stream} from pressure gradients [65]. In the discussion of the next chapter, we will give the scalings concerning the maximum power produced and the efficiency of the energetic conversion.

Altogether, electrical entrance effects across membranes exhibit subtle and counter-intuitive features, which could have significant repercussion in various fields.

Chapter 3

Hydrodynamic interactions within pore arrays

Contents

3.1 Flows in nanochannels

The development of new nanofabrication tools has allowed the design of controlled nanostructured materials [39], and has lead to a greater understanding of such systems. The living world features many nanometric systems, for example aquaporins and ionic pumps, which have recently benefited from thorough nanofluidic investigation [66]. The nanotechnological breakthrough also permitted to unveil previously undetected behaviors, such as the great slippage experienced by water in carbon nanotubes [67–69]. Numerous applications taking advantage of nanometric good properties have been imagined, especially in the fields of water-filtration, desalination or energy conversion [29, 70, 71]. For example, in desalination by reverse osmosis, a flow of pure water is driven through subnanometric pores by an imposed pressure drop [30]. Also, streaming currents have been considered as an alternative route to produce electric energy from hydraulic energy [16]. This process uses the fact that ionic currents can be produced by an applied pressure drop, which set into motion the charged diffuse layer in the fluid, close

to a surface. Such conversion can be efficient only at the nano scale, where surface effects become of the same order of magnitude as bulk effects.

The passage from one nanochannel to a macroscopic marketable membrane is not trivial, as parallelizing thousands of nanochannels does not necessary lead to a proportional increase in the quantity desired. Thus there is a strong need for predicting tools, to achieve the scaling up towards efficient devices. In this sense, we saw in the previous chapter that long-range interactions at pore entrances lead to a sub-additive conductance of an array of nanopore. Yet energy conversion processes involve electric and fluidic transport, which may not behave alike. In this chapter, we tackle the scaling of fluidic transport, investigating the stream-flow response of parallel pores to an applied pressure drop. Recently, Stone and coworkers proposed a theoretical first order approach to account for permeability corrections arising in multipore membranes, compared to a single pore situation [72]. We follow the same aim of predictability for an efficient scaling-up of nanofluidic properties, and present here an experimental approach leading to more complete rules concerning pore size and arrangement.

To avoid energetic loss and maximize pressure or potential gradients, the thickness of nanoporous membranes is reduced at its maximum. The use of graphen is even envisioned [32]. The hydrodynamic permeability of such systems is therefore mainly governed by entrance effects [4], which will be presented in the present section after a brief history of physics of fluid flows. One objective of this study is to understand how hydrodynamic entrance effects – and thus the global permeability – are affected by hydrodynamic interactions at pore entrances. We will present existing results on this subject, before turning to our choice to perform macroscopic experiments of water drainage which will be justified. This first section will end by the remark that macroscopic drainings can

reach regimes where the flow departs from a purely creeping behavior. Such small inertial effects could take place in the first stages of water filtration, with pore sizes of the order of 0.1 mm. We pursue the study of hydrodynamic interactions in this regime.

3.1.1 A bit of History

Fluid mechanics is built on many contributions from different ages. The oldest ones date from Greek Antiquity, when Archimedes (c. 287 BC – c. 212 BC) established that the upward buoyant force exerted on an immersed body is equal to the weight of the displaced fluid [73]. After many centuries of interruption (at least, in Christian Europe), the study of fluids resumes at the Renaissance with Leonardo da Vinci (1452-1519). He described various types of flows (jets, swirls, surface waves) and established the principle of mass conservation, following Empedocles and Epicurus ideas.

The mathematisation of hydrodynamics follows closely the development of mechanics initiated by Galileo and Newton. Bernouilli studied on perfect (*i.e.* non viscous) fluids, preceding d'Alembert and Euler who set the basis of fluid dynamics. D'Alembert notably introduced the notions of velocity field and partial derivative [74]. Having read d'Alembert's work, in 1755 Euler established the partial derivative equations describing incompressible perfect fluids [75]. However, a body immersed in such a perfect fluid would be affected by no resistance, which clearly is not the case in usual fluids. This is known as the d'Alembert paradox, and was solved by the addition of a viscous term in Euler equations, by Navier in 1820 [76] followed by Stokes in 1845 [77]. The Navier-Stokes equations, describing newtonian fluids in incompressible flow, read

$$\mu\left(\frac{\partial\vec{v}}{\partial t}+(\vec{v}\cdot\overrightarrow{\nabla})\vec{v}\right)=-\nabla p+\eta\triangle\vec{v},\quad\overrightarrow{\nabla}\cdot\vec{v}=0. \tag{3.1}$$

with μ the fluid density, p the pressure field and η the fluid dynamic viscosity. The first equation expresses the conservation of momentum, while the second one (also called continuity equation) characterizes an incompressible flow, which means that its density stays constant during the movement. The viscous term $\eta \triangle \vec{v}$ is a macroscopic formulation of the molecular level friction between fluid particles, and between particles and the fluid boundaries.

We consider here stationary flow, hence $\dfrac{\partial \vec{v}}{\partial t} = 0$. In nanofluidics, inertial effects are overwhelmed by viscous forces. This is quantified by the Reynolds number $\mathcal{R}_e$, which we define as

$$\mathcal{R}_e = \frac{\mu L v}{\eta} \sim \frac{||(\vec{v} \cdot \nabla)\vec{v}||}{||\eta \triangle \vec{v}||} \ll 1 \tag{3.2}$$

where L is a characteristic length scale of the flow, usually the channel radius a. This scaling comes from the low values of the system size and flow velocity. In this case, the first Navier-Stokes equation can be simplified to the Stokes equation

$$\overrightarrow{0} = -\overrightarrow{\nabla} P + \eta \triangle \vec{v}. \tag{3.3}$$

The most famous use of the Stokes equation is the Hagen-Poiseuille flow, describing a pressure-driven uniaxial flow in a cylindrical pipe. With the assumption of no slip boundary conditions (*i.e.* at the fluid/solid interface $v(r = a) = 0$), the velocity profile for such a flow can be easily inferred from the Stokes equation: $v(r) = \dfrac{-\Delta P}{4\eta\ell}(a^2 - r^2)$. $\Delta P = P(z = \ell) - P(z = 0)$ is the pressure drop between the pipe ends, ℓ the pipe length, a the pipe radius and r the radial coordinate (see Fig. 3.1-a). We now come to the concept of hydrodynamic resistance R (same notation than the electric resistance), which is central in this thesis. The hydrodynamic resistance R is defined as the absolute value

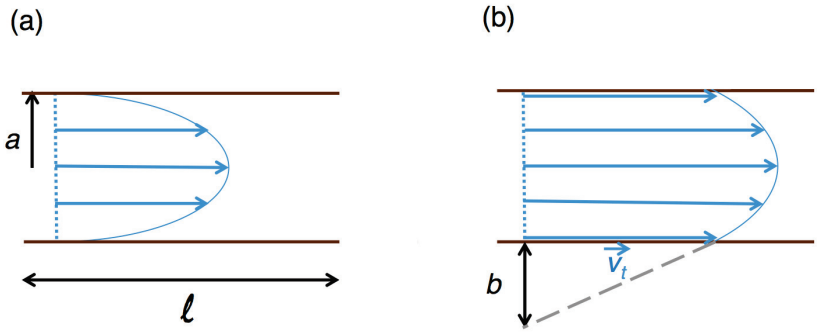

FIGURE 3.1: (a) Velocity profile of a Hagen-Poiseuille flow with no-slip boundary conditions. (b) Idem with slippage at the fluid-wall interface. b is the slip length, defined as $b = v_t / \left| \left(\frac{\partial v}{\partial r} \right)_{r=a} \right|$.

of the ratio of the pressure drop ΔP to the flow $Q = \iint \vec{v} \cdot \overrightarrow{\mathrm{d}S}$. In the case of a Hagen-Poiseuille flow, R can be expressed as

$$R = \left| \frac{\Delta P}{Q} \right| = \frac{8\eta\ell}{\pi a^4}. \tag{3.4}$$

Poiseuille flows are used to model flows inside nanochannels or nanopores, but it is in fact valid for a wide range of Reynolds numbers. The hydrodynamic resistance of a cylindrical flow can be described by Poiseuille resistance for $\mathcal{R}_e \ll 10^3$, which will be true in all this chapter.

In the systems we consider, Poiseuille resistance is not the only cause of dissipation in the fluid. Another cause of contribution comes from the convergence of the flow towards pores entrances, and its divergence after its passage inside the pores. These contributions are called entrance effects and are presented in the next section.

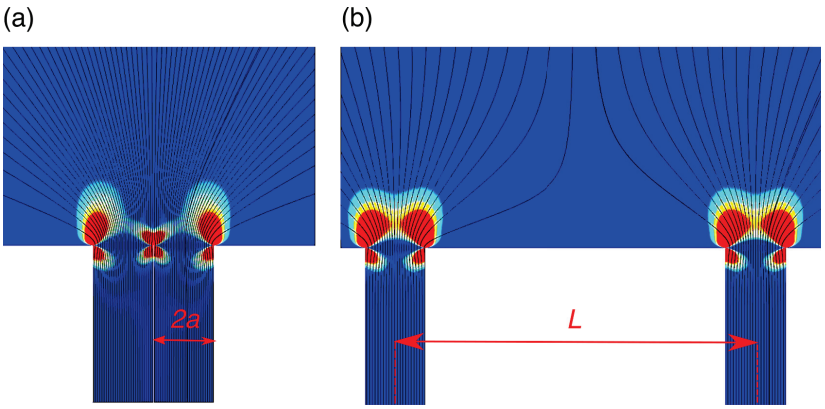

FIGURE 3.2: Snapshots of finite-element simulations of a bidimensional viscous flows converging toward two slits. The boundary condition is a perfect slip at the walls, which insures no Poiseuille dissipation. Streamlines are represented by black lines. The dissipated power density field is mapped with colors, ranging from low dissipation (blue) to high dissipation (red). The dissipated power density was computed with formula from [78]. (a) The inter-slit distance L is close to the slit width $2a$. (b) The slits are spaced with several times their width. Image courtesy of S. Gravelle.

3.1.2 Hydrodynamic entrance effects

As can be seen in Fig. 3.2, viscous flows dissipate energy when streamlines change in direction. This is the case when a fluid flows from a wide reservoir into a narrower one, as streamlines converge to enter the narrow part, and then diverge when returning in a larger reservoir. To these so-called **entrance effects** is associated an **access resistance** accounting for the energy dissipation. The sharper this change in direction is, the more energy dissipation occurs. This acknowledgment led Gravelle *et al.* to the conclusion that the hourglass shape of nanopores allowed a minimized access resistance compared to cylindrical pores [79]. This is true even down to single file transport, where continuum hydrodynamics is expected to fail [8, 79].

The first study of the resistance associated with the presence of an aperture dates back to 1890, conducted by Couette [80]. One year later, Sampson established the exact solution of a viscous flow through an infinitely thin circular aperture in an infinite plane [4]. The access resistance R^0_{acc} (the superscript ^{0} means that this value is for an isolated pore) is expressed as

$$R^0_{\text{acc}} = 2 \times \frac{3\eta}{2a^3} = \frac{3\eta}{a^3}, \tag{3.5}$$

where the factor 2 accounts for both accesses: the entrance and exit of the pore. In 1962, Weissberg proved the superposition of access and Poiseuille resistances to be a very good estimate of the total hydrodynamic resistance exerted on a fluid, flowing through an aperture in a membrane of finite width [81]. Confirmed by Dagan *et al.*, the Weissberg-Sampson-Poiseuille approximation departs by less than 1% from the exact resistance [82]. In the following, Poiseuille resistance will be written R_{in}, the subscript $_{\text{in}}$ referring to the inner part of the cylinder causing the dissipation. The global hydrodynamic resistance will be written R. Its inverse, called the permeability, will be K: $K = 1/R$. According to the Weissberg-Sampson-Poiseuille approximation, the hydrodynamic resistance R^0_1 (the subscript denotes the number of pores) of one circular pore thus writes

$$R^0_1 = \frac{3\eta}{a^3} + \frac{8\eta\ell}{\pi a^4}, \tag{3.6}$$

as if Sampson resistance and Poiseuille resistance were in series.
Entrance effects are very important in nanofluidics, especially in filtration or energy-conversion devices where the length of fluidic channels tends to be reduced. For example, in forward-osmosis, consisting in diluting a brine, the osmotic pressure that drives the flow is proportional to the concentration gradient of chemical species to be diluted. The

narrower the channels in the semi-permeable membrane, the higher the concentration gradients, which optimizes the dilution process. When the lateral dimension a of the channel is equivalent to or smaller than its length ℓ, the nanopore limit is reached. In that case, $R_{acc}/R_{in} \sim \frac{a}{\ell}$ (even in a non-cylindrical geometry), which implies that transport properties are governed by entrance effects.

In fact, entrance effects can be the main source of dissipation even in long channels, if the slippage between a fluid and its boundary is important. Indeed, in case of slippery boundary conditions, Poiseuille resistance can be greatly reduced. The boundary condition no longer writes $v(r = a) = 0$ but $v(r = a) = v_t$, which has a finite value. It was an idea of Navier to introduce the slip length b, geometrically defined in Fig. 3.1-b by

$$v_t = b \left| \left(\frac{\partial v}{\partial r} \right)_{r=a} \right|. \tag{3.7}$$

The slip length can also be interpreted in terms of liquid-solid friction at the interface [8]. The friction force F_f at the liquid-solid interface is linked to the slip velocity v_t according to

$$F_f = -\mathcal{A} f v_t \tag{3.8}$$

with $\mathcal{A}$ the lateral area and f the solid-liquid friction coefficient. By definition, the slip length is $b = \eta/f$, with η the bulk viscosity. Large slip lengths are associated with low liquid–solid friction. Slip length of the order of 10-100 nm are typically measured on hydrophobic surfaces [1, 83]. The Poiseuille resistance becomes, in the presence of fluid-wall slippage,

$$R_{\text{in}} = \frac{8\eta\ell}{\pi a^4} \left(1 + \frac{8b}{a} \right)^{-1}. \tag{3.9}$$

The second term of this expression denotes a major diminution of the resistance, when the channel size a compares to the slip length. For

perfect slip, b would be infinite and Poiseuille resistance $R_{in} \longrightarrow 0$. One of the most striking example of the reduction of Poiseuille resistance thanks to slippage, is flows in carbon nanotubes. Majumder *et al.* [67] and Holt *et al.* [68] were the first to publish experimental results of flows through carbon nanotube membranes. They reported greatly enhanced flows compared to classical predictions. In terms of slippage, it would correspond to slip length close to 1 micron. These results are not well understood, as molecular dynamics simulations predict 1 to 2 orders of magnitude lower permeabilities in similar systems [84–86]. Moreover, Sisan and Lichter showed that some of the experimental permeabilities reported by Holt *et al.* and Majumder *et al.* were even higher than what entrance effects allows, thus unphysical [87]. Indeed, even in case of infinitely long channels with great fluid/wall slippage, Poiseuille resistance may be vanishing but flow rates are still limited by entrance effects [88].

We now focus on corrections to entrance effects, due to hydrodynamic interactions at pore entrances. In the next paragraphs, we present a quick review of previous work on hydrodynamic interactions.

3.1.3 Influence of hydrodynamic interactions

Industrial applications such as water-filtration, desalination or energy conversion always involve membranes with a great number of pores or channels. We now address the prediction of the flow through such membranes, as the extrapolation from a single pore to a macroscopic membrane is not trivial. Naively, one would expect that the total hydrodynamic permeability of N pores K_N increases linearly with N. Yet we saw in the previous chapter that the electrical conductance exhibited a complex scaling with N, from which the hydrodynamic permeability cannot be deduced. For now, we present the physical

phenomenon occurring when pores are brought closer, and theoretical calculations from the literature.

We first note that Poiseuille flows inside of parallel pores are independent. If there were no entrance effects, Poiseuille resistances of neighboring pores could be simply added in parallel. But as can be seen in Fig. 3.2 page 65, when 2 parallel 2D slits are very close from each other, the access dissipation is reduced compared to when they are far apart. This would also hold for 3D cylindrical pores. "Very close" means that the interslit (or interpore) distance L is short compared to the typical length scale of the problem, which is the slit width here (or the pore radius for cylindrical pores), as in Fig. 3.2-a. On the contrary, "far apart" means that the interslit distance is large compared to the slit width, as in Fig. 3.2-b.

Another way to express the reduction of dissipation is to say that for an applied pressure drop between two reservoirs ΔP, the flux driven through the pores will surpass the expectations based on Sampson's classical results. The flux is enhanced because the effective pressure drop between pore entrances is higher than ΔP, which can be understood with only two pores and simple arguments, inspired by Jensen *et al.* [72]. We use a point source flow as a first-order approximation of Sampson flow through a pore of zero thickness and radius a. This approximation holds far from the pore. We consider a point source flow in a half space $z > 0$, the source O being located in $z = 0$, see Fig. 3.3-a. We use spherical coordinates, with r the distance to the point source, $\theta \in [0; \pi/2]$ the polar angle (also called colatitude), and $\varphi \in [0; 2\pi]$ the azimutal angle. The velocity field is purely radial and is given by the flux conservation, $Q(r) = \iint \vec{v} \cdot \overrightarrow{dS}(r) = Q$ whatever the integration

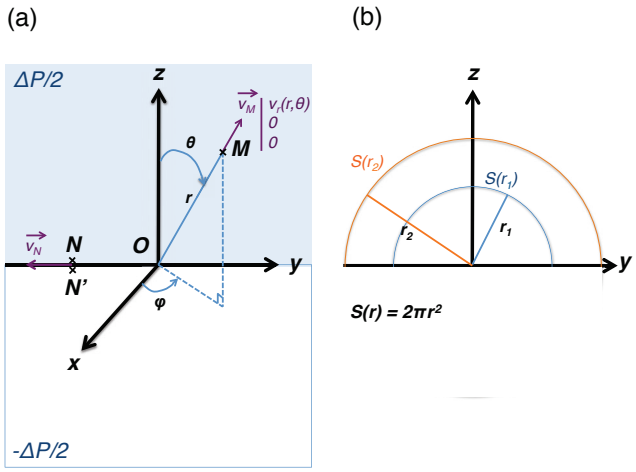

FIGURE 3.3: (a) System of coordinates used to compute the velocity and pressure fields from a point source located in O. (b) $x = 0$ plane with two examples of integration surface $S(r_1)$ and $S(r_2)$.

hemisphere $S(r)$ centered in O, see Fig. 3.3-b. One gets

$$v_r(r,\theta) = \frac{3Q}{2\pi}\frac{\cos^2\theta}{r^2}. \tag{3.10}$$

The Stokes equation then yields

$$P(r,\theta) = \frac{\eta Q}{\pi r^3}\left(3\cos^2\theta - 1\right) + P^{\infty} \tag{3.11}$$

As this expression is a first-order approximation of the Sampson's pressure field, we can use the result from Sampson's work: $P^{\infty} = \Delta P/2 = -\dfrac{3\eta Q}{2a^3}$. Note that ΔP is negative, to drive the flux toward positive z. Now, we consider a point N located in $z = 0^+$ (i.e. $\theta = \pi/2^-$) at a distance L

from the source. The pressure field in N writes

$$P(N) = P(r = L, \theta = \pi/2^-) = -\frac{\eta Q}{\pi L^3} - \frac{3\eta Q}{2a^3} \tag{3.12}$$

$$= -\frac{3\eta Q}{a^3}\left(\frac{1}{2} + \frac{1}{3\pi}\left(\frac{a}{L}\right)^3\right) \tag{3.13}$$

which is more negative that $\Delta P/2$. There is an extra depression in $z = 0^+$, caused by the presence of a pore in 0. A similar reasoning on the half-space $z < 0$ ($\theta \in [\pi/2; \pi]$) with a point sink in O and a point N' located in $z = 0^-$ (i.e. $\theta = \pi/2^+$) at the same distance L from O would lead to

$$P(N') = P(r = L, \theta = \pi/2^+) = +\frac{3\eta Q}{a^3}\left(\frac{1}{2} + \frac{1}{3\pi}\left(\frac{a}{L}\right)^3\right), \tag{3.14}$$

showing an extra pressure of the same magnitude than the depression calculated in $z = 0^+$. Finally, the pressure drop between N and N' is

$$P(N) - P(N') = -\frac{3\eta Q}{a^3}\left(1 + \frac{2}{3\pi}\left(\frac{a}{L}\right)^3\right) = \Delta P\left(1 + \frac{2}{3\pi}\left(\frac{a}{L}\right)^3\right) \tag{3.15}$$

where ΔP is the required pressure drop to let a flow Q pass through an isolated pore. Thus, if an aperture were to be drilled in N, the pressure drop would be higher than ΔP, and consequently the flux would be enhanced compared to a single pore situation.

Now, suppose we want to transport the flux Q through one pore. The required pressure drop in the presence of 2 pores $\Delta P'$ is reduced from the classical $\Delta P = 3\eta Q/a^3$ to

$$\Delta P' = \Delta P / \left(1 + \frac{2}{3\pi}\left(\frac{a}{L}\right)^3\right) \approx \Delta P\left(1 - \frac{2}{3\pi}\left(\frac{a}{L}\right)^3\right). \tag{3.16}$$

Accordingly, the access resistance of a pore within the 2-pore case $R_{\mathrm{acc},2}$ decreases compared to the single pore case:

$$R_{\mathrm{acc},2} = R^0_{\mathrm{acc}} \left(1 - \frac{2}{3\pi}\left(\frac{a}{L}\right)^3\right). \tag{3.17}$$

The influence of hydrodynamic interactions on fluid flow was first reported in 1958 by Hasimoto, who studied flows through an array of parallel slits [89]. His work was extended by Tio and Sadhal [90] and Wang [91] who considered interactions in infinite regular arrays of circular and rectangular pores. In this thesis, we rely on the theoretical results of Tio and Sadhal. They analytically solved the Stokes and continuity equations in a half-space $z > 0$, with boundary conditions reflecting the presence of apertures in the $z = 0$ plane (see Fig. 3.3 for the notations). Then, they explicitely expressed the flux rate through one aperture of zero thickness, as a power series of the ratio a/L, with a the pore radius and L the interpore distance. Each term of the series is a sum over all the other pores, as they all contribute to the enhancement of the flux. According to Tio and Sadhal's results, one can write the access resistance of a pore of radius a, labeled i, among other pores labeled j, as

$$R^i_{\mathrm{acc}} = \frac{3\eta}{a^3} \times \left\{1 - \sum_{j,j\neq i}\left[\frac{2}{3\pi}\left(\frac{a}{L_j}\right)^3 + \frac{6}{5\pi}\left(\frac{a}{L_j}\right)^5 + \frac{18}{7\pi}\left(\frac{a}{L_j}\right)^7 + \frac{56}{9\pi}\left(\frac{a}{L_j}\right)^9 + \text{h.o.t.}\right]\right\} \tag{3.18}$$

where L_j is the distance between the center of the pore considered i, and the center of the pore j, and h.o.t. stands for higher order terms. Note that our simplistic approach above gave the right first order correction, in the two-pore case.

We suppose that the pore i is at the origin O of the coordinate system. We get

$$R_{\mathrm{acc}}^{i} = R_{\mathrm{acc}}^{0}\left(1-\lambda^{i}\right) \tag{3.19}$$

with

$$\lambda^{i} = \frac{2}{3\pi}\left(\frac{a}{L}\right)^{3}\sum_{j,j\neq 0}\left(\frac{1}{|r_j|}\right)^{3} + O(\left(\frac{a}{L}\right)^{5}) \tag{3.20}$$

with r_j the dimensionless positions of the pores in units of L. $\sum_{j,j\neq 0}\left(\frac{1}{|r_j|}\right)^{3}$ always converges to a finite value, ≈ 11 for a number of pores N tending to infinity on an hexagonal array. The same applies for the higher order terms within λ^{i}. This is in strong constrast with electrostatic interactions, which are characterized by (on average for one pore)

$$R_{\mathrm{acc}} = R_{\mathrm{acc}}^{0}(1-\gamma_N\frac{a}{L}) \tag{3.21}$$

with

$$\gamma_N = \frac{1}{N}\sum_{i}\sum_{j,j\neq 0}\left(\frac{1}{|r_j - r_i|}\right) \tag{3.22}$$

which diverges with increasing N, scaling like $N^{1/2}$ for a 2D array of pores. Three consequences can be drawn from these scalings.

- First, contrary to the electrostatic interactions which reduce the ionic current, hydrodynamic interactions enhance the flow through nanopores, for a same pressure drop.
- Second, the hydrodynamic permeability of an array of pores is extensive with the number of pores, with only a positive correction. This is in strong contrast with the ionic conductance which scales sublinearly with N. Thus, while we focused on the scaling of the ionic conductance, we follow here a different approach and aim at testing the quantitative agreement between experiments and theory for the hydrodynamic permeability.

- Last, the scope and the strength of hydrodynamic interactions are much lower than those of electrostatic interactions. The $(a/L)^3$ term in λ^i is worth 0.3 for an infinite number of pores brought in contact, whereas for electrostatic interactions γ_N diverges with increasing N.

The normalized permeability of an array of pores is thus expected to increase, yet slightly, when pores are brought closer, or when pores are added.

We now come to two final remarks. First, we emphasize that using Eq. (3.18) requires to differentiate each pore access resistance R^i_{acc}. On the contrary, in Chapter 1, we bypassed such individual counting by considering global quantities on the whole array of pores (global charge and capacitance). This resulted in an access resistance averaged over all the pores. We are not aware of such a trick to compute hydrodynamic interactions, and, what is more, hydrodynamic interaction strength is much weaker than electrostatic one so hydrodynamic permeabilities are expected to vary only slightly with the different parameters. Thus, to have a chance to get quantitative agreement between experiments and theory, access resistances have to be computed precisely. We thus chose to differentiate each pore contribution and stuck to Tio and Sadhal's revisited formula (3.18).
Second, contrary to Stone and co-workers [72] who only kept the $(a/L)^3$ term in Eq. (3.18), we consider all the 4 terms calculated by Tio and Sadhal. The first alone term would have been satisfactory if it had lead to a significant variation of the access resistance, by say an order of magnitude. Such is not the case, as all terms represent corrections to the single pore case. To get a good quantitative agreement between experiments and theory, we must operate with the best precision, that is why we use the – relatively lengthy – formula (3.18).

To our knowledge, the experimental study of laminar flow in interacting pores has never been fulfilled. As we just mentioned, the increase in permeability with the number of pores is quite slight, which requires to operate with good precision. We experimentally verified formula 3.18 on gravity drainings through macroscopic perforated membranes. In the next section, we shall see why this verification also accounts for nanosystems, as the effects or hydrodynamic interactions are not size-dependent.

3.1.4 Why choosing a macroscopic scale is valid

To have a flow dominated by entrance effects, a sufficient condition is that the ratio of the pore radius to the pore width exceeds unity: $a/\ell > 1$. As for the modification of access resistance caused by hydrodynamic interactions, it is significant as soon as $a/L \sim 1$, where L is the next-neighbor distance. Thus, nothing requires nanometric pores to study hydrodynamic interactions, one should focus on the ratios above mentioned. As performing experiments at the nanoscale is still challenging, especially the measure of flux rates [1], we built a corner table experiment with millimetric pore membranes. The only thing one must beware of is the validity of Stokes equation, which depends on the value of the Reynolds number defined in Eq. (3.2). Considering the pore radius a as the characteristic length, the Reynolds number $\mathcal{R}_e$ is given by

$$\mathcal{R}_e = \frac{av}{\nu}, \tag{3.23}$$

with v the average flow velocity inside the pores and ν the kinematic viscosity of the oil. In the experiments we present in section 3.3, Reynolds number is below 0.03, thanks to the use of highly viscous silicon oil. We used the oils $M5.000$ ($\nu = \eta/\mu \sim 5.000$ mm^2/s which is 5.000 times more viscous than water) and $M10.000$ (10.000 times more

viscous) from *Carl Roth*. Thus inertial effects are negligible compared to viscous effects, and the Stokes equation is valid indeed.

3.1.5 Bonus for non-nano pores: influence of inertia

In nanosytems, the flow is laminar by nature thanks to the dimensions of the systems. With millimetric pores, it is possible to access to higher Reynolds number. By decreasing the viscosity of the silicon oil, we reached Reynolds number as high as 60. Such values of $\mathcal{R}_e$ can be encountered in many industrial situations, for example in agribusiness for fluid filtration (milk, juice...). While we were working on our first experiments, Jensen *et al.* [72] proposed a rationalization of the hydrodynamic resistance dependence with the Reynolds number, accounting for small inertial effects. They analysed the only experimental data available, dating back to 1921 (by Bond [92]) and 1930 (by Johansen [93]) and proposed from dimensional analysis that the access resistance follows

$$R^0_{\text{acc}} = \frac{\eta}{a^3}\left(3 + \frac{\mathcal{R}_e}{\pi}\right), \tag{3.24}$$

which reflects the experimentally noticed rise of access resistance with $\mathcal{R}_e$. However, experimental data show a slight deviation from Eq. 3.24, as the access resistance only departs from Sampson formula $R^0_{acc} = 3\eta/a^3$ from a threshold, called $\mathcal{R}^t_e$. Rather, the access resistance seems to follow the empirical formula

$$R^0_{\text{acc}} = \frac{\eta}{a^3}\left(3 + f(\mathcal{R}_e)\right), \tag{3.25}$$

with

$$f(\mathcal{R}_e) = \begin{cases} 0 & \text{if} \quad \mathcal{R}_e < \mathcal{R}^t_e \\ \dfrac{\mathcal{R}_e - \mathcal{R}^t_e}{\pi} & \text{if} \quad \mathcal{R}_e > \mathcal{R}^t_e. \end{cases} \tag{3.26}$$

The value of $\mathcal{R}_e^t$ is found to be 4 in Johansen work, and around 6 in Bond work. We led experimental investigations to check formulas 3.25 and 3.26, and see how they are affected by the presence of hydrodynamic interactions, which, to our knowledge, has never been studied.
In the next section, we will present the experimental setup used to measure the hydrodynamic resistance of regular arrays of pores. Then, we will present our results for creeping flows (experiments where $\mathcal{R}_e < 0.03$) and laminar flows with correction inertial effects ($\mathcal{R}_e < 60$) in sections 3.3 and 3.4 respectively.

3.2 Experimental setup

3.2.1 Design of multipore network membranes

For this study, we used 19 different membranes with 3 to 127 circular pores, most often disposed in a regular hexagonal arrangement, see Fig. 3.4. Two membranes presented a different geometry: 7 pores in line or 37 pores on a circle (supposed to approximate closely the behavior of 37 pores in line). These membranes were 3D printed with the rigid and opaque photopolymer *VeroWhitePlus*. Their radius is about 5 cm and their thickness is ℓ =500 μm, enough to ensure their indeformability under a flow, even though membranes could be slightly bent by hand. The pore radii were varied from 1.25 mm to 4 mm so that $a/\ell > 1$ and the flow is indeed governed by entrance effects. The smallest interpore distance accessible is $2a$+500 μm, so the maximal value of a/L is 0.47, close enough to the higher limit of 0.50 where pores are brought in contact.

The experiments we perform require a thorough control of the pore size, because hydrodynamic resistance strongly depends on the pore

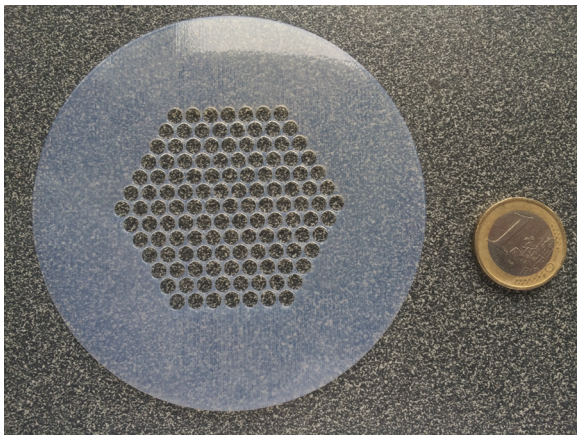

FIGURE 3.4: Picture of one of the 3D-printed membranes, with an hexagonal array of 127 pores of radius $a = 2$ mm

radius, as $1/a^3$ for flows governed by entrance effects. Moreover, hydrodynamic interactions depend mainly on $(a/L)^3$ (with L the next neighbor distance). Pore size is thus the most important parameter in this study. To control the pore shape, we scanned the membranes with a high resolution (typically 5.000 pixels per inch). We found a good circularity and reproducibility of the pores. We noticed that the two sides of the pores were not exactly equivalent, see Fig. 3.5. This is due to the process of fabrication, during which liquid polymer is deposited layer by layer. The first layer goes on a substrate that prevents the polymer from creeping and imparts its roughness to the polymer, once dried. As for the last layer, only the previous layers hold it during the few seconds it takes to dry. This last layer thus forms a smooth side, and the material around the pores tends to retract a bit, forming a flared aperture with a small bump on top, see Fig. 3.5-b. The slightly conical shape of the pores was further confirmed by mechanical profilometry, see Fig. 3.6.

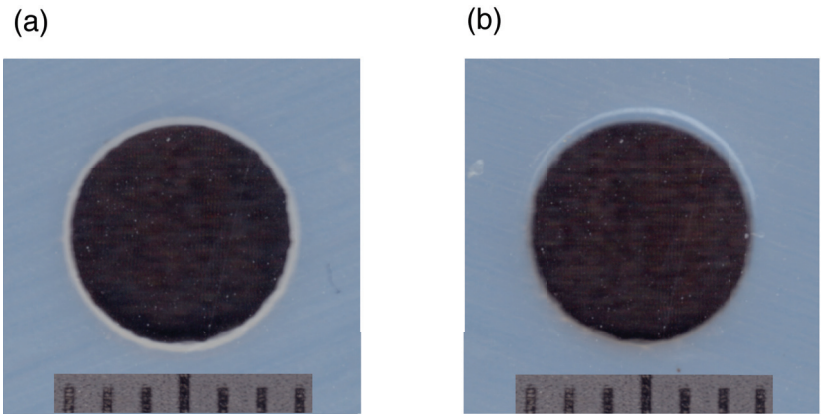

FIGURE 3.5: Scans of the central pore in a 7-pore membrane, of radius 3 mm. Black lines are spaced with 1 mm. (a) Rough side and (b) smooth side of the membrane. The white circle visible above the pore is the little bump of polypropylene (see text).

From images similar as Fig. 3.5, we extracted the "rough side" radius values which were always roughly 130 μm less than the nominal radius. On the contrary the bump radius was about 150 μm more than the nominal radius. We have a precision of 30 to 50 μm on these values depending on the membranes, which is better than the profilometry resolution. We started by analysing the data taking into account three different local radii: the rough side one and the smooth side one for the access resistance, and an average between them for Poiseuille resistance. But we saw no difference compared to the analysis with only an average value, equal to or very close to the nominal value. We thus kept the simpliest analysis with only one radius value, with an uncertainty of 30 or 50 μm.

We now turn to the measurement of the oil viscosity.

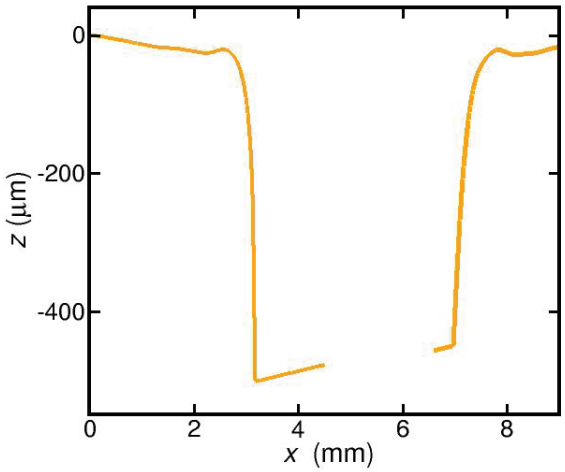

FIGURE 3.6: Mechanical profilometry of a nominally 2-mm radius pore. z is the pore axis and x a transverse axis, along which the needle has a constant transverse velocity. Initially the needle is brought in contact with the smooth side of the membrane. For $0 < x < 2$ mm the needle is slowly approaching the pore. Then it feels the bump and the flared pore aperture. It enters the pore and bounces off the support in $z = -500$ μm. Then it exits the pore and jumps again the bump. The local radii given here are mere indications.

3.2.2 Measure of the oil viscosity

Silicon oil viscosity sharply depends on temperature. As the data furnished by the producer were not satisfactory, we measured the oil viscosities with a Ubbelhode capillary viscosimeter [94]. As capillary viscosimeters should be used in the laminar regime, the choice of the capillary radius has to be adapted to the fluid viscosity. We thus used one viscosimeter for kinematic velocities between 1000 and 10000 mm^2/s, and a different one for ν =100 mm^2/s.

These viscosities were measured at two different temperatures, at the two

extremes of the temperature range of the experimental campaigns. The highest temperature was around 28°C by a hot day in the experiment room, and the lowest around 20°C in an air conditioned room. We then used a linear adjustment between the 2 measured values. The fluid temperature was recorded during each experiment, which will be precised below along with the whole experimental procedure.

3.2.3 Experimental protocol

To study the influence of hydrodynamic interactions on flow, we recorded the gravity drainage of a 4 cm radius cylinder, under which we had glued one of the membranes described in 3.2.1. At the beginning, we fill a wide reservoir with 5 cm of silicon oil. We then place the cylinder with the glued membrane above the reservoir, such as the membrane is just immersed in the oil (see Fig. 3.7). The cylinder is in turn filled with silicon oil and we record its emptying with either a low-speed camera (*Marlin, Allied Vision*) or a high-speed camera (*Phantom*), depending on the flow rate. We also recorded the rise of the oil level in the reservoir. We used frame rates between 0.1 and 120 frames per second. A ruler served as a referral for pixels-meters conversions. The temperature was monitored during the experiment with a digital thermometer (*Roth*), glued on the side of the cylinder such as the probe is at the pores level. A sketch of the setup can be found in Fig. 3.8-a, and a example of image recording is on Fig. 3.8-b.

In the following, z_B and z_A refer to the vertical position of the bottom of the meniscus in the cylinder, and of the top of the meniscus in the reservoir respectively (see Fig. 3.8-a). For low-speed flow, the interface at z_A could reasonably be considered as flat so we used the $z_A(t)$ data. In the majority of cases, the oil surface in the reservoir was not flat, so we discarded the reservoir filling and focused on the cylinder draining.

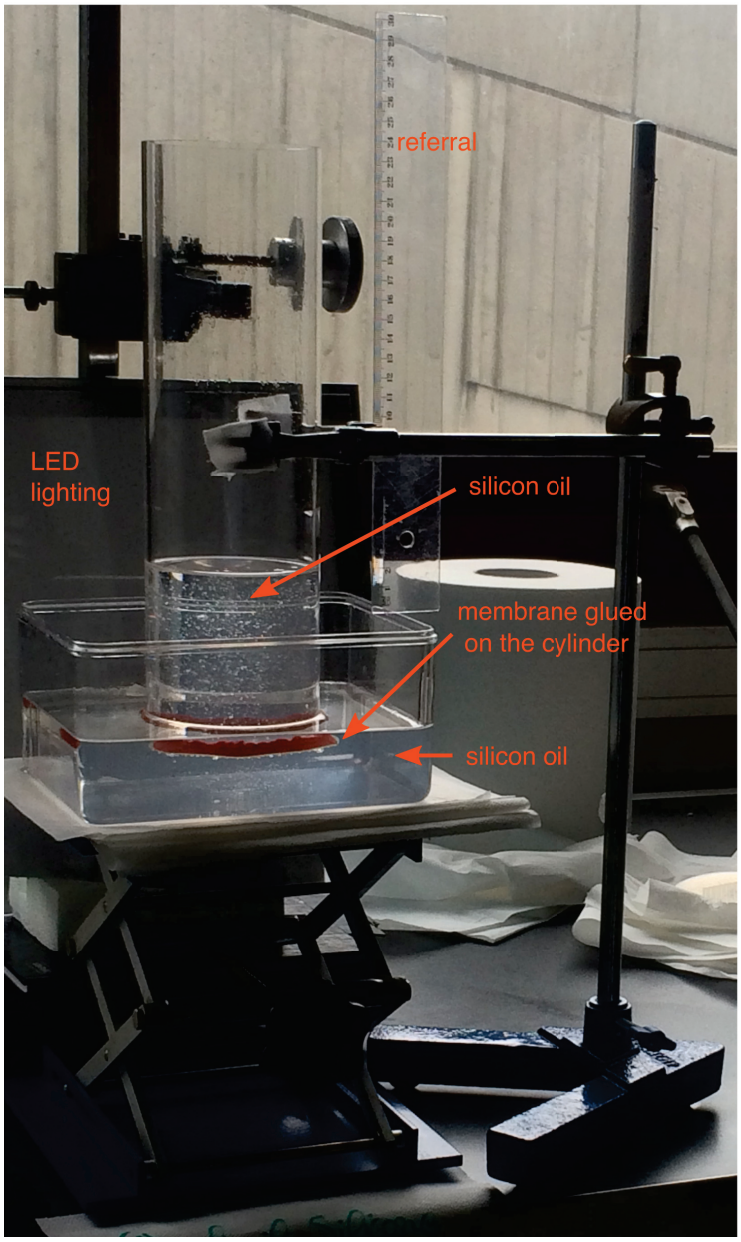

FIGURE 3.7: Photograph of the setup

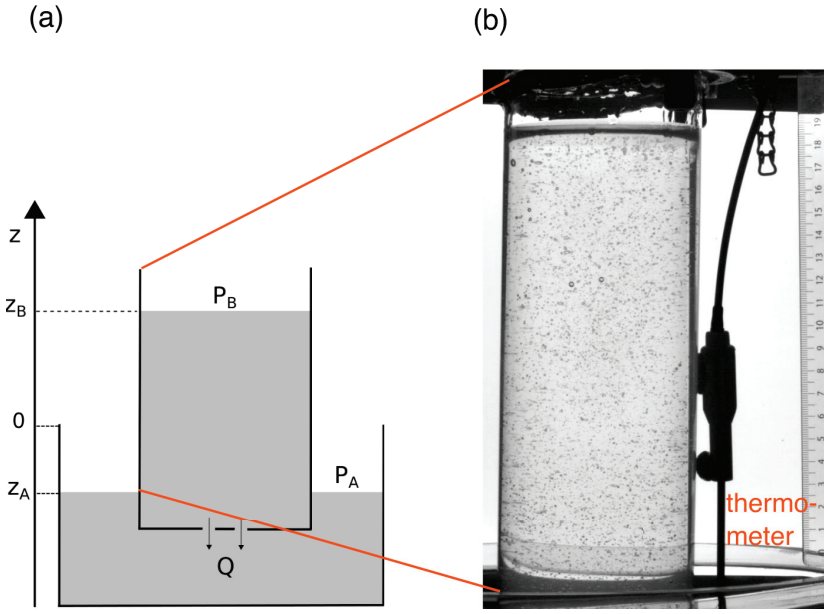

FIGURE 3.8: (a) Sketch of the setup with the position of the front in the cylinder z_B and in the reservoir z_A. At the air-oil interface, $P_B = P_A = P_{\text{atmo}}$. Q is the flux rate through the pores. (b) Example of a recorded image, focused on the upper part of the cylinder.

• *Computation of R, first method*

From the recording of the position of the meniscus $z_B(t)$ (and also $z_A(t)$ for low-speed flow), the hydrodynamic resistance R can be computed as

$$R = \frac{\Delta P}{Q} \tag{3.27}$$

with ΔP the hydrostatic pressure $\Delta P = \mu g(z_B - z_A)$ and Q the flux rate given by

$$Q = S_A \dot{z}_A = -S_B \dot{z}_B, \tag{3.28}$$

where $\dot{z}_{A/B} = \dfrac{\mathrm{d}z_{A/B}}{\mathrm{d}t}$, S_B is the cylinder section and S_A the reservoir section minus the cylinder section. From the flux rate conservation in Eq. 3.28 one gets

$$z_A(t) = -\frac{S_B}{S_A} z_B(t) \quad , \quad z_B(t) = -\frac{S_A}{S_B} z_A(t) \tag{3.29}$$

with the integration constant $z_B^\infty = z_A^\infty = 0$. We thus have

$$R = \mu g \left(\frac{1}{S_B} + \frac{1}{S_A} \right) \frac{z_B}{-\dot{z}_B} = \mu g \left(\frac{1}{S_B} + \frac{1}{S_A} \right) \frac{-z_A}{\dot{z}_A}. \tag{3.30}$$

z_B was extracted with *ImageJ* software from the recordings. To compute $\dot{z}_B$, we linearized portions of 60 points of the $z_B(t)$ curve (each curve $z_B(t)$ had around 500 points), and attributed their slope to $\dot{z}_B$ (see Fig. 3.9).

- *Computation of R, second method*

There is another way to compute R for low Reynolds numbers. As we mentioned in Eq. 3.25 and 3.26, for $\mathcal{R}_e < \mathcal{R}_e^t \sim 4$, the hydrodynamic resistance is constant during the flow. In that case, integrating Eq. 3.30 yields

$$z_{A/B}(t) = z_{A/B}^0 \exp\left(-\frac{\mu g}{R} \left(\frac{1}{S_B} + \frac{1}{S_A} \right) t \right). \tag{3.31}$$

Eq. 3.31 provides the easiest way to determine R. Using *Matlab*, we fitted the curves $z_B(t)$ (and $z_A(t)$ when usable) by an exponential with 3 free parameters α, β and γ:

$$z_{A/B} = \alpha + (\beta - \alpha) \exp\left(-\frac{\mu g}{\gamma} \left(\frac{1}{S_B} + \frac{1}{S_A} \right) t \right), \tag{3.32}$$

see Fig. 3.10. We took γ as the hydrodynamic resistance value. To fit $\ln z$ as function of time would have given a linear fit, but rather, we chose to fit z as a function of time because it allowed us not to convert

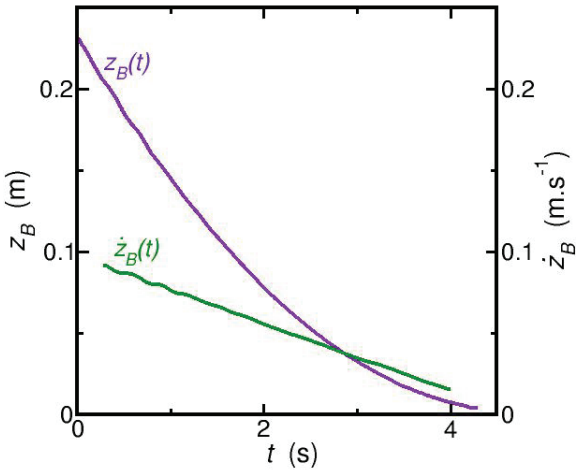

FIGURE 3.9: Evolution of the meniscus position $z_B(t)$ (purple) and of the computed meniscus velocity $\dot{z}_B(t)$ as a function of time, for a drainage of silicon oil M100 through 7 pores of radius $a = 4$ mm, $L = 8.5$ mm ($10 < \mathcal{R}_e < 60$).

from pixels to meters, and also not to shift $z_{A/B}$ to have $z_B^\infty = z_A^\infty = 0$. Indeed, we previously checked that the fit parameter γ was unchanged when shifting and/or converting from pixels to meters.

- *Consistency of the two methods for low $\mathcal{R}_e$*

We compared the values of the resistance given by the two methods, in a case where they are both valid. We computed the hydrodynamic resistance R_7 of 7 non-interacting pores of radius $a = 1.5$ mm. We used an oil of viscosity $\nu = 5000$ mm^2/s^{-1} which ensured a Reynolds number $\mathcal{R}_e < 0.01$. As can be seen on Fig. 3.11, the two methods are in excellent agreement during the first part of the draining. Then, as z_B and $\dot{z}_B$ tend to 0, their ratio and subsequently hydrodynamic resistance are subjected to strong fluctuations. Thus, to extract hydrodynamic resistance with method 1, one should keep only the data corresponding

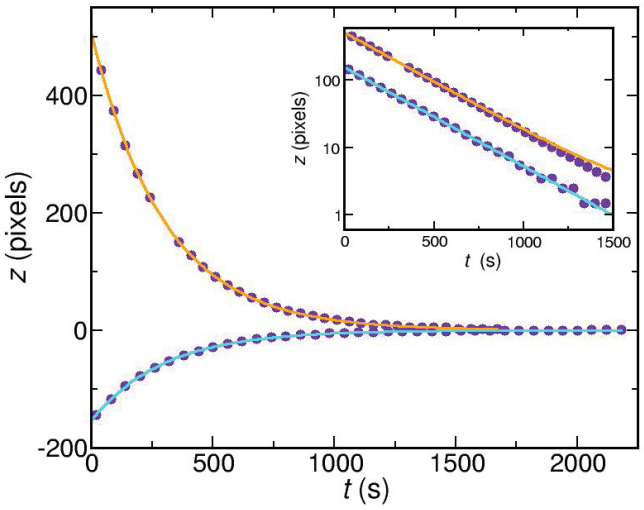

FIGURE 3.10: Evolution of the meniscii positions as a function of time, for a drainage of silicon oil M10.000 through 7 pores with $a = 2$ mm and $L = 4.5$ mm ($\mathcal{R}_e < 0.03$). Points represent experimental data. For the sake of clarity we kept only 1/20th of the available data. Orange and turquoise lines are fits using Eq. 3.32. *Inset*: idem with a semi-log scale. The data were previously shifted to have $z_B^\infty = z_A^\infty = 0$.

to the begining of the experiment. As the second method was easier to implement, we sticked to it for all the experiments with $\mathcal{R}_e < 4$.

• *Computation of the Reynolds number*

As presented in section 3.1.4, we define the Reynolds number as $\mathcal{R}_e = \dfrac{av}{\nu}$ with v the average velocity inside the pore. v is computed using the flux conservation :

$$N(\pi a^2)v = S_B|\dot{z}_B| \tag{3.33}$$

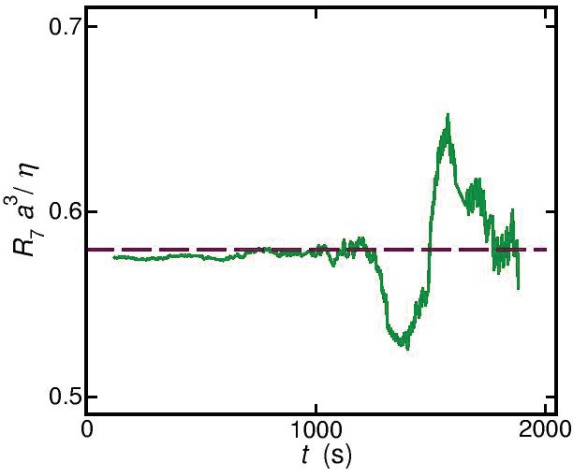

FIGURE 3.11: Normalized resistance of 7 non-interacting pores of radius $a = 1.5$ mm, as a function of time. The green curve is the result of method 1, while the brown dashed line is the result of the fit using method 2. The agreement between the 2 methods is excellent during the first half of the draining. Then, z_B and $\dot{z}_B$ tend to 0 which causes their ratio to undergo strong fluctuations.

which yields $v = |\dot{z}_B| \dfrac{S_B}{N\pi a^2}$. Thus

$$\mathcal{R}_e = \frac{|\dot{z}_B| S_B}{\nu N \pi a}. \tag{3.34}$$

We now turn to the results given by experiments with low Reynolds number flows.

3.3 Hydrodynamic interactions at low Reynolds number

The center of this chapter is the experimental study of hydrodynamic interactions in creeping flows. As a way to calibrate the experiment, we started by studying membranes with non interacting pores.

3.3.1 Preliminary verification with independent pores

We knew for theoretical formula such as 3.18 that hydrodynamic interactions can be detected only for pores spaced with less than four radii, *i.e.* $L < 4a$ (this will be verified in Section 3.3.2). The membranes we present now contain 7 pores on an hexagonal pattern. with pore spacing L such that $L/a \geq 6$. We verify that we recover the Weissberg-Sampson-Poiseuille approximation for flows through independent pores of varying radii from 1.25 mm to 4 mm, see Fig. 3.12. For 7 independent pores, Poiseuille resistances and non-modified Sampson resistances can be used. The total hydrodynamic resistance R_7 writes

$$R_7 = K_7^{-1} \tag{3.35}$$

$$= \left(7K_1^0\right)^{-1} \quad \text{as permeabilities add up in parallel} \tag{3.36}$$

$$= \frac{1}{7}\left(R_{acc}^0 + R_{in}\right) \tag{3.37}$$

$$= \frac{1}{7}\left(\frac{3\eta}{a^3} + \frac{8\eta\ell}{\pi a^4}\right). \tag{3.38}$$

We use the superscript O in K_1^0 and R_{acc}^0 to stress the non-interaction between pores. The subscript refers to the number of pores. K_1^0 thus represents the permeability of one isolated pore, while R_7 is the resistance of 7 possibly interacting pores.

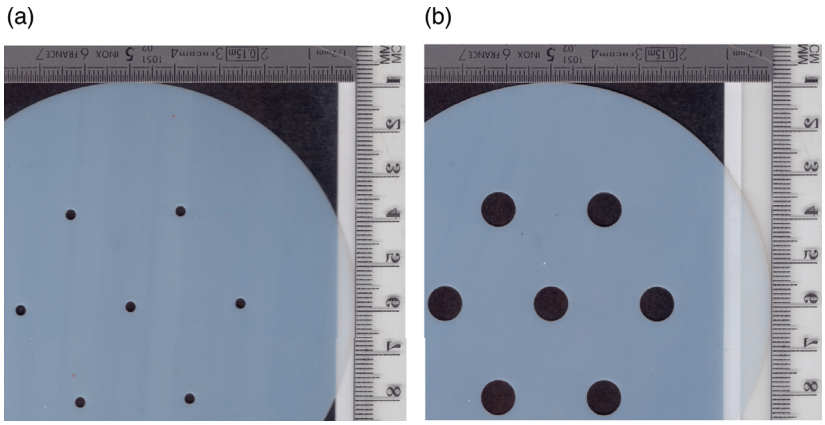

FIGURE 3.12: Scans of 2 membranes with non interacting pores. (a) a=1.25 mm, $L = 19a$ (b) a=4 mm, $L = 6a$.

Following Eq. 3.38, one expects

$$\frac{R_7 a^4}{\eta} = \frac{1}{7}\left(3a + \frac{8\ell}{\pi}\right). \tag{3.39}$$

In Fig. 3.13 we reported the experimental values of $\frac{R_7 a^4}{\eta}$ obtained from four independent drainings. Here η is the dynamic viscosity calculated at the temperature of the experiment. The error bars have two contributions: first the uncertainty on the experimental measurement of R_7/η. $\Delta\frac{R_7}{\eta}$ is the standard deviation of this parameter. The second and main contribution comes from the uncertainty on the pores radii, $\Delta a = 30$ μm. To compute the height of the error bars we used the formula

$$\Delta f(x_1, x_2) = \sqrt{\left(\frac{\partial f}{\partial x_1}\Delta x_1\right)^2 + \left(\frac{\partial f}{\partial x_2}\Delta x_2\right)^2} \tag{3.40}$$

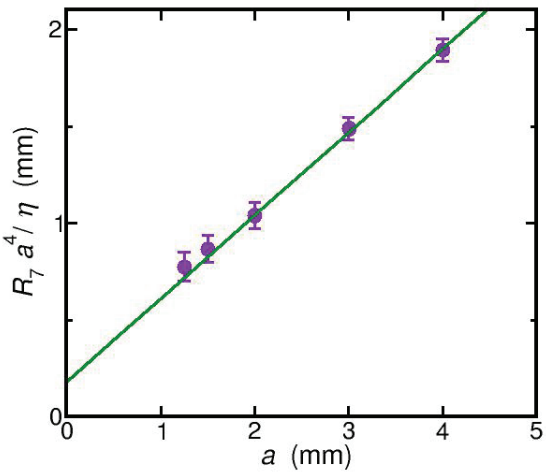

FIGURE 3.13: Hydrodynamic resistance of seven non-interacting pores, times a^4/η. Purple points represent experimental data, see text for details on the points and error bars. The green line is a theoretical prediction from Eq. 3.39, accounting perfectly for the experimental data

.

which in our case reads

$$\Delta\left(\frac{R_7 a^4}{\eta}\right) = \sqrt{\left(a^4 \Delta\frac{R_7}{\eta}\right)^2 + \left(\frac{4R_7 a^3}{\eta}\Delta a\right)^2}. \tag{3.41}$$

The error bars in Fig. 3.13 thus stand for $\pm\Delta\left(\frac{R_7 a^4}{\eta}\right)$. The theoretical curve $y = \frac{1}{7}\left(3x + \frac{8\ell}{\pi}\right)$ matches exactly the experimental data, so we can conclude that the Weissberg-Sampson-Poiseuille approximation is well captured by our experiments. We can thus safely analyze hydrodynamic interactions with this experimental set-up.

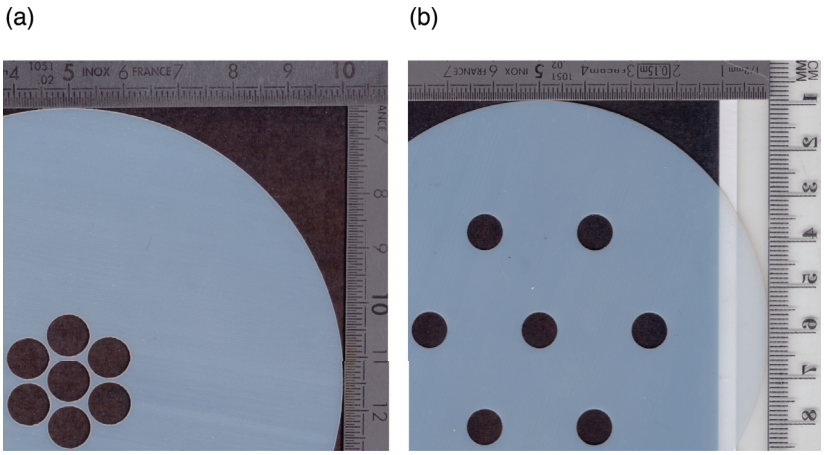

FIGURE 3.14: Scans of 2 membranes with 4 mm-radii interacting pores. (a) $L = 8.5$ mm$= 2.125\,a$, (b) $L = 24$ mm$= 6\,a$.

3.3.2 Dependency of the permeability with pore distance

We now turn to the study of flows through interacting pores. We used membranes with 7 pores of radii $a = 4$ mm ($\ell/a = 0.125$) on an hexagonal pattern. The interpore distance is varied from $L = 2.125\,a$ to $L = 6\,a$, see Fig. 3.14. For interacting pores, formula 3.38 does not hold anymore. It is easier to consider here hydrodynamic permeabilities, which add up as

$$K_7 = \sum_{j=1}^{7} K_1^j \tag{3.42}$$

$$= \sum_{i=1}^{7} \left(R_{acc}^i + R_{in}\right)^{-1}. \tag{3.43}$$

Note that pores are not equivalent here. The central pore has more interactions with its neighbors than the exterior ones. According to Tio and Sadhal, the access resistance of a given pore i writes (see Eq. 3.18)

$$R_{acc}^{i} = R_{acc}^{0} \times \left(1 - \lambda^{i}\right) \tag{3.44}$$

with $R_{acc}^{0} = 3\eta/a^3$ and

$$\lambda^{i} = \sum_{j,j\neq i} \left[\frac{2}{3\pi} \left(\frac{a}{L_j}\right)^3 + \frac{6}{5\pi} \left(\frac{a}{L_j}\right)^5 + \frac{18}{7\pi} \left(\frac{a}{L_j}\right)^7 + \frac{56}{9\pi} \left(\frac{a}{L_j}\right)^9 \right] \tag{3.45}$$

where the summation is on all other pores, labeled i. L_j is the distance between the center of the pore considered i, and the center of the pore j. We left out the higher order terms. For regular arrays a/L_j is always a fraction of a/L, with L the next-neighbor distance. Thus, λ^i depends on a/L, on the number of pores N and on the geometry of the array. Here we consider only the dependency in a/L. Normalizing Eq. 3.43, we get

$$\frac{K_7}{7K_1^0} = \frac{1}{7} \sum_{i} \left(R_{acc}^{0}(1 - \lambda^{i}(\frac{a}{L})) + R_{in} \right)^{-1} \times \left(R_{acc}^{0} + R_{in} \right) \tag{3.46}$$

$$= \frac{1}{7} \sum_{i} \left(1 - \frac{\lambda^{i}(\frac{a}{L})}{1 + R_{in}/R_{acc}^{0}} \right)^{-1} \tag{3.47}$$

$$= \frac{1}{7} \sum_{i} \left(1 - \frac{\lambda^{i}(\frac{a}{L})}{1 + \frac{8\ell}{3\pi a}} \right)^{-1} . \tag{3.48}$$

We confront Eq. 3.48 to the experiments in Fig. 3.15. Each value of the experimental permeability K_7 is normalized by the calculated permeability of an isolated pore K_1^0 at the same temperature. As in Section 3.3.1, the dots in Fig. 3.15 stand for the mean of $K_7/7K_1^0$ on 4

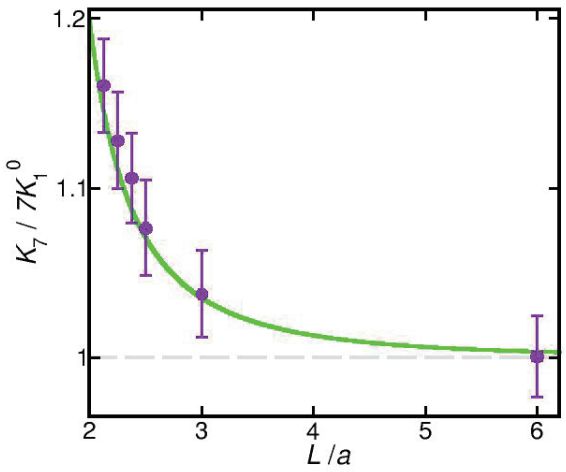

FIGURE 3.15: Permeability of 7-pore clusters, with radii $a = 4$ mm, normalized by seven times the permeability of an isolated pore, as a function of the next-neighbor distance L normalized by the pore radius. Experiments (purple dots) were performed with an oil viscosity of 1000 mm^2/s. See text for details. The green curve is the theoretical prediction of Eq. 3.48.

drainings. Similarly, vertical error bars take into account the standard deviation on $K_7\eta$ and the uncertainty of 30 μm on a. The horizontal error bars are smaller than the points width. The adequation between experiments and theory is very good. The increase in permeability almost reaches 20% for pores in contact. Hydrodynamic interactions can be neglected when pores are spaced with $6a$ or more.

To complete this study, Simon Gravelle performed finite-element simulations with the *Comsol* software. He created a 3D structure with two reservoirs on both sides of a membrane with pores disposed on a regular hexagonal array. Pore aspect ratio is $\ell/a = 0.25$, similar to experimental membranes of radius 2 mm. The first two systems present 3 and 7 pores. A third system consists in two quarters of pores and

symmetrical boundary conditions, to simulate an infinite membrane, see Fig. 3.16. For these three systems, the next-neighbor distance L is varied from $L = 2a$ to $L = 6a$. A no-slip condition is imposed on the walls. A pressure drop of 1 Pa is imposed between the ends of the two reservoirs, and the Stokes equation is solved. The flux rate is recorded as a function of the interpore distance.

• *3- and 7-pore systems*

We expect the normalized permeability of the cluster of pores, $K_3/3K_1^0$ or $K_7/7K_1^0$, to be described by Eq. 3.48. As pores spaced with roughly six times their radius can be considered as independent (see Fig. 3.15), the normalized permeability was computed as the ratio of the flux rate at L/a over the flux rate for most distant pores, *i.e.* $L/a = 6$.

• *Infinite membrane*

For the simulations of the infinite membrane, we plot in Fig. 3.17 the normalized permeability of 1 pore, K_1/K_1^0, as all pores are equivalent in this case. It means that the correction to access resistance λ^i is independent on the pore: $\lambda^i = \lambda(\frac{a}{L})$ and

$$\frac{K_1}{K_1^0} = \left(R_{acc}^0(1 - \lambda(\frac{a}{L})) + R_{in}\right)^{-1} \times (R_{acc}^0 + R_{in}) \tag{3.49}$$

$$= \left(1 - \frac{\lambda(\frac{a}{L})}{1 + \frac{8\ell}{3\pi a}}\right)^{-1} . \tag{3.50}$$

λ is an infinite sum which can be calculated thanks to

$$\sum_{i \neq j} \left(\frac{a}{L_i}\right)^k = \left(\frac{a}{L}\right)^k \times H_k \tag{3.51}$$

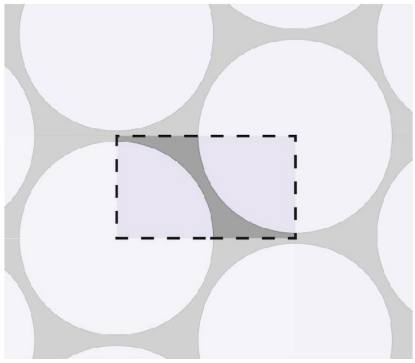

FIGURE 3.16: Draw of the system used to simulate an infinite membrane. Dashed lines represent the boundary of the system, on which we applied symmetric conditions.

with

$$H_k = \lim_{N\to\infty}\left[6\sum_{n=1}^{N}\frac{1}{n^k} + 6\sum_{n=1}^{N-1}\sum_{m=n+1}^{N}\frac{1}{(m^2-mn+n^2)^{k/2}}\right]. \quad (3.52)$$

Tio and Sadhal give the numerical values of H_3, H_5, H_7 and H_9 [90]. As for 3- and 7-pore systems, the normalized permeability was computed as the ratio of fluxes at L/a and $L = 6a$.

Fig. 3.17 evidences a clear increase of the permeability when pores are brought closer, as we already noticed in experimental data in Fig. 3.15. The agreement between the theory of modified entrance effects (Eq. 3.44 and 3.45) and simulations is very good. Two experimental data from experiments on 3 and 7 pores also are fully compatible with the model and simulations. However, we note that numerical results slightly exceed theoretical ones at short interpore distances. This may be explained by the higher order terms in Eq. 3.45 which we discarded.
What is more, as pore interactions are additive, we can see in Fig. 3.17

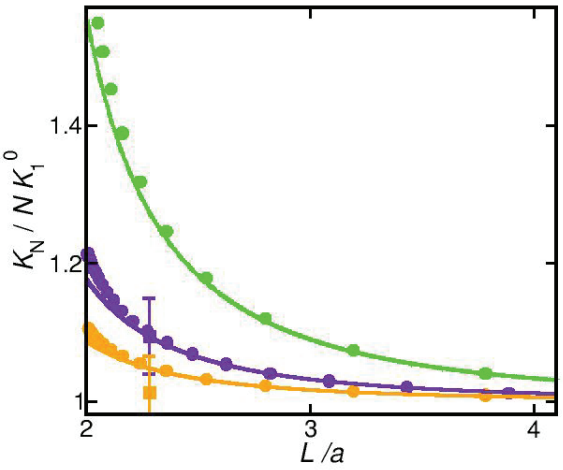

FIGURE 3.17: Permeability of N-pore clusters, with radii $a = 2$ mm, normalized by N times the permeability of an isolated pore, as a function of the next-neighbor distance L normalized by the pore radius. $N = 3$ (orange), $N = 7$ (purple) and $N = \infty$ (green) (in the latter case the ordinate is K_1/K_1^0, see text). Filled circles represent numerical simulation results, solid lines are theoretical predictions from Eq. 3.48 and 3.50, and squares with error bars are experimental results.

that this increase of the permeability depends on the size of the array of pores. The more pores, the stronger the hydrodynamic interactions between pores until they converge for an infinite array. For an infinite hexagonal array of pores with $\ell/a = 0.25$, the normalized hydrodynamic permeability converges to 1.6 for pores in contact (see Fig. 3.17). This means that the hydrodynamic permeability is always extensive, even if corrections have to be added.

The last part of our study at low Reynolds number consists in analyzing more precisely the influence of the geometry and the number of pores on the cluster permeability.

3.3.3 Dependency of the permeability with the array geometry

To study the dependency of the permeability with the number of pores, we used membranes with 3 to 127 pores on an hexagonal array. Not only the pattern under the pore arrangement was hexagonal, but also the shape of the cluster of pores itself (aside from the triangular 3-pore cluster), see Fig. 3.4. All pores have a nominal radius of 2 mm and the next neighbor-distance is fixed at 4.5 mm. We also used 1 membrane with 7 independent pores ($L = 12\,a$) to account for the $N = 1$ case.
In order to compare the effect of a linear geometry to an hexagonal one, we also used a membrane with 7 pores in line, and a membrane with 37 pores on a circle. The interpore distance was also $L = 4.5$ mm $= 2.28\,a$ in these last two cases.
For all these membranes, the scans revealed a radius slightly smaller than the nominal. We used a value of $a = 1.97$ mm.
As in the previous section 3.3.2, we normalized the experimental permeability by N times the permeability of a single isolated pore at the same temperature. In Fig. 3.18, we plot the mean on 4 drainings of these normalized permeabilities. As in the previous chapters, error bars come from the standard deviation of $K_N\eta$, plus an uncertainty of 30 μm on the pore radius.
The clear increase of the normalized permeability with the number of pores we saw in Fig. 3.17 is confirmed in Fig. 3.18. From 1 to 37 pores on an hexagonal array, the normalized permeability increases by 15%. 7 pores in line or 37 pores on a circle show a less marked increase of the normalized permeability, which is explained by a lower coordination number than in an hexagonal geometry. Hydrodynamic interactions are thus less intense.
The theoretical normalized permeability writes similarly to the 7-pore

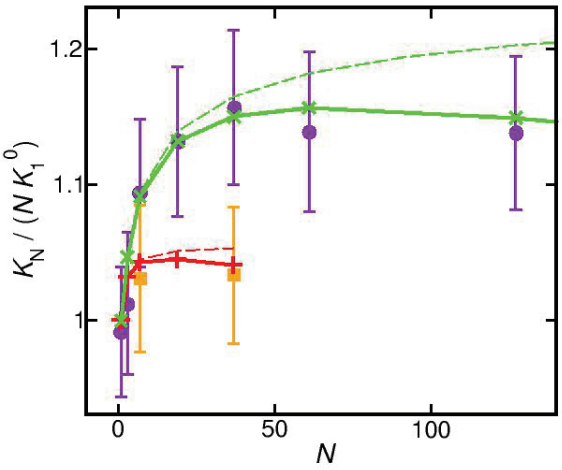

FIGURE 3.18: Normalized permeability N-pore of clusters, from $N = 1$ to $N = 127$ for hexagonal arrays of pore (purple circles and green crosses), and from $N = 1$ to $N = 37$ for pores in line (orange squares and red crosses). The normalization takes into account a radius of 1.97 mm and nearest pores are spaced with 4.5 mm. Circles and squares with error bars are experimental results. Green and red crosses are theoretical data taking into account an additional resistance $R_{\text{res}} = 1.5$ Pa.s.m^{-3}, see text. Solid lines are only guides for the eye. Dashed lines show the evolution of theoretical normalized permeability with no additional resistance.

case,

$$\frac{K_{\text{N}}}{NK_1^0} = \frac{1}{N}\sum_{i=1}^{N}\left(1 - \frac{\lambda^i(N, geometry)}{1 + \dfrac{8\ell}{3\pi a}}\right)^{-1}, \tag{3.53}$$

which we calculated for an hexagonal and a linear geometry. We can see in Fig. 3.18 that this expression (green and red dashed lines) accounts for the sharp increase of normalized permeability at $N < 37$.

If the number of pores is increased beyond $N = 37$, the experimental normalized permeability remains stagnant. Theoretical predictions of

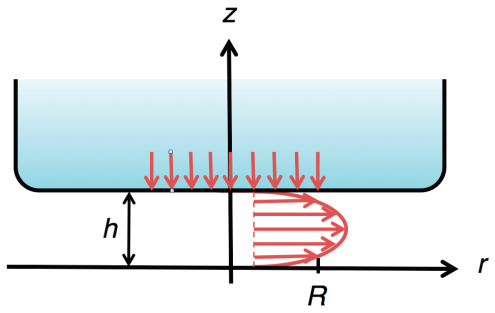

FIGURE 3.19: Sketch of the Poiseuille flow between the membrane (in $z = h$) and the bottom of the reservoir (in $z = 0$). The vertical red arrows represent flows through the pores, which are located between $r = 0$ and $r = R$.

the permeability show an attenuated increase beyond $N = 37$ (and converge toward $K_{\mathrm{N}}/(NK_1^0) = 1.27$ for $N \to \infty$), however they exceed experimental values. This can be explained by the presence of an additional resistance on the flow, most probably from the bottom of the reservoir. The order of magnitude of this resistance can be evaluated considering an horizontal Poiseuille flow below the membrane, see Fig. 3.19. Neglecting any vertical pressure gradient, the fluid velocity between the membrane and the bottom of the reservoir is purely radial: $\vec{v} = v(z)\overrightarrow{e_r}$. r and z are here cylindrical coordinates and $\overrightarrow{e_r}$ is a unit vector. We note h the distance between the membrane and the bottom reservoir. Given the Stokes equation, the velocity field is

$$\vec{v} = -\frac{\partial_r P}{\eta} z(z-h)\overrightarrow{e_r} \tag{3.54}$$

with $\partial_r \nabla P$ the pressure gradient along the radial direction. As the pore array is localized between $r = 0$ and $r = R$ (see Fig. 3.19), the flux crossing a cylinder of radius r increases as r increases from 0 to R. The

total flux Q reads

$$Q \times \frac{r^2}{R^2} = 2\pi r \int_0^h v(z)\,\mathrm{d}z. \tag{3.55}$$

After a few manipulations, one gets the pressure field between $r = 0$ and $r = R$:

$$P(r) = Q\frac{3\eta}{2\pi h^3}\left(\frac{r}{R}\right)^2 + P(r=0). \tag{3.56}$$

For $r > R$, the pressure field increases more slowly, in $\ln r$. An order of magnitude of the additional resistance due to the bottom reservoir is thus given by $R_{\mathrm{res}} \sim 3\eta/(2\pi h^3)$. In these experiments $h \sim 2$ cm, which gives $R_{\mathrm{res}} \sim 10^6$ Pa.m^{-3} ($\eta \sim 10$ Pa.s). If one adds this new resistance in series with the parallel resistances of the pores, we get

$$R_1^0 = R_{\mathrm{acc}}^0 + R_{\mathrm{in}} + R_{\mathrm{res}} \tag{3.57}$$

$$R_N = \left[\sum_{i=1}^{N}\left(R_{\mathrm{acc}}^i + R_{\mathrm{in}}\right)^{-1}\right]^{-1} + R_{\mathrm{res}} \tag{3.58}$$

and thus

$$\frac{K_N}{NK_0^1} = \left(\left(\frac{1}{N}\sum_{i=1}^{N}\left(1 - \frac{\lambda^i(N, geometry)}{1 + R_{\mathrm{in}}/R_{\mathrm{acc}}^0}\right)^{-1}\right)^{-1} + \frac{NR_{\mathrm{res}}}{R_{\mathrm{acc}}^0 + R_{\mathrm{in}}}\right)^{-1}. \tag{3.59}$$

With $R_{\mathrm{res}} = 1.5 \times 10^6$ Pa.s.m^{-3}, we get a good agreement with the experimental data. Note that the supposed dependency of R_{res} in $1/h^3$ makes R_{res} negligible compared to Poiseuille resistances inside the pores and access resistance, when $h = 5$ cm which is the case in all the other experiments.

In sections 3.3.2 and 3.3.3, we investigated the influence of the normalized interpore distance L/a, the number of pores and the array geometry on hydrodynamic interactions. In full agreement with the

model proposed by Tio and Sadhal (Eq. 3.18), hydrodynamic interactions enhance the flow through pores compared to an isolated pore situation. Their scope is quite small (an increase of 5% in normalized permeability is noted for 7 pores with $L \approx 3a$), and so is their strength (a maximal 20% increase for 7 pores brought in contact). An important fact is that the permeability keeps an extensive behavior: the normalized permeability of an infinite array converges, even when pores are brought in contact. Finally, the addition of pores increases the strength of interactions, which is clearly seen for small number of pores (typically $N < 40$). Above this value, the addition of pores have much less impact and interactions saturate.

We now turn to hydrodynamic interactions in laminar flows where inertial effects begin to have an impact. The Reynolds number in these cases is between 10 and 60.

3.4 Hydrodynamic interactions at $\mathcal{R}_e$ >10

To access to higher Reynolds numbers, we used a silicon oil of kinematic viscosity 100 mm^2/s (silicon oil $M100$). We could reach $\mathcal{R}_e = 60$. The membranes we used were already presented in section 3.3.2: 7 pores of radius $a = 4$ mm, with interpore spacing between 8.5 mm ($L/a = 2.125$) and 12 mm ($L/a = 3$). Because of the flow speed, we had to plug the pores during the cylinder filling, and then to remove the plug quickly when starting the recording.
In a first time, we show that the hydrodynamic resistance is not constant during one experiment. To determine R we thus stick to the first method described in section 3.2.3. Then we show that hydrodynamic interactions and inertial effects independently modify entrance effects.

3.4.1 Non-constancy of the permeability

Contrary to flows of more viscous oils, the hydrodynamic resistance is not constant during an experiment with the $M100$ oil. As can be seen in Fig. 3.20-a, the resistance strongly decreases while the cylinder empties. Thus the position of the front could not be fitted properly by an exponential, and we computed the resistance from measurements of positions and velocities (see section 3.2.3). The decrease of R_7 as a function of time corresponds to an increase of R_7 with the Reynolds number. Both are clearly seen in Fig. 3.20. Figure 3.20-b also reveals that inertial effects overwhelm hydrodynamic interaction effects. Indeed, the resistance rises by more than 300%, while interactions have an effect of 15% at most, for the membranes used here. Thus, this increase is the fact of inertial effects only. Moreover, the different curves corresponding to different interaction strengths are not ordered, which means that interaction effects cannot be detected in this plot. However, it is possible to disentangle these two effects, which we propose to do in the next subsection. In particular, we want to know if inertial effects and hydrodynamic interactions merely juxtapose, or if they combine in a mixed interaction-inertia coefficient.

3.4.2 Dependency of the access resistance with $\mathcal{R}_e$

As we mentioned in section 3.1.5, Jensen *et al.* rationalized the dependency with the Reynolds number of the access resistance of one single isolated pore. They stress that, for moderate Reynolds numbers exceeding a threshold $\mathcal{R}_e^t \lesssim 10$, an applied pressure drop not only counteracts the fluid viscosity but also accelerates the flow. The term $(\vec{v} \cdot \overrightarrow{\nabla})\vec{v}$ in Navier-Stokes equation begins to play a role. They proposed that the

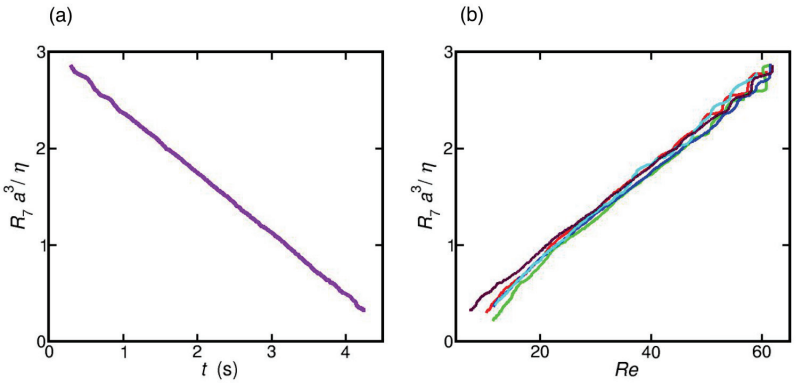

FIGURE 3.20: (a) Normalized hydrodynamic resistance of 7 pores ($a = 4$ mm, $L = 3\,a$) on the flow of $M100$ oil, during one draining. (b) Normalized resistance of different membranes with various interpore distances, as a function of the Reynolds number.

access resistance of a pore be

$$R^0_{\rm acc} = \frac{\eta}{a^3}\left(3 + \frac{\mathcal{R}_e - \mathcal{R}^t_e}{\pi}\right) = \frac{\eta}{a^3}\phi(\mathcal{R}_e), \tag{3.60}$$

which is successfully compared to old experimental data. Yet they stuck to the single pore case. Using the same notations, with ϕ a linear function of $\mathcal{R}_e$ and λ^i the interaction coefficient for the pore i, we aim at determining if the new correction factor for interacting pores with small inertial effects involves the sum of ϕ and λ^i (juxtaposition of both effects) or their product. We propose two alternative formulations of the access resistance of the pore i:

$$R^i_{\rm acc} = \frac{\eta}{a^3}\left(3(1-\lambda^i) + \frac{\mathcal{R}_e - \mathcal{R}^t_e}{C}\right) = \frac{\eta}{a^3}\left(\phi - 3\lambda^i\right), \tag{3.61}$$

which corresponds to the juxtaposition of inertial and interaction effects, or

$$R_{\text{acc}}^{i\prime} = \frac{\eta}{a^3}\left(3 + \frac{\mathcal{R}_e - \mathcal{R}_e^t}{C}\right) \times (1 - \lambda^i) = \frac{\eta}{a^3}\phi\left(1 - \lambda^i\right) \tag{3.62}$$

where inertial and interaction effects couple. Following Jensen *et al.*, we extracted the values of ϕ from the measured positions and velocities of the meniscus in the cylinder, under both hypothesis. We expect the values of ϕ not to depend on the interaction strength, as ϕ is defined to account for inertial effects only. We proceeded as follows. We saw that, when no parasitic resistance was perceptible, the global permeability of 7 pores on an hexagonal arrangement reads

$$K_7 = \sum_{i=1}^{7} K_1^i \tag{3.63}$$

$$= K_1^c + 6K_1^{ed} \tag{3.64}$$

with K_1^c the permeability of the central pore, and K_1^{ed} the permeability of a pore from the edge of the cluster. In the following, λ^c and λ^{ed} refer respectively to the central or a peripheral pore. We get

$$K_7 = \frac{1}{\frac{\eta}{a^3}(\phi - 3\lambda^c) + \frac{8\eta\ell}{\pi a^4}} + \frac{6}{\frac{\eta}{a^3}(\phi - 3\lambda^{ed}) + \frac{8\eta\ell}{\pi a^4}} \tag{3.65}$$

according to the first hypothesis, and

$$K_7' = \frac{1}{\frac{\eta}{a^3}\phi\,(1 - \lambda^{ed}) + \frac{8\eta\ell}{\pi a^4}} + \frac{6}{\frac{\eta}{a^3}\phi\,(1 - \lambda^{ed}) + \frac{8\eta\ell}{\pi a^4}} \tag{3.66}$$

according to the second one. Note that λ^c and λ^{ed} were proved to be accurate formulations of hydrodynamic interactions, in the case of creeping flow. We showed in the previous section that their theoretical

expression (3.45) accounts for experimental results. Furthermore, we saw in section 3.2.3 that the total hydrodynamic resistance of the cluster could be written as

$$R_7 = \mu g \left(\frac{1}{S_A} + \frac{1}{S_B} \right) \frac{z_B}{|\dot{z}_B|}. \tag{3.67}$$

Using Eq. (3.65) and (3.67) for the first hypothesis, or Eq. (3.66) and (3.67) for the second one, we get a second-order equation in ϕ which is easily solved, as all the coefficients can be calculated.

The values we obtain for ϕ are plotted in Fig. 3.21-a and b. The hypothesis of a coupling of inertial and interaction effects give values of ϕ which clearly depend on the interpore distance, *i.e.* on the intensity of hydrodynamic interactions, which is not relevant. On the other hand, we can see in Fig. 3.21-b that ϕ calculated under the hypothesis of a juxtaposition of these effects (3.61) does not depend on the interaction strength, whatever the Reynolds number. Thus, the correct definition of ϕ is the one given by Eq. (3.61), where hydrodynamic interactions and inertial effects simply add up. This evidences the absence of inertial interaction.

The linear fitting of the curves in Fig. 3.21-b results in $\phi = 3 + \dfrac{\mathcal{R}_e - \alpha}{\beta}$ with $\alpha = 4.2 \pm 1.3$ and $\beta = 3.22 \pm 0.09$. This is in full agreement with Johansen experimental results: $\phi = 3 + \dfrac{\mathcal{R}_e - \mathcal{R}_e^t}{\pi}$ with $\mathcal{R}_e^t = 4$ [72, 93]. In their article, Jensen *et al.* mentioned Bond work on cylindrical tubes of radius 1 mm and lenghts between 6 mm and 13 cm [92]. A thorough examination of their results suggests that the transition Reynolds number in this work is 6 ± 1, and not 10 as suggested by Jensen *et al.*. It seems that the 3 experimental results available to us are compatible. Contrary to Jensen *et al.*, we don't think that $\mathcal{R}_e^t$ should depend on the pore thickness. However, boundary conditions are likely

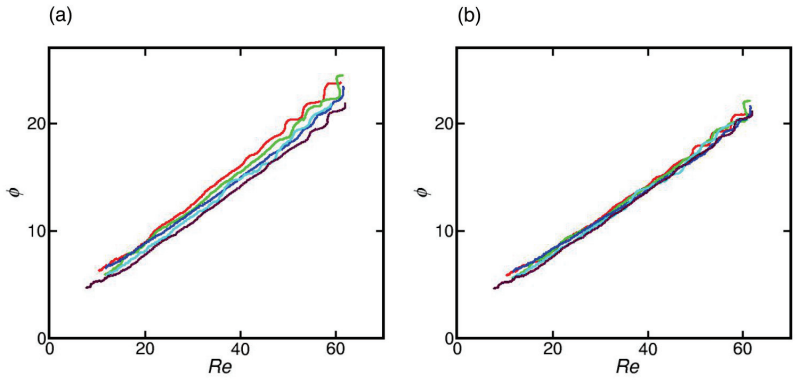

FIGURE 3.21: Parameter ϕ as a function of the Reynolds number. (a) ϕ under the hypothesis of a coupling between inertial and interaction effects (Eq. 3.62), (b) ϕ under the hypothesis of a simple juxtaposition of both effects (Eq. 3.61). From red to green, blue, cyan and maroon, the pores are spaced with an increasing distance L, from $L = 2.125\,a$ to $L = 3\,a$, *i.e.* interaction strength decreases.

to modify entrance effects, and thus the value of $\mathcal{R}_e^t$ and the slope of $\phi(\mathcal{R}_e)$. In this sense, Gravelle *et al.* recently showed that perfect slip enhanced access resistance at low $\mathcal{R}_e$ [66].

We summarize in Fig. 3.22 all the $\phi - \mathcal{R}_e$ curves from the same membranes, with $a = 4$ mm and various distances between pores L. For $\mathcal{R}_e < 3$, they all collapse on the constant curve $\phi = 3$, as expected for $\mathcal{R}_e < \mathcal{R}_e^t$. Data around $\mathcal{R}_e = 1$ were obtained with an intermediate viscosity, $\nu = 1000$ mm^2/s. For $\mathcal{R}_e > 10$, the adequacy with the model $\phi = 3 + \dfrac{\mathcal{R}_e - 4}{\pi}$ is excellent. It would be desirable to perform new experiments with a viscosity of 2000 mm^2/s, to access to Reynolds numbers between 0.1 and 12. Both regimes of high-viscosity and small inertial effects could be analyzed in a single drainage experiment, and the determination of the transition Reynolds number could maybe be more precise.

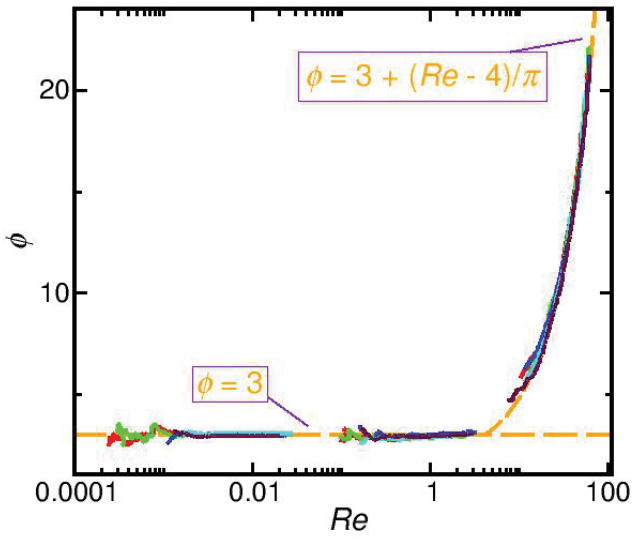

FIGURE 3.22: ϕ computed using Eq. 3.61, as a function of the Reynolds number in semi-log scale. The distinction between a regime of purely viscous flow ($\phi = 3$) and of viscous flow modified by small inertial effects (ϕ linear in $\mathcal{R}_e$) is clear.

To summarize briefly this section, we showed that hydrodynamic interactions and small inertial effects at moderate Reynolds numbers ($\mathcal{R}_e < 60$) simply juxtapose and do not couple. We stressed that even though the latter are "small" inertial effects, they surpass hydrodynamic interactions as soon as $\mathcal{R}_e > \mathcal{R}_e^t$. Finally, the access resistance of a pore i can be written as

$$R^i_{\text{acc}} = \frac{\eta}{a^3}\left(3(1-\lambda^i) + \frac{\mathcal{R}_e - \mathcal{R}_e^t}{C}\right) \tag{3.68}$$

with $\mathcal{R}_e^t = 4.2$ and $C = 3.22$. This is coherent with previous results on single pores.

3.5 Partial conclusion

In this chapter, we experimentally analyzed hydrodynamic interactions between pores, and found that they enhance the flow through a cluster of pores. Yet this enhancement remains a correction, the maximum increase in normalized permeability being $\approx 60\%$ for an infinite hexagonal array of pores brought in contact. This implies that hydrodynamic permeability keeps an extensive behavior when adding pores. For flows departing from a purely laminar behavior, we showed that hydrodynamic interactions and inertial effects do not influence each other but simply add up. Quantitatively, we found a transition Reynolds number of 4.2 between a purely laminar flow and inertial corrections. Our results thereby confirm and extend a recent proposition by Stone and co-workers [72]. We performed more complete calculation as a first-order description is not enough to describe quantitatively and accurately the interaction-driven permeability enhancement, and we explored different situations, such as the addition of pores.

Hydrodynamic interactions at low Reynolds numbers are in strong contrast with electrostatic interactions, which we studied in the first chapter. Indeed, electrostatic interactions decrease the intensity of ionic current. But their most dramatic characteristic is that they cause a sub-linear scaling of the conductance of an array of pores: for a growing number of pores $N \to \infty$, the contribution of one pore to the ionic conductance falls down to 0. Therefore, electrostatic interactions could modify the orders of magnitude of transport phenomena through pores, whereas hydrodynamic interactions are merely a correction factor. We also note that the scope of hydrodynamic interactions is much smaller than for electrostatic interactions, as hydrodynamic interactions scale mainly like $(a/L)^3$ whereas electrostatic ones scale like (a/L).

In the first two chapters of this thesis, we showed that there is no evidence that a massive parallelization of nanochannels could be an efficient way to scale up nanofluidic devices. Interactions at pore entrance can have dramatic effects on the scalings of transport properties, as it is the case for ionic transport. For fluidic transport, interactions have a rather positive impact, while not modifying the extensivity of the permeability.

Beyond the question of the scaling of hydrodynamic permeability, which is of first importance in filtration devices, we are interested in energy conversion which originates in electrokinetic effects. This is somewhat subtle, as electrokinetic conversion implies ionic transport, fluid transport, but also cross-coupling transports such as electro-osmosis and streaming current. There is no trivial way to predict the behavior of cross-coupling phenomena with respect to interactions at pore entrances. The aim of the next chapter will be to relate the global electrokinetic transport coefficients (such as ionic conductance and permeability but also streaming conductance) to their inner and access counterparts, in a general case. We will also tackle the case of particle diffusion, by analogy with ionic currents. Thanks to these theoretical formulations, we will be able to predict the scalings of electrokinetic energy conversions such as streaming current and diffusio-osmosis, for an assembly of interacting pores.

Chapter 4

Electrokinetic transport and energy conversion

Contents

In the two previous chapters, we studied the ionic and fluidic transport in nanopore arrays. Ionic conductance and hydrodynamic permeability have completely different scalings, the former scaling sub-linearly with the number of pores, while the latter keeps an extensive behavior with positive corrections. Apart from an extended knowledge and applications in filtration, these results constitute necessary building blocks to manage scaling-ups of energy conversion devices, based on electrokinetic transport phenomena. Yet, for now, we have no predicting tool for the energy conversion scaling, because we lack information on cross-coupling phenomena. In particular, we are interested in the ionic current stemming from an applied pressure drop (streaming current), and the ionic current stemming from a difference in ionic concentration between 2 reservoirs (diffusio-osmotic current). To access the scaling of these phenomena, we need a general matrix approach, which we develop in this chapter.

The main goal of this chapter is to determine the efficiency of energy conversion from electrokinetic transport phenomena, under the assumption of interacting pores. The formalism we develop to reach it will allow to tackle another question: how do cross-coupling phenomena affect the global ionic conductance and hydrodynamic permeability of the experimental systems previously studied ?

In this chapter, we will first carefully present the analogies between Fick diffusion and ionic conduction in nanopores. We present arguments in favor of a similar scaling of entrance effects for both phenomena. Such analogies must be handled with care, as fluidic transport does not obey the same rules. We next establish a general formulation of electrokinetic transport coefficients, from inner and access resistances. We will then

come back to the determination of ionic conductance and hydrodynamic permeability in the last 2 chapters, where we did not take cross-coupling phenomena into account. In fact, the results of the previous chapters are valid because of the dimensions of the pores, but they would not be for smaller nanopores. Finally, knowing the scaling of inner and access resistances with the size of the pore array, we will deduce the scaling of the global transport coefficients, in- and off-diagonal. We will be able to conclude on the produced power and the efficiency of energy conversion through streaming currents and diffusio-osmotic currents.

4.1 Analogies between transport phenomena

It is well-known since Adolf Fick's work that particle diffusion and electric conduction exhibit strong similarities. This is especially true for ion conduction and ion diffusion, as ions vector the transport in both cases. Yet, the driving forces differ: an electric potential drop ΔV in the first case, or a concentration difference $\Delta\rho$ in the second case. To conclude on the extent of the analogy, we investigate precisely the physical rules behind these two transport phenomena. We also compare them to fluidic transport which obeys different equations.

Our results are summed up in Table 4.1. Usually, the analogy between transport phenomena is built on the existence of driving force expressed as gradients of an intensive quantity, and a flowing quantity. This allows the definition of a resistance to the (electric, diffusive or fluid) flow. A deeper insight into the physics at stake shows that the existence of a linear relation between the driving force and the flowing quantity is a cornerstone for analogous behaviors. Ohm's law and Fick's law

transport type	conductive	diffusive	fluidic
Physical quantity representing the flow	$\vec{j}$	$\vec{j}_{\mathrm{d}}$	$\vec{v}$
Driving force	$V_1 - V_2$	$\rho_1 - \rho_2$	$P_1 - P_2$
Link between the driving force and the flow	$\vec{j} = -\kappa_{\mathrm{b}} \overrightarrow{\nabla} V$ Ohm's law	$\vec{j}_{\mathrm{d}} = -D \overrightarrow{\nabla} \rho$ Fick's law	$\eta \triangle \vec{v} = \overrightarrow{\nabla} P$ Stokes equation
Conservation equation	$\overrightarrow{\nabla} \cdot \vec{j} = 0$	$\overrightarrow{\nabla} \cdot \vec{j}_{\mathrm{d}} = 0$	$\overrightarrow{\nabla} \cdot \vec{v} = 0$
Laplacian equation	$\triangle V = 0$	$\triangle \rho = 0$	$\triangle \Omega = 0$
Boundary conditions	$\overrightarrow{t} \cdot \vec{j} = 0$, $\vec{n} \cdot \vec{j} = 0$	$\overrightarrow{t} \cdot \vec{j}_{\mathrm{d}} = 0$, $\vec{n} \cdot \vec{j} = 0$	$\overrightarrow{t} \cdot \vec{v} = 0$, $\vec{n} \cdot \vec{v} = 0$

TABLE 4.1: Analogies and differencies (in grey) between ionic conduction, particle diffusion and fluid advection.

represent such linear link, which does not exist for fluidic transport as evidenced in Table 4.1.

Under relevant hypothesis (quasi-stationary regimes for electric transport, incompressibility for fluidic transport), all transport phenomena under study exhibit similar conservation equations: the divergence of the flowing quantity is zero.

Coupled with Ohm's law and Fick's law, the conservation equation results in a Laplacian equation for the driving force quantity. For fluid flow, it is possible to define a harmonic function Ω, ressembling to a velocity potential, obeying a Laplacian equation, see [90]. Yet, this Laplacian equation does not have the same physical meaning as in ion conduction and diffusion, as Ω is not a driving force quantity.

Ion conduction and ion diffusion therefore exhibit similar governing equations. As for boundary conditions at the membrane surface, they are shared by all these three transport phenomena. The perpendicular component of the flowing quantity is zero, because there is no net flux

of ions toward the membrane, otherwise it would progressively charge or discharge like a condenser, which is not the case here. For fluidic transport, this result stems from the impermeability of the membrane. Moreover, there is no net lateral flow of ions or liquid at the membrane.

These considerations show that entrance effects behave alike for ionic conduction and ionic diffusion. On the contrary, fluidic transport does not obey the same equations. Hence it is no surprise that we found different behaviors for ionic entrance effects and hydrodynamic ones in chapters 2 and 3. Such assertion may be contradicted experimentally, if the above modelization is unsuitable. But if it is valid, then ionic conductive and diffusive transport have exactly the same bevior. Thus the access resistance to diffusive ion transport scales sub-extensively with the number of channels, as in conductive ion transport.

We now turn to a matrix rationalization of electrokinetic transport phenomena. We will build the global coefficients for direct phenomena (permeability, conductance) and cross-coupling phenomena (streaming current, electro-osmotic flow) from their inner and access counterparts which are our elementary bricks. To simplify the calculation, we exclude diffusive transport for now, assuming no gradient concentration between the reservoirs. We will come back to such situation in the last section, when dealing with diffusio-osmotic energy conversion.

4.2 General expression of electrokinetic transport coefficients

The aim of this section is to relate the global fluid flow, and ionic current, to these inner and access quantities. The novelty compared

to the previous chapters is that we will take cross-coupling phenomena into account, namely electro-osmosis velocity and streaming current.

We note quantities referring to the inner part of the channel (*e.g.* Poiseuille permeability) with a ^{i} superscript, the outer access region with a ^{a} superscript and no superscript for the total far field quantities. For clarity we use the notations K_h and K_e to refer to the hydrodynamic permeability and ionic conductance, instead of K and G used before. For the total transport we have

$$\begin{bmatrix} Q \\ I \end{bmatrix} = \begin{bmatrix} K_\mathrm{h} & \mu_\mathrm{EO} \\ \mu_\mathrm{EO} & K_\mathrm{e} \end{bmatrix} \begin{bmatrix} \Delta P \\ \Delta V \end{bmatrix} \tag{4.1}$$

where the symmetry results from Onsager reciprocity [95]. Our aim is to determine this 2x2 matrix coefficients, knowing the properties of the inner and access transport.

For the inner fields, the same symmetry is imposed:

$$\begin{bmatrix} Q^i \\ I^i \end{bmatrix} = \begin{bmatrix} K^i_\mathrm{h} & \mu^i_\mathrm{EO} \\ \mu^i_\mathrm{EO} & K^i_\mathrm{e} \end{bmatrix} \begin{bmatrix} \Delta P^i \\ \Delta V^i \end{bmatrix}. \tag{4.2}$$

As for the access region, we suppose that the transport matrix is diagonal, neglecting cross-over phenomena that could originate in the diffuse layer of the membrane itself (perpendicular to the channel) [96]. In this case we have, for one pore side,

$$\begin{bmatrix} Q^a \\ I^a \end{bmatrix} = \begin{bmatrix} K^a_\mathrm{h} & 0 \\ 0 & K^a_\mathrm{e} \end{bmatrix} \begin{bmatrix} \Delta P^a \\ \Delta V^a \end{bmatrix}. \tag{4.3}$$

We now consider the global conductance and electro-osmotic mobility that we obtain imposing $\Delta P = 0$. The conservation of flow rate and

ionic current write

$$Q = \mu_{\mathrm{EO}} \Delta V \tag{4.4}$$
$$= K_{\mathrm{h}}^{i} \Delta P^{i} + \mu_{\mathrm{EO}}^{i} \Delta V^{i} \tag{4.5}$$
$$= K_{\mathrm{h}}^{a} \Delta P^{a} \tag{4.6}$$

and

$$I = K_{\mathrm{e}} \Delta V \tag{4.7}$$
$$= \mu_{\mathrm{EO}}^{i} \Delta P^{i} + K_{\mathrm{e}}^{i} \Delta V^{i} \tag{4.8}$$
$$= K_{\mathrm{e}}^{a} \Delta V^{a}. \tag{4.9}$$

The total pressure drop and potential drop write as

$$\Delta P = \Delta P^{i} + 2\Delta P^{a} \tag{4.10}$$
$$\Delta V = \Delta V^{i} + 2\Delta V^{a}, \tag{4.11}$$

the factor 2 coming from the two channel ends. Using Eq. (4.4),(4.6) and (4.10) on the one hand, and Eq. (4.7),(4.9) and (4.11) on the other hand, we obtain

$$\Delta P^{i} = -2\frac{\mu_{\mathrm{EO}}}{K_{\mathrm{h}}^{a}} \Delta V \tag{4.12}$$
$$\Delta V^{i} = \left(1 - 2\frac{K_{\mathrm{e}}}{K_{\mathrm{e}}^{a}}\right) \Delta V. \tag{4.13}$$

Inserting Eq. (4.5) and (4.8) yields an equation system which can be easily solved as

$$K_{\mathrm{e}} = \frac{1 + 2q_{\mathrm{h}}(1-\alpha^{i})}{1 + 2(q_{\mathrm{e}} + q_{\mathrm{h}}) + 4q_{\mathrm{e}}q_{\mathrm{h}}(1-\alpha^{i})} K_{\mathrm{e}}^{i} \tag{4.14}$$
$$\mu_{\mathrm{EO}} = \frac{1}{1 + 2(q_{\mathrm{e}} + q_{\mathrm{h}}) + 4q_{\mathrm{e}}q_{\mathrm{h}}(1-\alpha^{i})} \mu_{\mathrm{EO}}^{i} \tag{4.15}$$

where we have used the reduced quantities $q_\mathrm{e} = K_\mathrm{e}^i/K_\mathrm{e}^a$, $q_\mathrm{h} = K_\mathrm{h}^i/K_\mathrm{h}^a$ and $\alpha^i = \mu_\mathrm{EO}^{i\,2}/(K_\mathrm{h}^i K_\mathrm{e}^i)$. A similar reasoning, imposing $\Delta V = 0$ leads to

$$K_\mathrm{h} = \frac{1 + 2q_\mathrm{e}(1-\alpha^i)}{1 + 2(q_\mathrm{e}+q_\mathrm{h}) + 4q_\mathrm{e}q_\mathrm{h}(1-\alpha^i)} K_\mathrm{h}^i \tag{4.16}$$

and to the same expression for μ_EO. Eq. (4.16) and (4.14) have exactly the same shape, with a switch in the role of q_e and q_h.

4.3 Influence of cross-coupling phenomena on ionic conductance and hydrodynamic permeability

4.3.1 Back to chapter 2: is a more accurate definition of K_e necessary ?

In chapter 2, we supposed that for an isolated pore the conductance was merely the result of the access resistance and the inner resistance in series. For one isolated pore, we wrote $K'_\mathrm{e} = (R_\mathrm{channel} + 2R_{access})^{-1}$ which can be rewritten as $K'_\mathrm{e} = \dfrac{K_\mathrm{e}^i K_\mathrm{e}^a}{K_\mathrm{e}^a + 2K_\mathrm{e}^i} = \dfrac{1}{1+2q_\mathrm{e}} K_\mathrm{e}^i$. K'_e visibly differs from what Eq. (4.14) predicts for K_e, taking into account electro-osmosis effect on the conductance via the coefficient α_i.

An applied voltage results in an ionic conductance and an electro-osmotic velocity, the latter being a first-order cross-coupling phenomena. The electro-osmotic solvent motion subsequently influences ion velocities, which could modify the ionic conductance compared to previous estimations.

We now give orders of magnitude showing that $K'_{\rm e}$ is a very good estimate of $K_{\rm e}$, in the nanopores we used. We can write

$$K_{\rm e} = K'_{\rm e}\frac{(1+2q_{\rm e})(1+2q_{\rm h}(1-\alpha^i))}{1+2(q_{\rm e}+q_{\rm h})+4q_{\rm e}q_{\rm h}(1-\alpha^i)} \tag{4.17}$$

$$= K'_{\rm e}\times\left(1-\frac{2q_{\rm h}\alpha^i}{1+2(q_{\rm e}+q_{\rm h})+4q_{\rm e}q_{\rm h}(1-\alpha^i)}\right). \tag{4.18}$$

To carry on the calculation, we need to evaluate $q_{\rm e}$, $q_{\rm h}$ and α^i.
We saw in the two previous chapters that

$$K^i_{\rm e} = \kappa_{\rm b}\frac{\pi a^2}{\ell}, \quad K^a_{\rm e} = 4\kappa_{\rm b}a \tag{4.19}$$

$$K^i_{\rm h} = \frac{\pi a^4}{8\eta\ell}, \quad K^a_{\rm h} = \frac{2a^3}{3\eta} \tag{4.20}$$

which yields

$$q_{\rm e} = \frac{\pi a}{4\ell} = 1.6, \quad q_{\rm h} = \frac{3\pi a}{16\ell} = 1.2 \tag{4.21}$$

using $a = 100$ nm $= 2\ell$ as in chapter 2. We compute $\mu^i_{\rm EO}$ in the case where $a \gg \lambda_{\rm D}$ the Debye length, which is valid throughout all this work as at most $\lambda_{\rm D} = 3$ nm for $c = 10^{-2}$ mol/L. Thus $\lambda_{\rm D} \ll a = 100$ nm in the nanopore experiments in chapter 2, and in the macroscopic experiments of chapter 3 this condition is obviously fulfilled. Classical formula (see *e.g.* [14]) give

$$\mu^i_{\rm EO} = \frac{-\epsilon\zeta}{\eta}\frac{\pi a^2}{\ell}, \quad \alpha^i = \frac{8(\epsilon\zeta)^2}{\eta\kappa_{\rm b}a^2} \leqslant 6.7\times10^{-3} \tag{4.22}$$

with $\epsilon \simeq 80\,\epsilon_0$ the permittivity of water ($\epsilon_0 = 8.85\times10^{-12}$ F/m is the vacuum permittivity) and ζ the zeta potential of the interface (potential at the slip plane). Typically for SiN surfaces $\zeta = -50$ mV. We have used the values $\eta \simeq 10^{-3}$ Pa.s, $\kappa_{\rm b} = 2{\rm e}^2\mu(c\times\mathcal{N}_A10^3)$ with $c \geqslant 10^{-2}$ mol/L and $\mu = D/(k_{\rm B}T)$ with $D \simeq 2\times10^{-9}$ m^2/s.

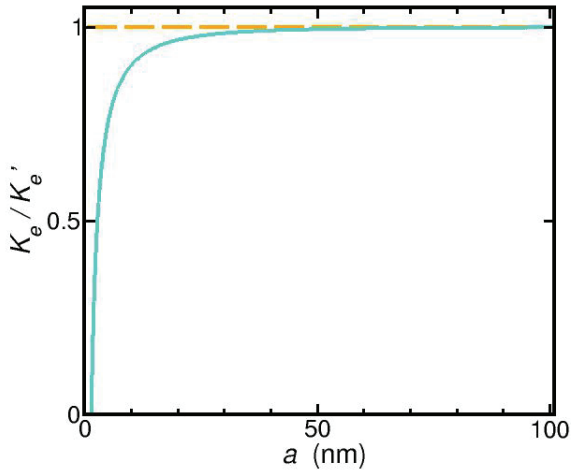

FIGURE 4.1: Ratio of the real ionic conductance over the estimated conductance, which we used in chapter 2, as a function of pore radius. We took a pore length $\ell = 50$ nm as in the experimental work of 2.

Numerically, Eq. (4.18) yields $K_\mathrm{e} = K'_\mathrm{e}(1 - 1 \times 10^{-3})$ for $a = 100$ nm. The formulation we used in chapter 2 is therefore valid. However, it would not be for smaller pores as can be seen in Fig. 4.1 where we computed K_e as a function of the pore radius. We used the expressions of q_e, q_h and α^i given in Eq. (4.21) and (4.22) and a salt concentration $c = 10^{-2}$ mol/L. For a pore size of 10 nm, we find a reduction of the ionic conductance of 10%.
Remember that our definition of μ^i_{EO} is valid for $a \gg \lambda_\mathrm{D}$. The sharp fall of K_e below $a = 10$ nm may not be accurate.

Note that in these calculation we leave out electro-osmosis originating on the membrane surface, but it is likely to be negligible [62].

4.3.2 Back to chapter 3: is a more accurate definition of K_h necessary ?

A rigorous calculation of the hydrodynamic permeability would also show that, in the case of macroscopic pores, the effect of streaming current of the flow is negligible. Indeed the coefficient α^i varies as $1/a^2$. α^i falls down to 10^{-11} when using 2 mm pores, while q_e and q_h keep the same order of magnitude. For fluid more viscous than water, as the silicon oil we used, α^i plunges even more. All in all, we are confident that cross-coupling phenomena have a negligible influence on the hydrodynamic permeability computed in chapter 3.

We now turn to the energy conversion question. We apply the above formalism to calculate the scaling of the output electrical power and efficiency of two different conversion processes. First, we investigate energy conversion through streaming currents, *i.e.* the ionic current in response to an applied pressure drop, due to the fact that the diffuse layer close to the surface has a global non-zero charge. We only consider 2D arrays of pores.

4.4 Energy conversion by streaming currents

We already saw in chapters 2 and 3 that, considering a number N of parallel channels, the inner conductance and permeability are additive. For an array of N pores, we have

$$K_\mathrm{e}^i \propto N \quad \text{and} \quad K_\mathrm{h}^i \propto N, \tag{4.23}$$

as Poiseuille and inner electrical resistances are independent, parallel resistances. The same holds for the streaming conductance μ_{EO}^{i}, like for all inner transport forms:

$$\mu_{\mathrm{EO}}^{i} \propto N. \tag{4.24}$$

For the access quantities, we have

$$K_{\mathrm{e}}^{a} \propto \sqrt{N} \quad \text{and} \quad K_{\mathrm{h}}^{a} \propto N, \tag{4.25}$$

according to our previous findings, for 2D arrays of N pores. For reduced quantities, this results in

$$q_{\mathrm{e}} \propto \sqrt{N} \quad \text{and} \quad q_{\mathrm{h}} \propto 1 \quad \text{and} \quad \alpha^{i} \propto 1. \tag{4.26}$$

Using Eq. (4.14) and (4.16), we get for the global coefficients

$$K_{\mathrm{e}}(= G_N) \propto \sqrt{N} \quad \text{and} \quad K_{\mathrm{h}}(= K_N) \propto N, \tag{4.27}$$

as we determined previously, in chapters 2 and 3, when we neglected cross-coupling phenomena. It is good news that these scalings are valid in any case. As for the global streaming conductance μ_{EO}, using Eq. (4.15) we get

$$\mu_{\mathrm{EO}} \propto \sqrt{N}. \tag{4.28}$$

It is worth noting that the electric response to an applied pressure field, and the flow caused by an applied electric field, behave like the electric conductance and not like the permeability.

We now turn to the energy conversion and consider a streaming current produced by an applied pressure drop. As pointed out by van der Heyden and coworkers [65], the nanochannel can be modelized by a current source in parallel with a resistance, see Fig. 4.2. Following the

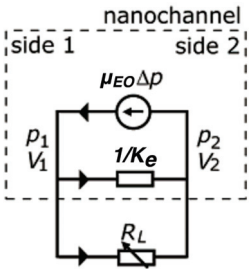

FIGURE 4.2: Equivalent electrical circuit for the energy conversion through streaming current. Adapted from [65].

work of the above cited authors, we connect this generator to a load resistance R_L. It is useful to express the potential drop as

$$\Delta V = V_2 - V_1 = -\frac{\mu_{\mathrm{EO}}\Delta P}{K_{\mathrm{e}} + 1/R_L}. \tag{4.29}$$

We use the reduced quantities

$$\alpha = \frac{\mu_{\mathrm{EO}}^2}{K_{\mathrm{e}}K_{\mathrm{h}}} \quad \text{and} \quad \Theta = K_{\mathrm{e}}R_L. \tag{4.30}$$

Using Eq. (4.29), the output power $\Delta V^2/R_L$ and the input mechanical power $Q\Delta P$ can be expressed as

$$\frac{\Delta V^2}{R_L} = K_{\mathrm{h}}\Delta P^2 \frac{\alpha\Theta}{(1+\Theta)^2} \quad \text{and} \quad Q\Delta P = K_{\mathrm{h}}\Delta P^2 \left(1 - \frac{\alpha}{1+1/\Theta}\right). \tag{4.31}$$

Note that the input power depends on the load resistance, because of cross-coupling phenomena.

The output power exhibits a maximum for a given ΔP for $\Theta = 1$ (impedance matching situation). In that case,

$$\left.\frac{\Delta V^2}{R_L}\right|_{max} = \frac{K_{\mathrm{h}}\Delta P^2\alpha}{4} \quad \left(= \frac{(\mu_{\mathrm{EO}}\Delta P)^2}{4K_{\mathrm{e}}} = \frac{I_{\mathrm{streaming}}^2}{4K_{\mathrm{e}}}\right). \tag{4.32}$$

The scalings of the global transport coefficients give $\alpha \propto 1/\sqrt{N}$ and thus

$$\left.\frac{\Delta V^2}{R_L}\right|_{\mathrm{Pmax}} \propto \sqrt{N}. \tag{4.33}$$

The electrical power produced thus increases with the number of interacting channels. However, the required input power $Q\Delta P$, increases even faster than the output power, according to

$$Q\Delta P_{\mathrm{Pmax}} = K_{\mathrm{h}}\Delta P^2 \left(1 - \frac{\alpha}{2}\right) \propto N. \tag{4.34}$$

Globally, the conversion efficiency $\mathcal{E}$, defined as the ratio of the output power to the input power, **decreases** as $1/\sqrt{N}$.

The same computation can be done for the maximum efficiency, which does not occur for $\Theta = 1$ but for a bigger load: $\Theta = 1/\sqrt{1-\alpha}$. It can be shown that

$$\mathcal{E}_{\max} = \frac{\alpha}{\alpha + 2(\sqrt{1-\alpha} + 1 - \alpha)} \underset{N\to\infty}{\sim} \frac{\alpha}{2} \propto 1/\sqrt{N}. \tag{4.35}$$

Interactions at pore entrances have therefore a major and potentially detrimental effects on single nanochannel performance when scaling up. Experimental ways have to be found to bypass these interactions. In other words, cut-offs are needed to limit the range of electrostatic interactions at pore entrances. A way to do so could be to bring the electrodes closer to the membrane, or even to spray deposite them directly on the membrane (see for example [97]). This is expected to affect strongly the field lines at pore entrances. Finite-element simulations could help to predict the behavior of transport phenomena in this situation.

The above result requires pushing the analysis further, to determine

which experimental refinements could preserve as much of single channel qualities.

4.5 Energy conversion by diffusio-osmosis

Diffusio-osmosis refers to the flow of solvent in a channel linking two reservoirs with different salt concentrations. This effect takes place in the Debye layer, which drags the whole fluid by viscosity. As the Debye layer has a net electric charge, such flows lead an electric current (see section **??** page **??**). Diffusio-osmosis can thus be envisioned as an alternative path for energy harvesting under salt concentration gradients [15]. As for streaming currents, the output power is an electric one, but the input power is of chemical nature.

As diffusio-osmosis involves diffusion, flows and ionic currents altogether, the matrixes we have to consider are now 3x3:

$$\begin{bmatrix} Q \\ I \\ J \end{bmatrix} = \begin{bmatrix} K_\mathrm{h} & \mu_\mathrm{EO} & B \\ \mu_\mathrm{EO} & K_\mathrm{e} & \mu_\mathrm{DO} \\ B & \mu_\mathrm{DO} & K_\mathrm{d} \end{bmatrix} \begin{bmatrix} \Delta P \\ \Delta V \\ \Delta \rho \end{bmatrix} \tag{4.36}$$

with

$$J = J^\mathrm{tot} - \rho^0 Q = \iint \vec{j_d} \cdot \overrightarrow{\mathrm{d}S} \tag{4.37}$$

the diffusive part of the flux of salt. J^tot is the total salt flux stemming from both diffusion (J) and convection ($\rho^0 Q$). ρ^0 is the average salt concentration.

The cross coefficients are now written μ_EO, B and μ_DO. The coefficients of interest in energy conversion under salt concentration gradients are μ_DO and K_e. Note that Onsager symmetry still applies. For inner and access transport, the matrixes are similar to (4.2) and (4.3) but 3x3. It

can be shown that the global transport coefficients are given by

$$\begin{bmatrix} B \\ \mu_{\mathrm{DO}} \\ K_{\mathrm{d}} \end{bmatrix} = M^{-1} \begin{bmatrix} B^i \\ \mu^i_{\mathrm{DO}} \\ K^i_{\mathrm{d}} \end{bmatrix}, \quad \begin{bmatrix} \mu_{\mathrm{EO}} \\ K_{\mathrm{e}} \\ \mu_{\mathrm{DO}} \end{bmatrix} = M^{-1} \begin{bmatrix} \mu^i_{\mathrm{EO}} \\ K^i_{\mathrm{e}} \\ \mu^i_{\mathrm{DO}} \end{bmatrix}, \quad \begin{bmatrix} K_{\mathrm{h}} \\ \mu_{\mathrm{EO}} \\ B \end{bmatrix} = M^{-1} \begin{bmatrix} K^i_{\mathrm{h}} \\ \mu^i_{\mathrm{EO}} \\ B^i \end{bmatrix}, \tag{4.38}$$

where M^{-1} is the inverse of

$$M = \begin{bmatrix} 1 + 2\frac{K^i_{\mathrm{h}}}{K^a_{\mathrm{h}}} & 2\frac{\mu^i_{\mathrm{EO}}}{K^a_{\mathrm{e}}} & 2\frac{B^i}{K^a_{\mathrm{d}}} \\ 2\frac{\mu^i_{\mathrm{EO}}}{K^a_{\mathrm{h}}} & 1 + 2\frac{K^i_{\mathrm{e}}}{K^a_{\mathrm{e}}} & 2\frac{\mu^i_{\mathrm{DO}}}{K^a_{\mathrm{d}}} \\ 2\frac{B^i}{K^a_{\mathrm{h}}} & 2\frac{\mu^i_{\mathrm{DO}}}{K^a_{\mathrm{e}}} & 1 + 2\frac{K^i_{\mathrm{d}}}{K^a_{\mathrm{d}}} \end{bmatrix}. \tag{4.39}$$

M^{-1} is given by $M^{-1} = \dfrac{1}{\det M} \operatorname{adj} M$, with $\operatorname{adj} M$ the adjugate matrix. We get, after a few simplifications

$$\mu_{DO} = \frac{-2\mu^i_{EO} B^i + \mu^i_{DO}(K^a_{\mathrm{h}} + 2K^i_{\mathrm{h}})}{K^a_{\mathrm{h}} \times \det M}. \tag{4.40}$$

This results has to be analyzed within a given experimental condition of mixing.

4.5.1 Absence of mixing

As we said in section 4.1, diffusive ion transport is expected to obey similar laws as conductive ion transport. Therefore the access coefficient for diffusive transport K^a_{d} is expected to follow $K^a_{\mathrm{d}} \propto \sqrt{N}$ like K^a_{e}.
After a few lines of calculation, it can be shown that in this case $\det M \propto N$. We get, for the transport coefficients, $K_{\mathrm{e}} \propto \sqrt{N}$ as expected,

and $\mu_{\mathrm{DO}} \propto 1$ which is worse than K_{e} and K_{d}, and very unexpected. The maximum output power is given by [15]

$$\mathcal{P}^{\mathrm{out}}_{\mathrm{DO,\,max}} = \frac{I_{DO}^2}{4K_{\mathrm{e}}} = \frac{(C\Delta\rho)^2}{4K_{\mathrm{e}}}, \tag{4.41}$$

which scales very unfavourably like $1/\sqrt{N}$.
Yet, it is possible to circumvent part of this adverse scaling by using convective mixing in the reservoirs. The aim of mixing is to bypass interactions in diffusive entrance effects, to reach an extensive diffusive flux.

It is also possible to compute scalings for the input chemical power and the efficiency of the process. However, there is no real economic cost in filling two reservoirs with different salt concentrations. These scalings can be used for comparison with different energy conversion methods, such as pressure-retarded osmosis or reverse electrodialysis which were presented in chapter 1.
The input chemical power can be approximated by

$$\mathcal{P}^{\mathrm{in}}_{\mathrm{DO}} \approx k_{\mathrm{B}}T\Delta\rho\, Q = k_{\mathrm{B}}T \times B(\Delta\rho)^2. \tag{4.42}$$

A more proper expression of the input power could be drawn from Gibbs free energy of mixing, following Kim and co-workers [98].
The same type of calculation as above leads to $B \propto \sqrt{N}$, and the global efficiency of the energy conversion thus scales like

$$\mathcal{E} \propto \frac{C^2}{BK_{\mathrm{e}}} \propto 1/N. \tag{4.43}$$

4.5.2 Case of convective mixing in the reservoirs

The effect of mixing on diffusive entrance effects is not certain yet. Two cases can be envisioned: either mixing remove interactions in which case $K_{\mathrm{d}}^{a} \propto N$, or mixing totally cancels access diffusive resistance and $K_{\mathrm{d}}^{a} \to \infty$. Still, $K_{\mathrm{e}}^{a} \propto \sqrt{N}$.
In fact, the two cases mentioned above lead to the same result: $\det M \propto \sqrt{N}$ which yields

$$\mu_{\mathrm{DO}} \propto \sqrt{N} \quad \text{and} \quad \mathcal{P}_{\mathrm{DO,\,max}} \propto \sqrt{N}. \tag{4.44}$$

Moreover, in this case $B \propto N$ so that

$$\mathcal{E}^{\mathrm{mix}} \propto 1/\sqrt{N}. \tag{4.45}$$

We summarize our results in Table 4.2. None of the two studied processes

process	streaming current	diffusio-osmosis	diffusio-osmosis with mixing
$\mathcal{P}^{\mathrm{out}}$	$\sqrt{N}$	$1/\sqrt{N}$	$\sqrt{N}$
$\mathcal{E}$	$1/\sqrt{N}$	$(1/N)$	$(1/\sqrt{N})$

TABLE 4.2: Summary of the results for energy conversion through streaming currents and diffusio-osmosis, N being the number of pores. The efficiency of the diffusio-osmosis process is given in brackets as it has no economic influence.

benefit from interactions at pores entrance, neither streaming current, nor diffusio-osmosis. Seemingly, interactions have to be avoided to reach a better efficiency.

4.6 Partial conclusion

We proposed in this chapter a general formalism to describe electrokinetic transport phenomena, taking into account entrance effects and cross-coupling coefficients. Using the scaling for hydrodynamic and electric entrance effects determined in the previous chapters, we predicted that the efficiency of energy conversion using electrokinetic phenomena scales at best like $1/\sqrt{N}$, N being the number of channels in the membrane.

This scaling is highly unfavorable, but several elements must temper our conclusion. First, the hypothesis that diffusive entrance effects scale as electrical ones must be checked. Moreover, we also have to consider the real scope of electrostatic interactions at channel entrances. The finite size of electrodes and the finite distance at which they are from the membrane could possibly limit the interaction range. It would be of interest to test numerically the case where electrodes are at a distance from the membrane which compares to the pore radius. The ultimate situation would be to graft electrodes directly on the membrane.

Altogether, entrance effects across membranes exhibit subtle and counter-intuitive features, which should be handled with care when tackling nanofluidic properties scaling-up. Calculations led in the case of infinite hemispherical electrodes indicate that interactions at channel entrances strongly decrease the efficiency of energy conversion processes. Yet, tuning of the electrode size and position could help reducing the strength and scope of interactions.

Chapter 5

Liquid osmosis through a gas phase: a numerical study

Contents

5.1 Osmosis membranes in desalination

5.1.1 Requirements for desalination osmosis membranes

In 1960, Loeb and Sourirajan exhibited the first desalination membrane, paving the way for reverse osmosis to develop [99]. Much progress has been accomplished since then, and reverse osmosis is now the leading desalination technology. Its main advantage is to have the lowest energy consumption among all the current industrial processes [29].

Designed to let only water molecules flow, but not ions, perfect desalination membranes should exhibit both an excellent selectivity and a high water permeability. Yet, these are conflicting requirements, because selectivity and permeability are mainly controlled by a same parameter, pore size, which influences them in an opposite way. Because of

their hydration shell, ions have a larger effective diameter than water molecules and are prevented from flowing to the membrane by steric repulsion. Hence, selectivity requires small-pore membranes. On the contrary, water flow increases rapidly along with pore radius a, as a^4 for a Poiseuille flow.

As selectivity is a necessary condition for desalinating, it was fulfilled from the first dedicated membranes. In the 1970s, salt rejection attained 95% and exceeded 99% by 1987 [100]. So far, reverse osmosis membrane pore size should be less than 0.6 nm to reach a 99% rejection rate [30, 101]. Wider pores of 1-2 nm can achieve decent ion rejection if they are functionalized with ionic groups, thanks to an electrostatic Donnan-type rejection mechanism [102, 103]. However, this mechanism only proves efficient at low ionic concentration and is very sensitive to ion valence effects, not providing universal ion rejection.

Permeability has regularly increased since the beginning of reverse osmosis, reaching now 0.3 $m^3/(m^{-2}{\cdot}MPa{\cdot}day)$ for seawater [29]. Yet, there is space to improve water flow which is the limiting factor of desalination efficiency. Carbon-nanotube (CNT) membranes are a potential alternative to current polymeric membranes. These structures foster hope because water was shown to experience great slippage inside of them [68, 69, 104]. Early experimental results were rationalized by numerical investigations, showing that the super fast water flows in CNTs originate in a curvature-dependent friction coefficient [31]. However, even if flow rates *inside of* CNTs outreach flows in traditionnal materials, they are still limitated by entrance effects (described in chapter 3). Access resistance scales like $1/a^3$, thereby the smaller the pores, the more stringent the limitation to fluid flows [87, 88]. Moreover, CNT membranes are very difficult to produce with good control. There is a need for technological breakthrough to manage to produce these at a large scale and reasonable cost.

We now present a new method susceptible to provide an alternative solution to the low permeate flow and high CNT-membrane cost.

5.1.2 A gas bubble as an osmosis semi-permeable membrane

The presently studied method releases the nanometric size constraint by forcing water into a gas phase inside the membrane [5–7]. Ions are retained in the liquid phase because of the very high energetic cost necessary to strip them from their solvation shell. The physical mechanism preventing ions from flowing into the membrane is thus very different from traditional osmotic membranes. It is actually shared by distillation methods, such as multi-stage flash distillation (MSF), multi-effect distillations (MED) and membrane distillation which we presented in chapter 1. In these methods, thermal energy and lowering pressures allow water to vaporize. Whereas MSF and MED work with large volumes of fluid at a time, membrane distillation is another nanoporous-membrane-based method, where water vapor from the brine reservoir reaches and passes through a hydrophobic porous membrane, before condensing in the pure water reservoir. Even though membrane distillation has a lower energetic cost than MSF and MED, it suffers from low permeate flow rates [35] and thermal losses [5]. Nowadays, membrane distillation is in a state of relative indifference, both from the industry and the academia.

Designed and experimentally studied in Karnik's team at Massachusetts Institute of Technology, liquid osmosis through a gas phase borrows from forward and reverse osmosis, and membrane distillation. The former methods were presented in chapter 1 too. As in membrane distillation, brine and pure water are separated by a porous hydrophobic

membrane, where water vaporizes while transiting from one side to the other. However the process is not thermally driven (although rising the temperature could enhance the flow), but osmotically driven if forward osmosis is considered, or mechanically driven as in reverse osmosis. Under a salt-concentration difference between the two sides of the membrane, water spontaneously transits through the gas phase from the low- to the high-concentration side. Instead, if an applied mechanical pressure compensates and overcomes the osmotic pressure, water flows from the high- to the low-concentration side. Experimentally, such membranes comprising nanobubbles with typical diameters of 70 nm and lengths of a few microns have been shown to be successful under forward osmosis [6]. Even if the level of hydrophobicity required necessitates some chemical technicality, these nanotube dimensions allow an easy scaling-up.

The present chapter will be organized as follows. First, we present the physics governing the osmotic process through a gas phase. The established equations will allow for a direct comparison with reverse osmosis performance. The limits of the method will also be considered. Then, we will characterize the transport mechanism under forward osmosis, with molecular dynamics simulations of a simple Lennard-Jones fluid. We then investigate the conditions under which the gas bubble is impermeable to salt by measuring the energy-barrier an ion has to overcome to pass through the hydrophobic tube.

5.2 Physical mechanism of osmotic permeation through a gas phase

5.2.1 Driving force

Gas flow within the membrane is driven by a partial pressure drop between the two interfaces, originating from the (mechanical or osmotic) pressure drop between the two liquid phases [5, 7]. This will be evidenced by the following calculation.

We consider the situation depicted in Fig. 5.1. The left reservoir, referred to as the A side, contains salty water, while the right reservoir (B side) contains pure water. Like in reverse osmosis, a piston adds a mechanical pressure on the A side aimed at counterbalancing the osmotic pressure between the two sides. Thus, the A-interface meniscus is more curved than the B one. At each interface, the chemical potential of water in the liquid and gas phases equilibrates. Using subscripts for the reservoir $_A$ or $_B$, and superscripts $^\ell$ or ^{v} for the liquid or gas phase, we get for the B interface

$$\mu_B^\ell = \mu_B^v \tag{5.1}$$

$$\mu_{\text{sat}} + V_m(P_B - P_{\text{sat}}^v) = \mu_{\text{sat}} + RT \ln\left(P_B^v / P_{\text{sat}}^v\right) \tag{5.2}$$

where μ_{sat} and P_{sat}^v are the equilibrium chemical potential and equilibrium vapor pressure, defined when pure liquid water is in equilibrium with pure vapor water. V_m is the liquid water molar volume, P_B the pressure in the B liquid reservoir, R the gas constant, T the temperature and P_B^v the water partial pressure at the B interface.

Moreover, Young-Laplace equation describes the mechanical equilibrium of the interface, linking the pressure in the liquid P_B to the pressure in

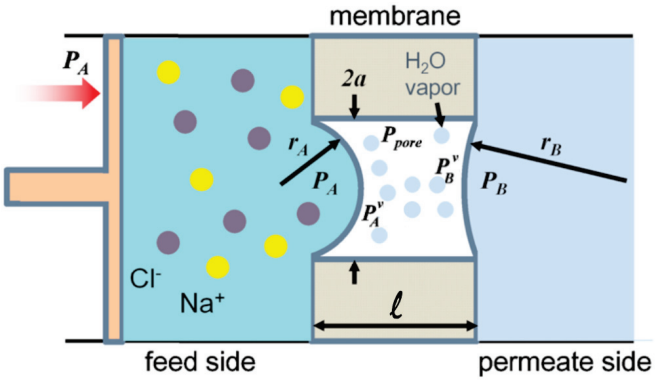

FIGURE 5.1: Schematic diagram of a hydrophobic nanochannel with liquid-vapor interfaces on either sides. The applied pressure on the A side is greater than the osmotic pressure, resulting in gas transport through the bubble. P_{pore} is the total pressure of the gas phase, while $P_{\text{vap,A/B}}$ are the water partial pressures at both interfaces. Reproduced from [5].

the gas P_{pore} according to

$$P_B = P_{\text{pore}} + \frac{2\gamma_{lv}}{r_B}. \tag{5.3}$$

We stress that P_{pore} is the total pressure of the gas phase, which contains not only water vapor but also air. γ_{lv} is the water surface tension, assumed to be identical for salted and pure water, and r_B is the curvature radius of the B interface. Eq. (5.2) and (5.3) yield

$$\ln\left(\frac{P_B^v}{P_{\text{sat}}^v}\right) = \frac{V_m}{RT}\left(P_{\text{pore}} - P_{\text{sat}}^v + \frac{2\gamma_{lv}}{r_B}\right). \tag{5.4}$$

As $P_{\text{pore}} - P^v_{\text{sat}} \ll \dfrac{2\gamma_{lv}}{r_B}$, we get

$$\ln\left(\frac{P^v_B}{P^v_{\text{sat}}}\right) = \frac{V_m}{RT}\left(\frac{2\gamma_{lv}}{r_B}\right) \tag{5.5}$$

$$= \frac{V_m}{RT}\left(P_B - P_{\text{pore}}\right). \tag{5.6}$$

The partial pressure at the B interface follows as

$$P^v_B = P^v_{\text{sat}} \exp\left(\frac{\Delta P_B\, V_m}{RT}\right) \approx P^v_{\text{sat}}\left(1 + \frac{\Delta P_B\, V_m}{RT}\right). \tag{5.7}$$

where $\Delta P_B = P_B - P_{\text{pore}}$ is the pressure difference across the B meniscus.

The same procedure at the A interface gives

$$\mu^\ell_A = \mu^v_A \tag{5.8}$$

$$\mu_{\text{sat}} + V_m(P_A - P^v_{\text{sat}}) + RT\ln x_w = \mu_{\text{sat}} + RT\ln\left(P^v_A/P^v_{\text{sat}}\right) \tag{5.9}$$

where x_w is the water mole fraction in the liquid phase. Considering

$$P_A = P_{\text{pore}} + \frac{2\gamma_{lv}}{r_A} \tag{5.10}$$

and $P_{\text{pore}} - P^v_{\text{sat}} \ll \dfrac{2\gamma_{lv}}{r_A}$, Eq. (5.9) results in

$$P^v_A = P^v_{\text{sat}} \exp\left(\frac{\Delta P_A\, V_m}{RT}\right) x_w \approx P^v_{\text{sat}}\, x_w \left(1 + \frac{\Delta P_A\, V_m}{RT}\right). \tag{5.11}$$

with $\Delta P_A = P_A - P_{\text{pore}}$.

We now follow Lee & Karnik [5] to establish the transport driving force across the pore:

$$P_A^v - P_B^v = P_{\text{sat}}^v \left[\left(1 + \frac{\Delta P_A \, V_m}{RT} \right) (x_w - 1) + \frac{\Delta P_A \, V_m}{RT} - \frac{\Delta P_B \, V_m}{RT} \right]. \tag{5.12}$$

Introducing the osmotic pressure as

$$\Delta\Pi = k_{\text{B}} T \rho_{\text{salt}} = \frac{RT}{V_m} x_{\text{salt}} = \frac{RT}{V_m}(1 - x_w), \tag{5.13}$$

Eq. (5.12) can be rewritten according to

$$P_A^v - P_B^v = P_{\text{sat}}^v \left[\frac{(\Delta P - \Delta\Pi) V_m}{RT} - \frac{\Delta P_A \, V_m}{RT} \frac{\Delta\Pi \, V_m}{RT} \right] \tag{5.14}$$

with $\Delta P = \Delta P_A - \Delta P_B = P_A - P_B$. The second term in the parenthesis being much smaller than the first one, we finally obtain

$$P_A^v - P_B^v = \frac{P_{\text{sat}}^v V_m}{RT} (\Delta P - \Delta\Pi) = \frac{\rho_{\text{sat}}^v}{\rho^l} (\Delta P - \Delta\Pi) \tag{5.15}$$

where ρ_{sat}^v and ρ^l are the number densities of the equilibrium vapor and of the liquid phase respectively.

5.2.2 Transport through a gas phase

Denoting $\phi_{A,B/B,A}$ the probability that a molecule emitted by evaporation in A (resp. B) condenses on the other meniscus B (resp. A), and $\dot{N}_{\text{e,A/B}}$ the evaporation rate at the A (resp. B) interface, the net flux rate (in s^{-1}) across the nanochannel is

$$\dot{N} = \phi_{A,B} \dot{N}_{\text{e,A}} - \phi_{B,A} \dot{N}_{\text{e,B}}. \tag{5.16}$$

For each meniscus to be at equilibrium, the evaporation rate $\dot{N}_e$ is equal to the condensation rate $\dot{N}_c$, given by [5, 105]

$$\dot{N}_{\mathrm{c,A/B}} = \sigma \times \frac{1}{4}\,\bar{v}\,\rho^v_{A/B} \times \pi a^2 \tag{5.17}$$

where σ is the condensation coefficient, *i.e.* the probability that an incident gas molecule condenses at the meniscus, $\bar{v}$ the mean of the magnitude of the water-molecule thermal velocity and $\rho^v_{A/B}$ the water number density in the gas phase, at meniscus A or B respectively. Using $\bar{v} = \sqrt{\dfrac{8k_{\mathrm{B}}T}{\pi m_w}}$ (with m_w the mass of a water molecule) and $\rho^v = \dfrac{P^v}{k_{\mathrm{B}}T}$, we obtain

$$\dot{N}_{\mathrm{c,A/B}} = \sigma \times \sqrt{\frac{k_{\mathrm{B}}T}{2\pi m_w}}\,\frac{P^v_{A/B}}{k_{\mathrm{B}}T} \times \pi a^2. \tag{5.18}$$

The net flux through the bubble becomes

$$\dot{N} = \sigma\,(\pi a^2)\,\sqrt{\frac{1}{2\pi m_w k_{\mathrm{B}}T}}\,(\phi_{A,B}\,P^v_A - \phi_{B,A}\,P^v_B). \tag{5.19}$$

To compute $\phi_{A,B}$, it is necessary to rely on a diffusion model. For nanometer pores, Knudsen diffusion is relevant, as the mean free path for water vapor at ambiant temperature is about 1 μm, thus exceeding the pore radius. However, Knudsen diffusion coefficient is defined in the limit of an infinite pore length. Lee & Karnik thus established a general model by considering all possible ways for a molecule emitted in A to condense at either A of B meniscus [5]. They found that

$$\phi_{A,B} = \phi_{B,A} = \frac{\eta}{2\eta(1-\sigma)+\sigma} \tag{5.20}$$

where η is the transmission coefficient, accounting for the probability that a molecule evaporated at one side reaches the other side. Whereas σ is expected to be constant but unknown, as the values reported in the literature vary from 0.01 to 1 (see [5]), η was calculated as a

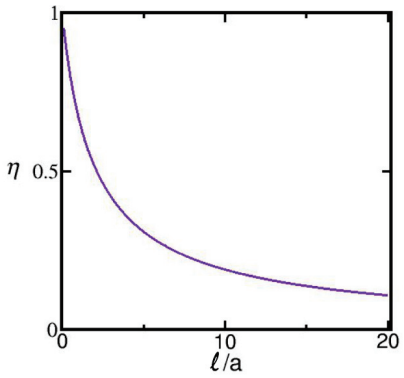

FIGURE 5.2: Transmission coefficient of a molecule across a cylindrical nanochannel of length ℓ and radius a, using the expression given by Berman [106]. In this work we use aspect ratio ℓ/a between 1 and 12.

function of the pore aspect ratio $AR = \ell/a$, under the diffusive scattering assumption [106]. It is given by

$$\eta = 1 + \frac{AR^2}{4} - \frac{AR}{4}(AR^2+4)^{1/2} - \frac{\left[(8-AR^2)(AR^2+4) + AR^3 - 16\right]^2}{72\,AR(AR^2+4)^{1/2} - 288\ln\left(\frac{AR}{2} + \left(\frac{AR^2}{4}+1\right)^{1/2}\right)} \tag{5.21}$$

which is plotted in Fig. 5.2. Formula (5.21) is derived under the hypothesis that only water molecules are present in the gas phase. It is possible to account for the effects of air molecules using a dusty-gas model [6], which yields a modified transmission probability. Although such effects can be substantial in experimental systems, we do not consider them in the following; numerical systems will not exhibit air molecules.

All in all, the water flux across the nanochannel, from the draw side to the permeate side, is expected to obey

$$\dot{N} = \frac{\sigma\eta}{2\eta(1-\sigma)+\sigma} \times \pi a^2 \times \sqrt{\frac{1}{2\pi m_w k_\mathrm{B} T}} \frac{\rho^v_\mathrm{sat}}{\rho^l} (\Delta P - \Delta\Pi) \quad (5.22)$$

It is of interest to check the validity of Eq. (5.22) with numerical methods, which allow an easy tuning of the various physical quantities. This study will be undertaken in section 5.3. If one considers a nanoporous membrane with many nanobubbles in parallel, it is useful to consider the mass rate through the membrane, in g/(m$^2\cdot$ s), which we define as

$$\dot{m} = \Phi\, m_w \frac{\dot{N}}{\pi a^2} \quad (5.23)$$

where Φ is the membrane porosity (void fraction), and $\dot{N}$ the flux rate in s^{-1} through one single nanochannel, derived in Eq. (5.22). $\dot{m}$ writes

$$\dot{m} = \Phi \times \frac{\sigma\eta}{2\eta(1-\sigma)+\sigma} \times \sqrt{\frac{m_w}{2\pi k_\mathrm{B} T}} \frac{\rho^v_\mathrm{sat}}{\rho^l} (\Delta P - \Delta\Pi). \quad (5.24)$$

Now, we turn to the inherent limitations of osmosis through a gas phase, namely a maximal pore radius and minimal aspect ratio.

5.2.3 Limits of the method

To maximize concentration gradients and hence optimize permeate flow, the length of nanochannels tends to be reduced. What is more, as the present method waives the subnanometric imperative, it is tempting to increase the pore radius. However, the stability of the gas bubble restricts both pore radius and length. Both criteria affect the mass flux derived in 5.24, because they translate in an upper bound for the

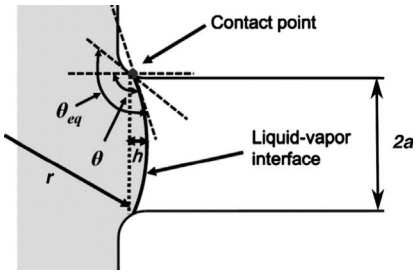

FIGURE 5.3: Detailed configuration of liquid-vapor interface. θ_{eq} denotes equilibrium contact angle satisfying Young's relation and θ denotes the angle between a line tangential to interface and pore axis, which satisfies mechanical force equilibrium. Reproduced from [5].

transmission coefficient η. Note that $\dfrac{\sigma\eta}{2\eta(1-\sigma)+\sigma}$ is an increasing function of η, whatever σ.

• *Maximum pore radius*

The condition on the pore radius originates in the mechanical pressure drop a liquid-gas interface can sustain. In the proposed configuration, depicted in Fig. 5.3, it is given by the Laplace-Washburn equation [5, 107]

$$\Delta P_{A\,\max} = P_A - P_{\text{pore}} = -\frac{2\gamma_{lv}\cos\theta_{\text{eq}}}{a}, \tag{5.25}$$

where θ_{eq} is the static contact angle, satisfying Young's relation

$$\gamma_{sl} - \gamma_{sv} + \gamma_{lv}\cos\theta_{\text{eq}} = 0. \tag{5.26}$$

Eq. (5.25) can alternatively be seen as the maximum radius allowing the pore to resist wetting,

$$a_{\max} = -\frac{2\gamma_{lv}\cos\theta_{\text{eq}}}{\Delta P_A}. \tag{5.27}$$

Under forward osmosis, the channel radius could be as high as 1.4 μm for a perfectly non-wetting surface ($\theta_{\text{eq}} = 180°$), using $\gamma_{lv} = 72$ mN/m at 25°C. However, the highest equilibrium contact angles experimentally observed on smooth surfaces are much lower. Silanization is one of the most efficient chemical process to make a surface hydrophobic, yielding contact angles of 120° at most [108, 109]. Lee *et al.* used this method to make hydrophobic one side of the nanoporous alumina membranes they trap water vapor bubbles into [6]. Micro- and nanopatterned surfaces, which can exhibit higher contact angles (up to 160° in [109]), are not relevant in the present situation [110–112].

Considering $\theta_{\text{eq}} = 120°$, $a_{\max}$ is reduced to 0.7 μm under forward osmosis. Under reverse osmosis, 60 bar are typically applied on the salted-water side for seawater desalination [29]. Such mechanical pressure leads to $a_{\max} \sim 12$ nm. To alleviate this condition on the radius, it is possible to work at lower mechanical pressure, either accepting a water flux reduction, or using less saline water such as brackish water from estuaries, for example.

• *Minimum pore aspect ratio*

Even if the criterion (5.27) is fulfilled, it is not enough to ensure the bubble stability. Indeed, because of the finite pore length, pore filling becomes energetically favorable below a critical aspect ratio $\ell/a_{\min}$.

We now derive the energetic balance describing pore filling, considering that it occurs from the A side which is under mechanical pressure. Work by pressure forces will compensate the energetic cost of new liquid-solid and liquid-liquid interfaces, which writes [5]

$$-\int_{V_0}^{0} \Delta P_A \, \mathrm{d}V + \Delta E = (\gamma_{sl} - \gamma_{sv}) A_{\text{wall}} - \gamma_{lv}(A_{m,A} + A_{m,B}) \quad (5.28)$$

with V_0 the pore volume initially occupied by air, A_{wall} the area of the pore wall, $A_{m,A}$ and $A_{m,B}$ the areas of the A and B menisci. The first term corresponds to the work of pressure forces and ΔE is the additional energy required to induce the filling. On the right hand-side of Eq. (5.28), the A_{wall} term accounts for the air-solid interface being replaced by a liquid-solid interface, and the last term corresponds to the merging of the two liquid-gas menisci. The geometric parameters read

$$V_0 = \pi a^2 \ell + O(a^3) \tag{5.29}$$

$$A_{\text{wall}} = 2\pi a \ell \tag{5.30}$$

$$A_{m,A} = 2\pi r_A h = \frac{2\pi a^2}{1+\sin\theta} \tag{5.31}$$

$$A_{m,B} = \pi a^2, \tag{5.32}$$

where θ is the contact angle, generally different from the equilibrium contact angle used in Young-Laplace equation. It is related to the pressure drop across the A interface according to

$$\Delta P_A = \frac{2\gamma_{lv}}{r_A} = -\frac{2\gamma_{lv}\cos\theta}{a}. \tag{5.33}$$

The pore resists wetting if $\Delta E > 0$, which yields the criterion [5]

$$\frac{\ell}{a} > \frac{1}{\cos\theta - \cos\theta_{\text{eq}}}\left(\frac{1}{2} + \frac{1}{1+\sin\theta}\right). \tag{5.34}$$

Hence, ℓ/a is always more than 1, even for a perfectly non-wetting pore ($\theta_{\text{eq}} = 180°$). Considering moreover $\theta_{\text{eq}} = 120°$, $\Delta P_A = 60$ bar as in reverse osmosis, and $a = 10$ nm, we get $\ell/a > 13$. Decreasing the pore size to $a = 5$ nm yields a more favorable $\ell/a > 3.5$.

Under forward osmosis, $\Delta P_{A/B} = 1$ bar and $\theta = 91° \approx 90°$. Both menisci can be considered as flat, and we get $\ell/a > 1.0$ with $\theta_{\text{eq}} = 180°$,

or $\ell/a > 2.0$ with $\theta_{\text{eq}} = 120°$ ($a = 10$ nm). Therefore, even in forward osmosis, the bubble stability imposes that the pore length equals or exceeds the pore radius: $\ell/a > 1$.

At that stage, one could be tempted to conclude that osmosis through a gas phase is therefore more suited to forward osmosis, than to reverse osmosis. However, the points to be considered are, what flux is targeted, and how much mechanical energy is available, then a compromise must be seeked. This non-trivial compromise should put in balance the effects of the radius, of the aspect ratio and of the mechanical pressure on the total water flux.

We note also that a negative line tension could alleviate the criterion of stability on the aspect ratio. To account for the merging of the two contact lines during the filling, the term $(-4\pi a\lambda)$ is added to the right side of Eq. (5.28), yielding

$$\frac{\ell}{a} > \frac{1}{\cos\theta - \cos\theta_{\text{eq}}}\left(\frac{1}{2} + \frac{1}{1+\sin\theta} + \frac{2\lambda}{\gamma_{lv}a}\right). \tag{5.35}$$

Taking $a = 10$ nm or $a = 8$ Å (typical radius in the simulations, see section 5.3), $\gamma_{lv} = 72$ mN/m and $\lambda = -2.10^{-11}$ N/m^2 [107], we find $\dfrac{2\lambda}{\gamma_{lv}a} = -0.06$ or -0.7 respectively. Thus, in experimental systems the line tension is expected to have no detectable influence, but it could be evidenced with molecular dynamics simulations.
In our numerical studies where θ_{eq} is thought to be close to 180°, we clearly observe spontaneous pore filling for pore lengths smaller than a. However, we did not try to determine more precisely the threshold above which all vapor bubbles are stable. Accounting for the precise influence of the line tension requires dedicated studies, which could be an interesting continuation of the present work.

As a remark to end this paragraph, we note that pore filling occurs for $\Delta E = 0$. From Eq. (5.28), we get

$$\Delta P_A = -\frac{2\gamma_{lv}\cos\theta_{\text{eq}}}{a} - \frac{4\gamma_{lv}}{\ell}\left(\frac{1}{2} + \frac{1}{1+\sin\theta}\right) - \frac{4\lambda}{a\ell}. \tag{5.36}$$

In the limit of an infinite pore length, we recover the Laplace-Washburn law of Eq. (5.25).

To sum up this paragraph, we have shown that the maximum pore radius is given by

$$a_{\max} = -\frac{2\gamma_{lv}\cos\theta_{\text{eq}}}{\Delta P_A}. \tag{5.37}$$

with ΔP_A the pressure drop across the A meniscus, and that the minimal pore aspect ratio is $\ell/a = 1$ at best, but possibly higher depending on the equilibrium contact angle and the pressure across the meniscii.
We now come to the order of magnitude of the permeate flow rate through the membrane.

5.2.4 Order of magnitude of the permeate flow rate

The aim of this paragraph is to compare the presently studied osmosis through a gas phase with traditional reverse osmosis.
We recall the water-vapor mass flux through a hydrophobic nanoporous membrane, in g/(m^2·s),

$$\dot{m} = \Phi \times \frac{\sigma\eta}{2\eta(1-\sigma)+\sigma} \times \sqrt{\frac{m_w}{2\pi k_{\text{B}}T}}\,\frac{\rho^v_{\text{sat}}}{\rho^l}\,(\Delta P - \Delta\Pi),$$

which is plotted as a function of both pore radius a and applied pressure $(\Delta P - \Delta\Pi)$ on Fig. 5.4, assuming a membrane porosity of 40%. The mass flux in this figure is computed for the minimal aspect ratio ensuring the nanobubble stability.

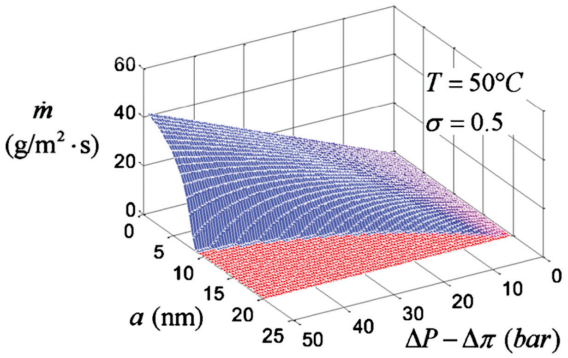

FIGURE 5.4: Predicted mass flux through a nanoporous membrane with different pore sizes and driving pressures. The minimal aspect ratio ℓ/a ensuring an unfavorable channel filling was used, together with a static contact angle $\theta_{eq} = 120°$ and a porosity $\Phi = 40\%$. The red region with zero flux indicates that the pore radius is too large to sustain the applied mechanical pressure drop. Reproduced from [5].

We can see that actually, smaller nanochannels provide higher mass fluxes, because they allow shorter channels to be used. Indeed, the minimal aspect ratio for thermodynamic stability depends on a, through $\cos\theta$ (see Eq. 5.34). Reducing a at constant ℓ reduces indeed the transmission coefficient η, but the gain in reducing ℓ overcomes this trend. All in all, reducing a *and* ℓ so as to keep at the limit of the bubble thermodynamic stability enhances η, and thus the water flux.

A NaCl concentration of 0.62 mol/L (typical seawater concentration) yields an osmotic pressure of roughly 30 bar. For $\Delta P = 60$ bar, commonly used in reverse osmosis, pore sizes of 5-10 nm seem well suited. Such pore sizes are convenient to produce on a large scale, which is the main advantage of this method. With a condensation probability σ of 0.5, and at $T = 50°C$, the mass flux is aroung 10 g/(m^2·s). This is

comparable to or higher than the actual flux rate achieved in reverse osmosis, between 3 and 10 g/(m^2·s) for seawater [29].

It is worth noting that high water fluxes are reach, although transport occurs through a vapor phase with a very low density. Indeed, mass fluw is proportional to $\rho^v_{\text{sat}}/\rho^l$ which is about 10^{-4} for water. One could thus express surprise that transport through a gas phase could compare with liquid reverse-osmosis fluxes [7]. This is because reverse osmosis requires sub-nanometric pores, which hinders considerably liquid flow. Indeed, mass flux per unit membrane area under a Poiseuille flow reads

$$\dot{m}_{\text{Poiseuille}} = \Phi \times \frac{m_w a^2}{8\eta\ell}\,(\Delta P - \Delta\Pi), \tag{5.38}$$

where the $\dfrac{a^2}{\ell}$ factor is the limiting one.

However, recent experimental data show that the condensation coefficient σ is likely to be smaller than 0.5, around 0.2 [6]. What is more, air molecules trapped inside of the bubble result in a smaller transmission coefficient η. The above-mentioned orders of magnitude therefore may be slightly overestimated, but yet the present method is likely to be competitive with reverse osmosis as far as water flux is concerned. Another requirement is that osmosis through a gas phase proves selective enough. This will be shown to be true in section 5.4.2.

In the next part, we focus on the transport properties of an osmotic gaz flow under forward osmosis, and show that Eq. (5.22) giving the water flux through a single nanochannel is robust. To this end, we study the forward osmosis process under way through the bubble using a simple Lennard-Jones two-component fluid. We then investigate the conditions under which the gas bubble is impermeable to salt by measuring the energy-barrier an ion has to overcome to pass through the hydrophobic

tube. In this case, we use the TIP3P model for water and both coulombic and Lennard-Jones interactions between ions and water molecules.

5.3 Characterization of the osmotic transport in a gas phase

In this section, the dependency of the permeability with respect to pore length and radius, and to fluid-particle mass, is investigated with molecular dynamics simulations. We briefly expose the computational details before numerically proving the adequacy of Eq. (5.22).
In the following, we consider only simulations where the vapor bubble is impermeable to ions.

5.3.1 Computational details

Molecular dynamics (MD) provides a molecular-scale resolution of the transport properties. Considering the low number of gas molecules inside hydrophobic nanochannels – around 100 water molecules within the nanochannels experimentally studied by Lee & Karnik of 70-nm diameter and 100-nm length [6] – MD simulations are fully appropriate in the present study.
Moreover, since the seminal article by Hummer and co-workers in 2001 [113], MD simulations are an ideal tool to study nanometer-scale flows. [113] first pointed to the high water flow rates in CNT, fostering much experimental investigations in this direction [68, 69, 104]. Hummer's results on the interactions between water molecules and hydrophobic CNTs also are of great interest, and will be invoked in this section.
In the present work, all the simulations are performed using LAMMPS

[114], a now classical molecular dynamics code. This acronym stands for Large-scale Atomic/Molecular Massively Parallel Simulator. LAMMPS is very convenient as it enables to work on a single processor for test simulations, but also on many processors in parallel. We conducted simulations on as many as 1000 processor cores with no particular difficulty.

• *System*

The system of interest consists in a fixed and rigid nanotube linking two reservoirs, and 2 pistons to compress the fluid in the direction of the tube axis, see Fig. 5.5. The present nanotube is made of a rolled sheet of hexagonally arranged atoms. Even though the use of CNTs in the present work was not compulsory, as we barely needed a material capable of hosting a nanometric gas bubble, several reasons guided our choice. Because of their excellent electrical (and mechanical) properties, the use of CNTs is getting widespread in the nanofluidic community. Moreover, their geometry is easy to implement, and we could benefit from previous MD studies experience [31, 115].

Not only the nanotube, but also the walls at its entrances and the pistons are made of imitation graphene with a distance between nearest neighbors of $d = 0.6$ Å. This value ensures the nanotube and walls impermeability to the Lennard-Jones fluid.

The nanotube connects two fluid reservoirs, one containing a one-component fluid and the second one with a one- or two-component fluid. Periodic boundary conditions were imposed in all directions, and we checked that the reservoir lateral size L was big enough to give accurate data [79]. We typically use $L \gtrsim 5a$.

• *Lennard-Jones fluid*

According to Eq. (5.22), the expected osmotic flux is proportional to the ratio of water vapor density and liquid water density. For water, $\frac{\rho^v_{\text{sat}}}{\rho^l}$ is

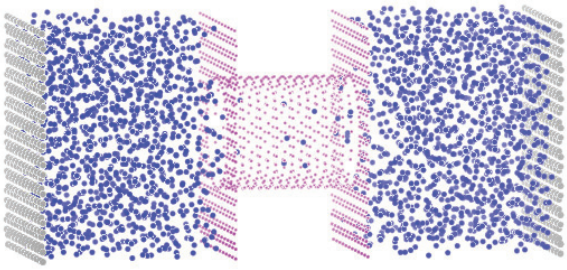

FIGURE 5.5: Snapshot of the system, with only α particles (blue spots). The pistons are in grey, the tube and the walls at its entrances in pink. The system is in an equilibrium state. A bubble of vapor is nucleated inside the tube, whereas the reservoirs contain liquid. Snapshot made with VMD [116].

less than 10^{-4}. We thus chose not to use water models here, but rather a Lennard-Jones fluid for which $\frac{\rho^v_{\text{sat}}}{\rho^l} \sim 0.1$, which provides a faster osmotic transport across the gas phase. Moreover, the models used to simulate water are costly in terms of number of parallel processors and calculation time, whereas Lennard-Jones fluids are easier to implement, time-savers, but still capture the physics at stake.

• *Interaction parameters*

Simulations involve between 2180 and 76050 fluid particles (solvent particles labeled α and solute particles labeled β) interacting solely via the Lennard-Jones potential

$$U(r) = 4\epsilon \left[\left(\frac{\sigma}{r}\right)^{12} - \left(\frac{\sigma}{r}\right)^{6} \right] \tag{5.39}$$

where ϵ is the depth of the potential well, and σ the cross-section, worth the finite distance at which the inter-particle potential $U(r)$ is zero (see Fig. 5.6).

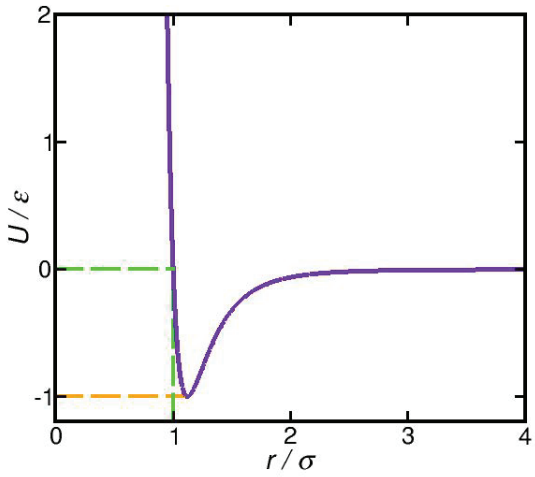

FIGURE 5.6: Reduced Lennard-Jones potential, as a function of the reduced distance r/σ.

Interactions are suppressed among neighboring nanotube atoms, neighboring wall atoms, and neighboring piston atoms. The interaction parameter between two solvent molecules $\epsilon_{\alpha\alpha}$ is such as to keep the reduced temperature $T^* = \dfrac{k_\mathrm{B}T}{\epsilon_{\alpha\alpha}} = 0.9$, which is in between the fluid's triple-point temperature and the critical temperature [117, 118]. The temperature was fixed at 300 K using a Langevin thermostat with a damping parameter of 10 ps. Between the fluid and the tube, or between the fluid and the tube's entrances, the interaction strength is set to

$$\epsilon_{\alpha-\mathrm{tube}} = 0.1\,\epsilon_{\alpha\alpha}, \tag{5.40}$$

and between the fluid and the pistons to

$$\epsilon_{\alpha-\mathrm{piston}} = 0.8\,\epsilon_{\alpha\alpha}. \tag{5.41}$$

These values ensure the hydrophobicity of the nanotube and the hydrophilicity of the pistons: the particles are distributed in both reservoirs, while the tube is nearly empty (see Fig. 5.5). We stress that the phase transition inside the nanotube, from a liquid to a gas phase, is very sharp when reducing $\epsilon_{\alpha-\text{tube}}$, as previously observed by Hummer *et al.* [113]. Moreover, under decreasing $\epsilon_{\alpha-\text{tube}}$, solid-liquid interfaces are replaced by solid-vapor ones at the tube's entrances. This is in full agreement with Nijmeijer and co-workers' results, who observed a drying transition at $\epsilon_{\alpha,\text{tube}} \approx 0.2\,\epsilon_{\alpha\alpha}$ and only solid-vapor interfaces below this value [110, 117, 119].

To mimick the solvation of ions, we choose a high interaction parameter between the solvent and the solute,

$$\epsilon_{\alpha\beta} = 2.3\,\epsilon_{\alpha\alpha}, \tag{5.42}$$

while α and β particles interact similarly with the tube, the walls and the pistons. This high value of the $\alpha - \beta$ interaction parameter ensures that β particles neither evaporate, nor cross the tube.

For the sake of simplicity, we choose cross-sections of 1 Å for the fluid particles:

$$\sigma_{\alpha\alpha} = \sigma_{\beta\beta} = 1\,\text{Å}. \tag{5.43}$$

For the fixed tube and piston atoms, the link between the interatomic distance d and the cross-section σ is given by

$$\sigma_{\text{tube}-\text{tube}/\text{piston}-\text{piston}} = \frac{d}{2^{1/6}} = 0.534\,\text{Å} \tag{5.44}$$

and

$$\sigma_{\alpha-\text{tube}/\alpha-\text{piston}} = \frac{\sigma_{\alpha\alpha} + \sigma_{\text{tube}-\text{tube}/\text{piston}-\text{piston}}}{2} \tag{5.45}$$

according to Lorentz-Berthelot mixing rules.

• *Mechanical pressure*
On each piston, we apply a reference pressure of 3000 atm in order to get the vapor phase only inside the tube, and not spilling over the reservoirs, as in Fig. 5.8. The average vapor density is $0.04/\sigma_{\alpha\alpha}^3$ and the average fluid density is $0.69/\sigma_{\alpha\alpha}^3$, which is in full agreement with [117]. Unless otherwise stated, solvent and solute particles have the same mass $m = 1$ g/mol.

Five different sets of simulations are conducted using solely Lennard-Jones potentials. The first two sets test the correct functioning of the simulations, and the last three explore the dependency of the permeability with the fluid particle mass, pore radius and length.

5.3.2 Pressure-driven flow with no solute

The first set of simulations permits to check that a one-component fluid (i.e. $\Delta\Pi = 0$) under an applied pressure drop ΔP, flows with a constant rate, proportional to the applied pressure drop, see Fig. 5.7. We call permeability, the proportionality coefficient between the flow rate and the pressure drop. It is thus defined as

$$\dot{N} = K(\Delta P - \Delta\Pi) \tag{5.46}$$

and it is expected to behave according to

$$K = \frac{\sigma\eta}{2\eta(1-\sigma)+\sigma} \times \pi a^2 \times \sqrt{\frac{1}{2\pi m_w k_\mathrm{B} T}}\, \frac{\rho_\mathrm{sat}^v}{\rho^l} \tag{5.47}$$

$$= \frac{\sigma\eta}{2\eta(1-\sigma)+\sigma}\, K_\mathrm{max}, \tag{5.48}$$

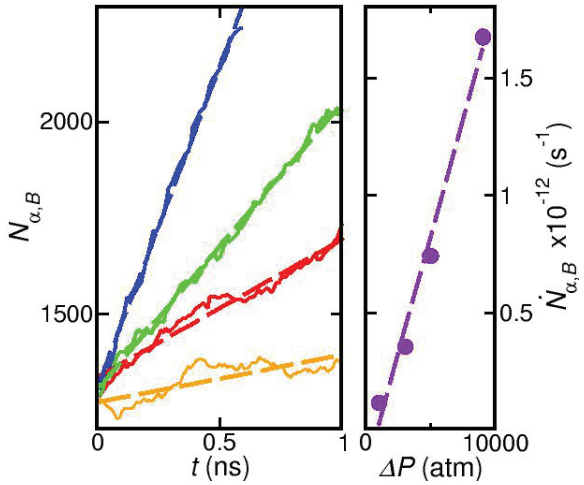

FIGURE 5.7: Response of a one-component Lennard-Jones fluid to an applied pressure drop, vaporizing and flowing through a nanochannel of dimensions $a = 3.4$ Åand $\ell = 8.3$ Å. *(Left)* Number of particles in the right B reservoir as a function of time, while the excess pressure is applied by the left A piston. The curves in yellow, red, green and blue correspond to an applied pressure drop of 1000, 3000, 5000 and 9000 atm respectively. The dashed lines are linear fit of the curves, their slope is plotted on the *right figure* against the excess pressure with purple dots. The purple dashed line is a linear fit of the flux against the excess pressure, its slope is the permeability $K \sim 2.10^8$ atm^{-1}.s^{-1}.

where $K_{\max}$ is the highest reachable permeability with given nanochannel and solvent, attained when $\sigma = \eta = 1$.

In these pressure-driven flows of α particles, through a nanochannel of radius $a = 3.4$ Å and length $\ell = 2.5\,a$, we find for the permeability $K = 2.10^8$ atm^{-1}.s^{-1}, which gives $K/K_{\max} = 0.6$. This value of $K/K_{\max}$ is close to the predicted value (0.5) calculated using Eq. (5.21) with a condensation coefficient $\sigma = 1$, (see Fig. 5.10 page 161). The discrepancy between these two values may come from reservoirs being too small in these simulations.

5.3.3 Evolution of the number of solvent particles under an osmotic forcing

Subsequent sets of simulations involve a concentration gradient, which entails an osmotic forcing. From now on, solvant flows are driven by forward osmosis. We first checked that the initial flow rate $\dot{N}_{\alpha,A}(t=0)$ with an initial osmotic pressure $\Delta\Pi\,(t=0)$ was the same than the flux rate with an applied excess pressure ΔP worth $-\Delta\Pi\,(t=0)$.

Then, the flow of α particles as a function of time is considered. Under a salt concentration difference between two reservoirs, the number of α particles in the A reservoir (the "seawater" side) $N_{\alpha,A}(t)$ does not increase linearly with time, as it would be under an applied excess pressure. It can be shown that it follows an algebraic law,

$$N_{\alpha,A}(t) = N^0_{\text{tot},A}\sqrt{1+\kappa K t} - N_\beta \tag{5.49}$$

with $N^0_{\text{tot},A}$ the total number of particles in the A reservoir at $t=0$, N_β the number of β particles which is constant, and $\kappa = 2\dfrac{k_\text{B}TN_\beta\rho^l}{(N^0_{\text{tot},A})^2}$.

Of course $N_{\alpha,A}$ does not increase infinitely, but until the A reservoir is drained. More precisely, the complete draining of a reservoir is never observed. As in Fig. 5.8, one to three strongly-organized layers of solvent molecules always remained between the piston and the tube. The same observation can be done with water simulations. The special stability of 2D sheets of water was first reported by Kalra and co-workers [120], who showed that fluctuations adding or removing atoms from such layers are strongly suppressed as compared to a bulk situation. They point to a metastability arising from the molecule orientations, leading to close to three in-plane hydrogen bonds per molecule. As a comparison, water molecules exhibit four hydrogen bonds per molecule

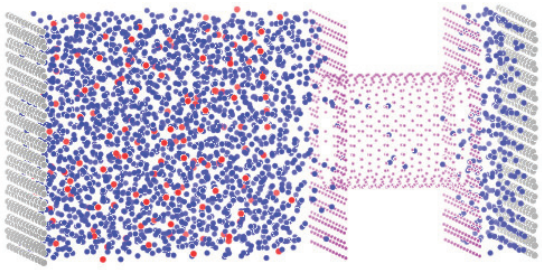

FIGURE 5.8: Out-of-equilibrium ending of a run, where the solvent from the B reservoir (on the right) moved through the bubble and diluted the two-component reservoir (on the left) under forward osmosis ($\Delta P = 0$). Snapshot made with VMD [116].

under the ice phase, and around 3.5 hydrogen bonds on average in the bulk liquid phase [121]. Such phenomenon of water layering near hydrophilic solid surfaces has received much attention from transport studies in porous media [122].

5.3.4 Investigation of the permeability dependencies

In the last three sets of simulations with Lennard-Jones fluids, we focus on the dependencies of the permeability K with respect to the particle mass m, and then the dependency of $K/K_{\max}$ with a/l under forward osmosis.

Rewriting Eq. (5.49), the square of the normalized number of α particles in the A reservoir is expected to behave as

$$\left(\frac{N_{\alpha,A}(t) + N_\beta}{N^0_{\text{tot},A}} \right)^2 = 1 + \kappa K t, \tag{5.50}$$

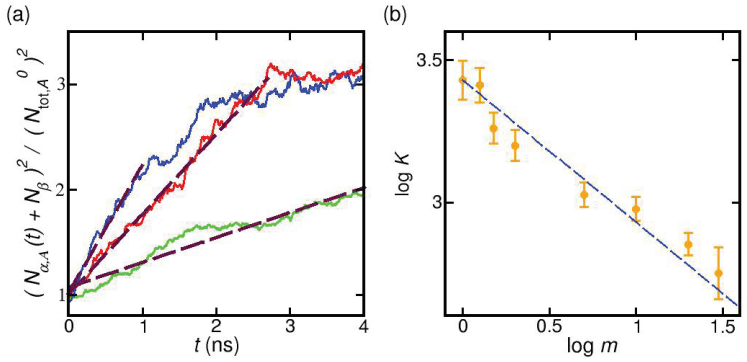

FIGURE 5.9: Results from simulations with $a = 3.4$ Å, $l = 8.3$ Å and various m (a) $\left(\frac{N_{\alpha,A}(t)+N_\beta}{N^0_{\mathrm{tot},A}}\right)^2$ as a function of time, for $m = 1$ (in blue) $m = 2$ (in red) and $m = 30$ g/mol (in green). The blue and the red curves saturate around 2 and 3 ns respectively, because of the pure water reservoir draining. The maroon dashed lines are examples of linear fits crossing the y-axis between 0.9 and 1.1 (see text). (b) *Orange dots* : log K as a function of log m, with K in $\mathrm{Pa}^{-1}\mathrm{s}^{-1}$ and m in g/mol. The blue dashed line has a slope of -0.5, it is only a guide for the eye.

which provides an easy access to the permeability K. The curves obtained from the simulations, such as the ones plotted on Fig. 5.9-a, are indeed well described by Eq. (5.50) before the (incomplete) draining of the B reservoir is achieved. We perform several linear fits on different time scales, and keep only those cutting the ordinate axis at 1 ± 0.1. From these different fits we extract an average of K and a standard deviation which are represented in Fig. 5.9-b and Fig. 5.10 by points and error bars respectively.

As can be seen in Fig. 5.9-b, log K as a function of log m can be fitted by a linear function of slope -0.5, which is in full agreement with the dependency of $K \sim 1/\sqrt{m}$ proposed in Eq. (5.22). We now turn to

the computation of $K/K_{\max}$ under various pore sizes and lengths. For varying pore radius, the pore legnth was fixed to $\ell = 8.3$ Å , and for varying pore length the pore radius was $a = 8.3$ Å.

As established in Eq. (5.48), the theoretical expression of $K/K_{\max}$ is

$$\frac{K}{K_{\max}} = \frac{\sigma\eta}{2\eta(1-\sigma)+\sigma} \tag{5.51}$$

which, according to Eq. (5.21), is a function of the aspect ratio ℓ/a. For long pores ($\ell \to \infty$), Eq. (5.21) results in [5]

$$\eta \longrightarrow \frac{8}{3}\frac{a}{\ell}. \tag{5.52}$$

Adding the hypothesis of a perfect condensation ($\sigma = 1$), we thus get

$$\left.\frac{K}{K_{\max}}\right|_{\ell\to\infty} = \frac{\sigma\eta}{2\eta(1-\sigma)+\sigma} = \frac{8}{3}\frac{a}{l}. \tag{5.53}$$

On Fig. 5.10, the numerical results of K normalized by $K_{\max}$ are compared to the theoretical expressions (5.51) and (5.53). Numerical data are well represented by Eq. (5.51) with a condensation coefficient σ comprised between 0.75 and 1. Indeed, all data from osmosis simulations, either with a varying tube length or a varying tube radius, fall between those two theoretical curves. In the case where the inverse aspect ratio a/ℓ is below 0.2, K/K_{max} is reasonably accounted for by the simpler expression of Eq. (5.53).

The determination of the condensation probability is an issue on which no general agreement has emerged yet. For Lennard-Jones fluids, values between 0.1 and 1 have been proposed [123], while $\sigma = 1$ is typically used in calculations [124]. The estimate we provide is therefore not unreasonable.

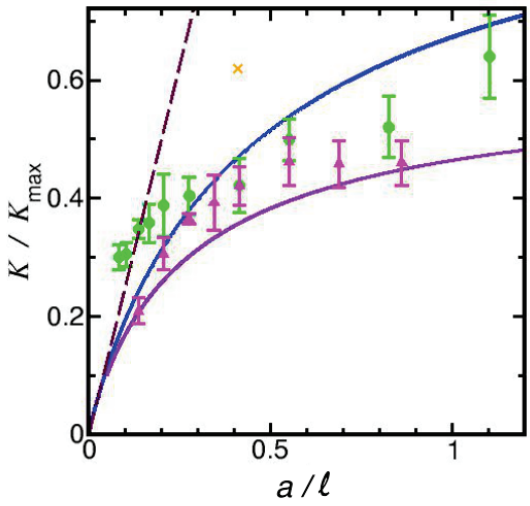

FIGURE 5.10: $K/K_{\max}$ as a function of a/ℓ. *Blue and purple solid line* : prediction of Eq. (5.51) with $\sigma = 1$ and $\sigma = 0.75$ respectively. *Maroon dashed line* : prediction of Eq. (5.53), which is the limit of Eq. (5.51) for long pores and $\sigma = 1$. It is the tangent at the origin of the blue curve. *Green points and squares* stand for simulations where the tube length varies. *Pink triangles* stand for simulations where the tube radius varies. All those points were obtained from forward-osmotic processes. The *orange X-mark* is the result of a hydraulic-pressure driven flow with a zero osmotic pressure.

Note that the same (if not wider) discrepancy exists within the experimental and theoretical results for σ [125]. Lee *et al.* recently reported an experimental value of 0.23 at 39°C, with a slowly decreasing trend upon increasing temperature [6].

It would be of interest to carry on the same simulations with water models. Since the Bernal-Fowler model published in 1933 [126], many water models have been proposed, usually designed to better reproduce one property in particular. Although it has been suggested that molecular dynamics simulations could be used to determine the water condensation

probability [127], current water models may not be accurate enough for this purpose, as they hardly account for both liquid *and* gas properties [128, 129]. In any case, this question deserves a dedicated study, for which the TIP4P/2005 model could be promising [128, 130].

We now turn to the study of the selectivity of a vapor phase trapped in a nanochannel, between two liquid reservoirs.

5.4 Selectivity of a hydrophobic nanotube

The selectivity of the non-conventional semi-permeable osmosis membrane used in the present study relies on the nanobubble stability. Indeed, ions are very unlikely to cross a vapor phase. To maintain the bubble integrity, it was exposed in section 5.2.3 that limitations to the pore radius and aspect ratio are required. In the performed numerical simulations, it was observed that the vapor bubble is stable for pore lengths down to $\ell = a$. For $\ell \lesssim a$, the vapor phase seems stable, but it is likely that transient liquid bursts carry ions toward the pure-water reservoir. For values of ℓ lower than a, the vapor bubble is quickly filled with liquid water.

To rationalize the observed behaviors, we now focus on the energy barrier encountered by ions when crossing the tube. This energy barrier is called the potential of mean force (PMF). In the following, the PMF is measured for various tube lengths, resorting to the umbrella sampling technique. Umbrella sampling is briefly described in the next paragraph along with the choosen parameters. We investigate both the impermeable case where $\ell/a > 1$, and the permeable case when this condition is no longer fulfilled.

5.4.1 Computational details and umbrella sampling method

As in the previous section, the calculations are performed with LAMMPS. The geometry is the same as before (see Fig. 5.5-a) : an armchair single-wall nanotube made of a rolled graphene sheet, two reservoirs delimited by graphene walls at the tube entrances and by graphene pistons which pressure was set to 1 atm. Carbon nearest neighbors are spaced with $d = 1.418$ Å. The tube radius is fixed at 8.1 Å, while tube lengths range from 2.5 to 39 Å.

To describe water molecules, the TIP3P model was used [131], as it is both easy to implement and efficient in terms of calculation time. The following results may be refined by using a more sophisticated model such as TIP4P/2005 [130].

The interactions between water and the nanochannel (and the walls at its entrances) are modeled with a Lennard-Jones potential of parameters $\epsilon_{\text{O-tube}} = 0.001$ kcal/mol and $\sigma_{\text{O-tube/O-piston}} = 3.28$ Å. Between water and the pistons, we used the classical value $\epsilon_{\text{O-piston}} = 0.114$ kcal/mol [115].

O-H bonds are fixed using the SHAKE algorithm. Long range Coulombic forces are computed using the particle-particle particle-mesh (PPPM) method [132]. Calculations are performed in the nve ensemble and temperature is set at 300 K with a Dissipative Particle Dynamics thermostat [133]. A time step of 1 fs is used and, typically, simulations of a few nanoseconds are performed.

Two ions, K^+ and Cl^-, are put in one of the reservoirs. Ions interact with the carbon atoms with the same parameters as oxygen. At the beginning of each run, the tube is empty from water molecules and separated from the reservoirs with two graphene sheets. We let the reservoirs equilibrate during 0.1 ns before removing these sheets. Then,

the ions are driven through the z-axis tube, starting from 11 Å from the tube's entrance and by steps of 1.6 Å. To this end, we apply an harmonic bias of stiffness $b = 1$ kJ/mol/Å^2 on the z-coordinate of both ions, which are trapped during 0.1 to 0.5 ns in the same position z_i. This method is called the umbrella sampling technique [134, 135].
We calculate pieces of the PMF of Cl^- according to

$$F_i(z) = -k_B T \ln p_i(z) - \frac{1}{2} b(z - z_i)^2 + C_i \tag{5.54}$$

where the subscript $_i$ refers to the position of the trap. $p_i(z)$ is the probability of finding the ion in z, z_i is the center of the $i-$th trap and C_i is an unknown constant. Thanks to the small overlaps between them, we manually rescale the F_i curves to get the entire energy profile $F(z)$. Alternatively, one could use the automated weighted histogram analysis method (WHAM) [135].

5.4.2 Energy barrier experienced by an ion crossing the nanotube

As can be seen on Fig. 5.11, the computed PMF are symmetrical with respect to $z = 0$. For a tube radius of 8.1 Å, the maximum energy barrier is $30\, k_B T$ (75 kJ/mol). This result can be compared to the 75 and 52 kJ/mol found by Song & Corry to fully dehydrate Na^+ and Cl^- respectively [136]. Here we do not dehydrate the ions, so one could expect a lower energy barrier. But as the tube is hydrophobic, water molecules surroundings the ions are also reluctant to enter it, which possibly raises the PMF.

The PMF reaches and plateaus at the maximum value of $30\, k_B T$ only for tubes longer than ~ 20 Å (*i.e.* $\ell/a > 2.5$). In this case, we observe that when ions are driven through the bubble by umbrella sampling, a

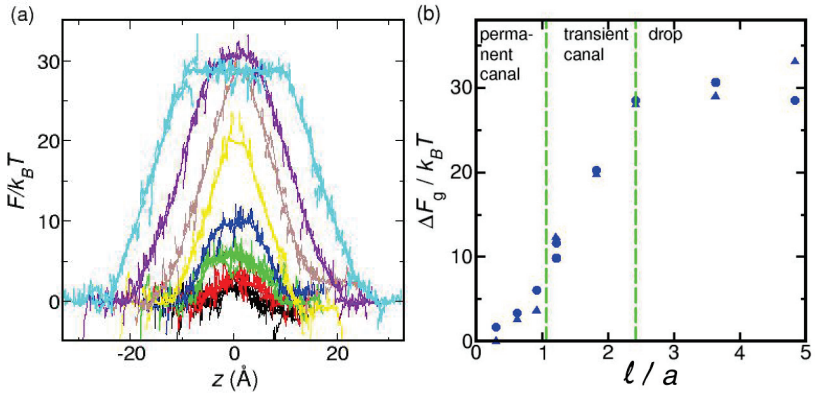

FIGURE 5.11: PMF of an ion Cl^- crossing a hydrophobic nanotube of radius 8.1 Å. (a) PMF along the z-coordinate for different tube lengths : 2.5 Å (black), 4.9 Å (red), 7.4 Å (green), 9.8 Å (blue), 14.7 Å (yellow), 19.6 Å (brown), 29.5 Å (purple) and 39.3 Å (cyan curve). (b) Height of the free energy barrier as a function of the aspect ratio. Ions were trapped during 0.1 ns (dots) or 0.2 ns (triangles) in each position. We evidenced 3 regimes, whether a water canal would establish instantly ($\ell/a \leq 1$), or only when the ions get through the tube entrance ($1 \leq \ell/a \leq 2.5$), or whether a drop would detach from the reservoir to travel inside the tube ($\ell/a \geq 2.5$).

liquid drop containing the two ions and various water molecules (from 6 to 17 in our simulations) detaches from one reservoir (see Fig. 5.12-top). For $1 < \ell/a < 2.5$, ions have to overcome a smaller barrier. It corresponds to the case where, when ions are already engaged inside the channel, a liquid canal sets inside the tube (see Fig. 5.12-bottom). The canal disappears when the ions reach the second reservoir.

Tubes shorter than 8 Å (*i.e.* $\ell/a < 1$) are not impermeable to ions because the bubble is unstable. Liquid water flows inside the tube, and so do ions. Still, ions experience an energy barrier to cross these tubes, which can be as high as $6\,k_BT$. This comes from a reduction of the coordination number as an ion gets into the tube [136]. Another

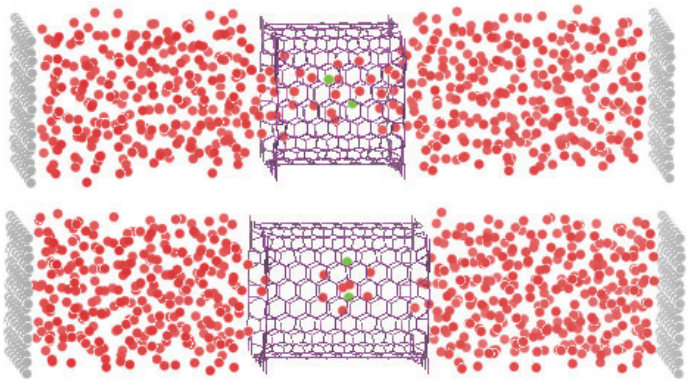

FIGURE 5.12: Snapshots of two different umbrella-sampling processes occurring inside an impermeable tube ($\ell/a > 1$). Water molecules are represented in red and the ions in green. *(Top :)* $\ell/a = 2$, a canal forms and links the two reservoirs. *(Bottom :)* $\ell/a = 2.5$, a drop forms containing the ions and a few water molecules. Snapshots made with VMD [116].

explanation could lie in the lower relative permittivity of the nanotube, compared to that of water. It results in a dielectric exclusion of the ions inside the nanochannel [137, 138], which is energetically defavorable.

As a last remark, we note that the slopes of the PMF along the z-coordinate are identical, and that the barrier sets up on a typical distance ~ 15 Å, which compares to the tube diameter.

5.5 Partial conclusion

In this section, we considered a new desalination method, combining the advantages of osmosis processes such as reverse and forward osmosis, and

of membrane distillation. The osmotic process at stake in this method makes use of a vapor bubble, trapped inside of a nanochannel, as a semi-permeable membrane. Even though the bubble-stability requirement adds constraints to the pore radius and length, which are limited by a maximum radius and a minimal aspect ratio ℓ/a respectively, this method is throught to be as efficient as reverse osmosis.

Using molecular dynamics, we investigated the water-flow properties, especially its dependence with the particle mass and the geometric characteristics of the nanochannel. Then, we computed the energy barrier an ion should overcome to penetrate into and cross the vapor phase. For impermeable nanobubbles, its value is between 10 and $30\,k_{\mathrm{B}}T$. We believe that these values are high enough the prevent ions from crossing the tube with a close to 100% probability.

Simulations of forward and reverse osmosis in a more realistic system are ongoing. They require huge computing capacities. For example, using a nanochannel of radius and length 7 nm, we simulated the dynamics of 35.000 water molecules. Moreover, simulations with more accurate water models such as TIP4P/2005 [128, 130] are also about to be performed, which should provide more precise numerical data. The surface tension values, as well as the liquid-vapor co-existence parameters, are expected to be the main changes.

Conclusion

In this thesis, we rationalized the collective effect occurring at pore entrances, and studied their influence on transport properties. We showed that whereas the ionic conductance scales sub-linearly with the number of channels, the hydrodynamic permeability keeps an extensive behavior. Using the deep analogy between diffusive and conductive ion transport, we concluded that the salt diffusive flux also scaled sub-linearly with the number of pores.

In a second time, we deduced the behaviors of cross-coupling phenomena. Unexpected and far from trivial, the scalings of transport phenomena show that it will not be an easy task to benefit from nanosize good properties on a macroscopic scale. Designing energy harvesting devices from nanofluidic building blocks requires ingenuity to bypass collective entrance effects, which occur at the frontier between the nano-materials and the macroscopic reservoirs.

Using molecular dynamics simulations, we also carried a study on a new concept for water desalination, of which the selectivity and permeability have been investigated. Along with existing experimental results, our results show that osmosis through a gas phase is competitive with reverse osmosis, from which it is inspired. Moreover, it is possibly

easier to implement on a large scale than reverse osmosis, because the semi-permeable membrane is replaced by a membrane with larger pore than those required by reverse osmosis.

With the expected end of the fossil-energy era, it is important that new technologies are proposed and developed, to sustain the global demand. Nanofluidics is a very helpful tool for this purpose, as evidenced by the recent contributions on shale-gas desorption and transport [139, 140]. Many countries are in a dynamical development phase, and energy is one of the main support of economical growth. Thus the need in energy keeps increasing. So does the need in fresh water supply, which follows the rhythm of the population growth. Climate change deepens the fresh water shortage, leading countries and industries to invest massively in water purification facilities. But in water purification, as in energy harvesting, devices working at many different scales cohabit. From the nuclear power plant to the solar cells on rooftops of houses, the tendency is to the multiplication of devices, in parallel with the multiplication of involved actors, from the individual to the city or the company. Providing new devices and new solutions to accompany the changes under way in the society may well be the most exciting challenges indeed.

Bibliography

[1] L. Bocquet, P. Tabeling, *Lab on a Chip* **2014**, *14*, 3143–3158.

[2] B. Hille, *The Journal of General Physiology* **1968**, *51*, 199–219.

[3] J. E. Hall, *The Journal of General Physiology* **1975**, *66*, 531–532.

[4] R. A. Sampson, *Philosophical Transactions of the Royal Society of London A* **1891**, *182*, 449–518.

[5] J. Lee, R. Karnik, *Journal of Applied Physics* **2010**, *108*, 044315.

[6] J. Lee, T. Laoui, R. Karnik, *Nature Nanotechnology* **2014**, *9*, 317–23.

[7] L. Bocquet, *Nature Nanotechnology* **2014**, *9*, 249–251.

[8] L. Bocquet, E. Charlaix, *Chemical Society Reviews* **2010**, *39*, 1073–1095.

[9] R. Villey, E. Martinot, C. Cottin-Bizonne, M. Phaner-Goutorbe, L. Léger, F. Restagno, E. Charlaix, *Physical Review Letters* **2013**, *111*, 215701.

[10] R. B. Schoch, H. van Lintel, P. Renaud, *Physics of Fluids* **2005**, *17*, 2–7.

[11] D. Andelman in *Handbook of Biological Physics*, *Vol. 1*, **1995**, pp. 603–641.

[12] C. Lee, L. Joly, A. Siria, A.-L. Biance, R. Fulcrand, L. Bocquet, *Nano Letters* **2012**, *12*, 4037–4044.

[13] J. Palacci, *Manipulation of colloids by osmotic forces*, PhD thesis, Université Claude-Bernard, Lyon, France, **2010**.

[14] S. Levine, J. R. Marriott, K. Robinson, *Journal of the Chemical Society Faraday Transactions 2* **1975**, *71*, 1.

[15] A. Siria, P. Poncharal, A.-L. Biance, R. Fulcrand, X. Blase, S. T. Purcell, L. Bocquet, *Nature* **2013**, *494*, 455–458.

[16] F. H. J. van der Heyden, D. J. Bonthuis, D. Stein, C. Meyer, C. Dekker, *Nano Letters* **2007**, *7*, 1022–1025.

[17] T. Nguyen, Y. Xie, L. J. de Vreede, A. van den Berg, J. C. T. Eijkel, *Lab on a Chip* **2013**, *13*, 3210–6.

[18] J. A. Nollet in *Mémoires de Mathématique et de Physique, tirés des registres de l'Académie Royale des Sciences de l'année 1748*, Paris, **1748**, pp. 57–104.

[19] B. Cabane, S. Hénon, *Liquides: solutions, dispersions, émulsions, gels*, Belin, Paris, **2007**.

[20] T. Y. Cath, A. E. Childress, M. Elimelech, *Journal of Membrane Science* **2006**, *281*, 70–87.

[21] I. L. Alsvik, M. B. Hägg, *Polymers* **2013**, *5*, 303–327.

[22] S. Daer, J. Kharraz, A. Giwa, S. W. Hasan, *Desalination* **2015**, *367*, 37–48.

[23] M. Elimelech, W. A. Phillip, *Science* **2011**, *333*, 712–717.

[24] P. Długołecki, J. Dabrowska, K. Nijmeijer, M. Wessling, *Journal of Membrane Science* **2010**, *347*, 101–107.

[25] S. Loeb, R. S. Norman, *Science* **1975**, *189*, 654–655.

[26] N. Y. Yip, M. Elimelech, *Environmental Science and Technology* **2012**, *46*, 5230–5239.

[27] N. Y. Yip, M. Elimelech, *Environmental Science and Technology* **2014**, *48*, 11002–11012.

[28] B. E. Logan, M. Elimelech, *Nature* **2012**, *488*, 313–319.

[29] T. Humplik, J. Lee, S. C. O'Hern, B. A. Fellman, M. A. Baig, S. F. Hassan, M. A. Atieh, F. Rahman, T. Laoui, R. Karnik, E. N. Wang, *Nanotechnology* **2011**, *22*, 292001.

[30] K. P. Lee, T. C. Arnot, D. Mattia, *Journal of Membrane Science* **2011**, *370*, 1–22.

[31] K. Falk, F. Sedlmeier, L. Joly, R. R. Netz, L. Bocquet, *Nano Letters* **2010**, *10*, 4067–4073.

[32] D. Cohen-Tanugi, J. C. Grossman, *Nano Letters* **2012**, *12*, 3602–3608.

[33] J.-L. Barrat, J.-P. Hansen, *Basic Concepts for Simple and Complex Liquids*, Cambridge University Press, **2003**.

[34] L. Bocquet, A. Siria, A.-L. Biance, P. Poncharal, *French pat.*, *1259847*, **2012**.

[35] M. S. El-Bourawi, Z. Ding, R. Ma, M. Khayet, *Journal of Membrane Science* **2006**, *285*, 4–29.

[36] E. Korngold in *Synthetic membrane processes*, **1984**, pp. 191–220.

[37] Y. Oren, *Desalination* **2008**, *228*, 10–29.

[38] M. E. Suss, S. Porada, X. Sun, P. M. Biesheuvel, J. Yoon, V. Presser, *Energy & Environmental Science* **2015**, *8*, 2296–2319.

[39] C. Dekker, *Nature Nanotechnology* **2007**, *2*, 209–216.

[40] W. Guo, L. Cao, J. Xia, F. Q. Nie, M. Wen, J. Xue, Y. Song, D. Zhu, Y. Wang, L. Jiang, *Advanced Functional Materials* **2010**, *20*, 1339–1344.

[41] M. Napoli, J. C. T. Eijkel, S. Pennathur, *Lab on a Chip* **2010**, *10*, 957–985.

[42] S. Howorka, Z. S. Siwy, *Chemical Society Reviews* **2009**, *38*, 2360–2384.

[43] Z. S. Siwy, S. Howorka, *Chemical Society Reviews* **2010**, *39*, 1115–1132.

[44] O. A. Saleh, L. L. Sohn, *Proceedings of the National Academy of Sciences of the United States of America* **2003**, *100*, 820–824.

[45] N. F. Y. Durand, P. Renaud, *Lab on a Chip* **2009**, *9*, 319–324.

[46] I. Vlassiouk, P. Y. Apel, S. N. Dmitriev, K. Healy, Z. S. Siwy, *Proceedings of the National Academy of Sciences of the United States of America* **2009**, *106*, 21039–21044.

[47] C. C. Striemer, T. R. Gaborski, J. L. McGrath, P. M. Fauchet, *Nature* **2007**, *445*, 749–753.

[48] M. Wanunu, W. Morrison, Y. Rabin, A. Y. Grosberg, A. Meller, *Nature Nanotechnology* **2010**, *5*, 160–165.

[49] G. F. Schneider, S. W. Kowalczyk, V. E. Calado, G. Pandraud, H. W. Zandbergen, L. M. K. Vandersypen, C. Dekker, *Nano Letters* **2010**, *10*, 3163–3167.

[50] S. Garaj, W. Hubbard, a. Reina, J. Kong, D. Branton, J. a. Golovchenko, *Nature* **2010**, *467*, 190–193.

[51] S. C. O'Hern, C. A. Stewart, M. S. H. Boutilier, J. C. Idrobo, S. Bhaviripudi, S. K. Das, J. Kong, T. Laoui, M. Atieh, R. Karnik, *ACS Nano* **2012**, *6*, 10130–10138.

[52] A. Gadaleta, A.-L. Biance, A. Siria, L. Bocquet, *Nanoscale* **2015**, 7965–7970.

[53] A. Gadaleta, C. Sempere, S. Gravelle, A. Siria, R. Fulcrand, *Physics of Fluids* **2014**, *012005*, 1–11.

[54] I. Vodyanoy, S. M. Bezrukov, *Biophysical Journal* **1992**, *62*, 10–11.

[55] J. D. Jackson, *Classical Electrodynamics*, Wiley, New York, **1962**.

[56] P. Laüger, *Biochimica et Biophysica Acta* **1976**, *455*, 493–509.

[57] M. Aguilella-Arzo, V. M. Aguilella, R. S. Eisenberg, *European Biophysics Journal* **2005**, *34*, 314–322.

[58] S. W. Kowalczyk, A. Y. Grosberg, Y. Rabin, C. Dekker, *Nanotechnology* **2011**, *22*, 315101–315105.

[59] D. Stein, M. Kruithof, C. Dekker, *Physical Review Letters* **2004**, *93*, 035901.

[60] R. J. Hunter, *Zeta Potential in Colloid Science*, Elsevier, **1981**.

[61] M. Firnkes, D. Pedone, J. Knezevic, M. Döblinger, U. Rant, *Nano Letters* **2010**, *10*, 2162–2167.

[62] M. Mao, S. Ghosal, G. Hu, *Nanotechnology* **2013**, *24*, 245202.

[63] R. Fulcrand, N. P. Blanchard, A.-L. Biance, A. Siria, P. Poncharal, L. Bocquet in *FIB Nanostructures SE - 15*, *Vol. 20*, (Ed.: Z. M. Wang), Springer International Publishing, **2013**, pp. 373–389.

[64] P. Vanysek in *CRC Handbook of Chemistry and Physics, Internet Version 2005*, (Ed.: D. R. Lide), CRC Press, Boca Raton, FL, **2005**.

[65] F. H. J. van der Heyden, D. J. Bonthuis, D. Stein, C. Meyer, C. Dekker, *Nano Letters* **2006**, *6*, 2232–2237.

[66] S. Gravelle, L. Joly, F. Detcheverry, C. Ybert, C. Cottin-Bizonne, L. Bocquet, *Proceedings of the National Academy of Sciences of the United States of America* **2013**, *110*, 16367–72.

[67] M. Majumder, N. Chopra, B. J. Hinds, *Journal of the American Chemical Society* **2005**, *127*, 9062–9070.

[68] J. K. Holt, H. G. Park, Y. Wang, M. Stadermann, A. B. Artyukhin, C. P. Grigoropoulos, A. Noy, O. Bakajin, *Science* **2006**, *312*, 1034–1037.

[69] M. Whitby, L. Cagnon, M. Thanou, N. Quirke, *Nano Letters* **2008**, *8*, 2632–2637.

[70] M. A. Shannon, P. W. Bohn, M. Elimelech, J. G. Georgiadis, B. J. Mariñas, A. M. Mayes, *Nature* **2008**, *452*, 301–310.

[71] R. Semiat, *Environmental Science and Technology* **2008**, *42*, 8193–8201.

[72] K. H. Jensen, A. X. C. N. Valente, H. A. Stone, *Physics of Fluids* **2014**, *26*, 052004.

[73] I. Gallagher, Autour des équations de Navier-Stokes, **2010**, `http://images.math.cnrs.fr/Autour-des-equations-de-Navier.html` (visited on 07/25/2015).

[74] J. D'Alembert, *Essai d'une nouvelle théorie de la résistance des fluides*, Paris, **1752**.

[75] L. Euler, *Physica D* **2008**, *237*, 1840–1854.

[76] C. Navier, *Mémoires de l'Académie des Sciences de l'Institut de France* **1822**, *6*, 375–394.

[77] G. Stokes, *Transactions of the Cambridge Philosophical Society* **1845**, *8*, 287–319.

[78] H. H. Winter, *Calculation and Measurement Techniques for Momentum Energy and Mass Transfer* **1987**, *7*, 27–34.

[79] S. Gravelle, L. Joly, C. Ybert, L. Bocquet, *The Journal of Chemical Physics* **2014**, *141*, 18C526.

[80] M. M. Couette, *Annales de Chimie et Physique* **1890**, *21*, 433–510.

[81] H. L. Weissberg, *Physics of Fluids* **1962**, *5*, 1033.

[82] Z. Dagan, S. Weinbaum, R. Pfeffer, *Journal of Fluid Mechanics* **1982**, *115*, 505–523.

[83] C. Cottin-Bizonne, S. Jurine, J. Baudry, J. Crassous, F. Restagno, E. Charlaix, *The European Physical Journal E* **2002**, *9*, 47–53.

[84] J. A. Thomas, A. J. H. McGaughey, *Nano Letters* **2008**, *8*, 2788–2793.

[85] S. Joseph, N. R. Aluru, *Nano Letters* **2008**, *8*, 452–458.

[86] S. K. Kannam, B. D. Todd, J. S. Hansen, P. J. Daivis, *The Journal of Chemical Physics* **2013**, *138*, 094701.

[87] T. B. Sisan, S. Lichter, *Microfluidics and Nanofluidics* **2011**, *11*, 787–791.

[88] W. D. Nicholls, M. K. Borg, D. A. Lockerby, J. M. Reese, *Microfluidics and Nanofluidics* **2012**, *12*, 257–264.

[89] H. Hasimoto, *Journal of the Physical Society of Japan* **1958**, *13*, 633–639.

[90] K. K. Tio, S. S. Sadhal, *Applied Scientific Research* **1994**, *52*, 1–20.

[91] C. Y. Wang, *AIChE Journal* **1994**, *40*, 419–423.

[92] W. N. Bond, *Proceedings of the Physical Society of London* **1921**, *34*, 139.

[93] F. C. Johansen, *Proceedings of the Royal Society of London A: Mathematical Physical and Engineering Sciences* **1930**, *126*, 231–245.

[94] D. S. Viswanath, T. Ghosh, D. H. L. Prasad, N. V. K. Dutt, K. Y. Rani, *Viscosity of Liquids: Theory, Estimation, Experiment, and Data*, Springer Netherlands, **2007**.

[95] L. Onsager, *Physical Review* **1931**, *38*, 2265–2279.

[96] M. Mao, J. D. Sherwood, S. Ghosal, *Journal of Fluid Mechanics* **2014**, *749*, 167–183.

[97] X. Li, C. Wang, *Journal of Materials Chemistry A* **2013**, *1*, 165–182.

[98] D. K. Kim, C. Duan, Y. F. Chen, A. Majumdar, *Microfluidics and Nanofluidics* **2010**, *9*, 1215–1224.

[99] S. Loeb, S. Sourirajan, *US Pat.*, *3133132*, **1964**.

[100] T. Matsuura, *Desalination* **2001**, *134*, 47–54.

[101] B. Corry, *The Journal of Physical Chemistry B* **2008**, *112*, 1427–1434.

[102] F. Fornasiero, H. G. Park, J. K. Holt, M. Stadermann, C. P. Grigoropoulos, A. Noy, O. Bakajin, *Proceedings of the National Academy of Sciences of the United States of America* **2008**, *105*, 17250–17255.

[103] B. Corry, *Energy & Environmental Science* **2011**, *4*, 751.

[104] M. Majumder, N. Chopra, R. Andrews, B. J. Hinds, *Nature* **2005**, *438*, 44.

[105] R. K. Pathria, P. D. Beale, *Statistical Mechanics*, Academic Press, Elsevier, Third edition, **2011**.

[106] A. S. Berman, *Journal of Applied Physics* **1965**, *36*, 3356.

[107] B. Lefevre, A. Saugey, J.-L. Barrat, L. Bocquet, E. Charlaix, P. F. Gobin, G. Vigier, *The Journal of Chemical Physics* **2004**, *120*, 4927–4938.

[108] M. Reyssat, D. Quéré, *Pour la Science* **2006**, *347*, 34–40.

[109] A. Lafuma, D. Quéré, *Nature Materials* **2003**, *2*, 457–460.

[110] W. Mickel, L. Joly, T. Biben, *The Journal of Chemical Physics* **2011**, *134*, 094105.

[111] T. Biben, L. Joly, *Physical Review Letters* **2008**, *100*, 186103.

[112] Y. C. Jung, B. Bhushan, *Nanotechnology* **2006**, *17*, 4970–4980.

[113] G. Hummer, J. C. Rasaiah, J. P. Noworyta, *Nature* **2001**, *414*, 188–190.

[114] S. Plimpton, *Journal of Computational Physics* **1995**, *117*, 1–19.

[115] L. Joly, *The Journal of Chemical Physics* **2011**, *135*, 214705.

[116] W. Humphrey, A. Dalke, K. Schulten, *Journal of Molecular Graphics* **1996**, *14*, 33–38.

[117] M. J. P. Nijmeijer, C. Bruin, A. F. Bakker, J. M. J. van Leeuwen, *Physical Review A* **1990**, *42*, 6052–6059.

[118] J. Pérez-Pellitero, P. Ungerer, G. Orkoulas, A. D. Mackie, *The Journal of Chemical Physics* **2006**, *125*, 054515.

[119] K. Lum, A. Luzar, *Physical Review E* **1997**, *56*, R6283.

[120] A. Kalra, S. Garde, G. Hummer, *Proceedings of the National Academy of Sciences of the United States of America* **2003**, *100*, 10175–10180.

[121] W. L. Jorgensen, J. D. Madura, *Molecular Physics* **1985**, *56*, 1381–1392.

[122] P. A. Bonnaud, B. Coasne, R. J.-M. Pellenq, *Journal of Physics: Condensed Matter* **2010**, *22*, 284110.

[123] J. Xu, S. Kjelstrup, D. Bedeaux, A. Røsjorde, L. Rekvig, *Journal of Colloid and Interface Science* **2006**, *299*, 452–463.

[124] K. Yasuoka, M. Matsumoto, *The Journal of Chemical Physics* **1998**, *109*, 8463–8470.

[125] R. Marek, J. Straub, *International Journal of Heat and Mass Transfer* **2001**, *44*, 39–53.

[126] J. D. Bernal, R. H. Fowler, *The Journal of Chemical Physics* **1933**, *1*, 515.

[127] T. H. Yang, C. Pan, *International Journal of Heat and Mass Transfer* **2005**, *48*, 3516–3526.

[128] C. Vega, J. L. F. Abascal, I. Nezbeda, *The Journal of Chemical Physics* **2006**, *125*, 034503.

[129] R. Sakamaki, A. K. Sum, T. Narumi, K. Yasuoka, *The Journal of Chemical Physics* **2011**, *134*, 124708.

[130] J. L. F. Abascal, C. Vega, *The Journal of Chemical Physics* **2005**, *123*, 234505.

[131] W. L. Jorgensen, J. Chandrasekhar, J. D. Madura, R. W. Impey, M. L. Klein, *The Journal of Chemical Physics* **1983**, *79*, 926–935.

[132] T. Darden, D. York, L. Pedersen, *The Journal of Chemical Physics* **1993**, *98*, 10089.

[133] R. D. Groot, P. B. Warren, *The Journal of Chemical Physics* **1997**, *107*, 4423.

[134] G. Torrie, J. Valleau, *Journal of Computational Physics* **1977**, *23*, 187–199.

[135] J. Kästner, *Wiley Interdisciplinary Reviews: Computational Molecular Science* **2011**, *1*, 932–942.

[136] C. Song, B. Corry, *The Journal of Physical Chemistry B* **2009**, *113*, 7642–7649.

[137] S. Buyukdagli, M. Manghi, J. Palmeri, *The Journal of Chemical Physics* **2011**, *134*, 74706.

[138] D. Levitt, *Biophysical Journal* **1978**, *22*, 209–219.

[139] K. Falk, B. Coasne, R. J.-M. Pellenq, F.-J. Ulm, L. Bocquet, *Nature Communications* **2015**, *6*, 6949.

[140] T. Lee, L. Bocquet, B. Coasne, *Activated desorption at heterogeneous interfaces and long-time kinetics of hydrocarbon recovery from nanoporous media*, submitted, **2015**.

Abstract

The first part of this thesis is an introduction to the different energy conversion and desalination methods that will be invoked in this work.
In a second part, we show that the ionic conductance of a nanopore array is sub-additive with the number of pores. Individal contributions of each pore to the global conductance tend to a null value, if the network is big enough. We note that this phenomenon only involves length ratios, and that working at a nanometric scale does not have any influence.
Then, in a third part, we measure the permeability of a pore array at a macroscopic scale. There too, the effect of the array does not depend on the scale of the system. Permeability evolves inversely to conductance: permeability is enhanced by the presence of neighboring pores, but in a smaller proportion than the ionic conductance falls under the same cause.
The fourth part uses the results of the two preceding ones, to determine a scaling law for the electric power produced by streaming current and diffusio-osmosis, two methods of osmotic energy conversion. We show that entrance effects have a negative impact on such conversion, more efforts are needed to understand them better and circumvent them.
The fifth and last part of this thesis is a numerical work on a new desalination device. It relies on osmosis through a gas phase which is trapped within a hydrophobic nanotube. Its main interest is to use nanotubes bigger than the pores of currently used materials, thus less prone to fouling. We use molecular dynamics methods to study the permeability and selectivity of this device.

Key words : nanofluidics, entrance effects, pore arrays, ionic and fluidic transport, cross-coupling transport phenomena, osmotic energy, energy conversion, desalination